DYNAMICS OF GASEOUS AND SOLID FUEL FIRE WHIRLS

by

Monica Therese Ghosn

Submitted in partial fulfilment of the requirements
for the degree of Doctor of Philosophy

at

Dalhousie University
Halifax, Nova Scotia
October 2022

Table of Contents

List of Tables

List of Figures

Abstract

Fire whirls (FWs) are swirling diffusion flames with significantly enhanced burning rates, flame heights, and flame temperatures. The swirling motion combined with a more intense flame poses a greater hazard than a normal diffusion flame. Therefore, a deeper understanding of FW dynamics for various fuels will help to identify and mitigate additional fire risks. In this work, experiments were conducted to study the dynamics of propane gas and wooden crib FWs in a square-based, fixed-frame apparatus. Simulations were performed using Fire Dynamics Simulator (FDS) for propane gas FWs to study the impact of additional parameters and analyze the predictability of FW dynamics under various conditions.

Measurements of flame heights and temperature profiles were made with a low initial momentum propane burner using a variety of burner sizes and heat release rates (HRRs) under both FW and free burning (FB) conditions. The burner diameter and number of inlets on the apparatus did not significantly affect the flame stability, height, and temperature of FWs. Conversely, increasing HRR significantly increased flame height and temperature of FWs relative to FB conditions. Flame heights from FW and FB experiments were correlated using the equation proposed by Heskestad with a different fitting constant. The hood configuration, width of inlets, and height of walls on the apparatus strongly affected flame stability, height, and temperature. FDS predictions were generally in good agreement with the experimental data, but accuracy of FW simulations was found to depend strongly on grid resolution.

Both FB and FW experiments were also conducted using three square-based wooden crib sizes with side lengths of 76.2, 152.6, and 228.6 mm, 6.35, 12.7, and 19.1 mm cross-section sticks, respectively, and six sticks per layer (giving heights of 38.1, 76.2, and 114.3 mm). All crib sizes were tested with n = 3–7 sticks per layer. Compared to FB conditions, FWs produced a less luminous and cleaner burning flame. As n increased, the burning rate for the 152.6 and 228.6 mm FW tests increased from 1.0 to 1.84 and 1.16 to 1.47 times that of the FB cribs for the same geometric configuration. The FW flame heights for the 152.6 and 228.6 mm cribs were 1.02 to 1.4 times greater than for FB conditions.

List of Abbreviations and Symbols Used

CAF	Canadian Armed Forces
CFD	Computational fluid dynamics
DCTF	Damage Control Training Facility
DME	Dimethyl ether
FB	Free burning
FDS	Fire Dynamics Simulator
FW	Fire whirl
FWG	Fire whirl generator
HRR	Heat release rate
HHV	Higher heating value
JFRO	Joint Fire Research Organization
LHV	Lower heating value
RMSE	Root-mean-square error
SPIV	Stereo Particle Image Velocimetry
USFS	US Forest Service

Symbols

A	A constant in Equation (5-7) (cm kW^{-1})
A_v	Vent area (m^2)
A_s	Exposed initial surface area of the fuel (m^2)
A_{so}	Area of the openings on one side of a crib (m^2)
a	A constant in Equation (2-35)
B	A constant in Equation (5-7) (cm)
b	Crib stick thickness (mm)
b_v	Core radius (m)
C_p	Specific heat (J kg^{-1} K^{-1})
C	A constant in Equation (5-6a)
d	Pool diameter (m)
D	Diameter of the burner (m)
D_o	Diameter of fire whirl in this work (m)
D_S	Molecular diffusion coefficient (m^2/s)
$\mathcal{F}_B$	Body force (N)

g	Gravitational acceleration (m s^{-2})
H	Average flame height (m)
H^*	Normalized flame height (–)
ΔH_c	Heat of combustion (kW)
H_c	Height of chamber (m)
h	Height of crib (m)
h_f	Flame height measured from top of crib (cm)
K	Comprehensive dimensionless quantity (–)
k	A constant in Equation (2-35)
l	Crib length (mm or inch)
L	Horizontal length scale (m)
L_{ff}	Fitted flame height (m)
L_h	Dimensionless flame height (-)
LS	Left side
$\dot{m}$	Burning rate (g s^{-1})
$\dot{m}''$	Burning rate per area (kg m^{-2} s^{-1})
m_9	Slope for the 9-inch crib (cm)
m_6	Slope for the 6-inch crib (cm)
m_3	Slope for the 3-inch crib (cm)
N	Number of layers (–)
n	Number of sticks per layer (–)
P	Pressure (Pa)
p	A constant in Equation (5-6a)
$\dot{Q}$	Heat release rate (kW)
$\dot{Q}^*$	Dimensionless fire power (–)
$\dot{q}^{"}$	Radiative heat flux (kW m^{-2})
u_{boy}	Buoyant velocity (m s^{-1})
U_r	Radial velocity (m s^{-1})
U_z	Axial velocity (m s^{-1})
u_s	Spread rate (cm s^{-1})
u_z	Average gas velocity (m s^{-1})
$\dot{V}$	Volumetric flow rate (m^3 s^{-1})

RS	Right side
r	A constant in Equation (6-1) or stoichiometric air to fuel ratio
S^*	Normalized gap size (–)
s	Gap spacing or crib spacing (m)
t	Time (s)
T	Temperature (K)
V	Mixture fraction
V_{st}	Mixture fraction at height
W	Width of crib (m)
x	A constant in Equation (6-1)
Z	Normalized flame height (= z/H)
z	Axial location of temperature measurement (cm)

Greek Symbols

α_{eff}	Viscous core coefficient (-)
β	Thermal expansion (K^{-1})
γ	Mass stoichiometric ratio of air to volatiles (-)
ε	Porosity (-)
ς	A constant in Equation (5-17) ($m^{1/2}\ s^{-1}$), ($m\ kW^{1/5}\ s$), ($m^{4/3}\ kW^{1/3}\ s$)
η	A constant in Equation (5-17) (-)
κ	Thermal conductivity ($W\ m^{-1}\ K^{-1}$)
Γ	Circulation ($m^2\ s^{-1}$)
μ	Dynamic viscosity (Pa s)
ρ	Density ($kg\ m^{-3}$)
ω	Vorticity (rot/s)

Subscripts

ave	Average
b	Burner
c	Cylinder/container
conv	Convection
max	Maximum
o	Atmosphere
rad	Radiation

re-rad	Re-radiation
tot	Total
w	Fire whirl
∞	Ambient air

Acknowledgements

This thesis was possible primarily because of the people who supported me during my time in graduate school at Dalhousie University. First and foremost, I would like to thank my supervisors, Dr. Michael J. Pegg and Dr. Jan B. Haelssig. I am extremely grateful for their invaluable advice, continuous support, and patience during my Ph.D. study. They stood by my side from day one and helped me through all the ups and downs. Mike always pushed me to think outside the box allowing room for creativity and growth. He gave me the opportunity to travel across Europe presenting my research, which increased my passion in this field. I am extremely grateful for his sense of humor, experimental expertise, and Wednesday morning meetings. I cannot emphasize the gratitude I have for Dr. Haelssig. Jan was always there to provide encouragement, keep me on track, and going above and beyond in assisting with questions, modelling, and papers. His rigorous work ethic and passion for his research is an excellent example of how I will be pursuing my future career.

Sincere thanks to Dean Grijm, Peter Jones, Scott Mackinnon, Dr. Dominic Groulx, Cathleen Lupien, Christopher Salah, David McKinnon, the staff of the woodshop lab, and all the undergraduate students who worked or volunteered in the lab. Without your help, the FWG chamber, LabVIEW, experiments, and software would not have been successful.

Several experiments were conducted at the DCTF-Kootenay and a special thank you to Lt. Cmdr Andrew Cumming for allowing us to use the facility. These experiments could not have been completed without my sister, Marena, giving up her summer days to be by my side. She continues to be there whenever I need a helping hand.

My heartfelt thanks to my parents, Maroun and Lena, who have supported and guided me throughout school. Their strong work ethic was instilled in me at a young age. This thesis would not have been possible without your encouragement and unconditional love. To my sister, Stephanie, and brother, Antonios, who were always available for questions, late study sessions, endless support, and love.

A special thank you to my soccer family for teaching me how to stay dedicated, the importance of teamwork, and how to persevere through adversity. They always kept me smiling even when times were tough.

I owe the biggest thanks to two very special people, my husband Justin and my son, Jack, for their continued support, love, and understanding during my pursuit of a Ph.D. degree that made the completion possible. You were always around at the hardest times, and you helped to keep things in perspective. Words would never say how grateful I am to both of you.

Chapter 1: Introduction

1.1. Background

Fire whirls (FWs) are unique physical phenomena often associated with mass destruction and fatalities. They are an astonishing example of the destructive nature of fire behaviour with spinning diffusion flames, sudden formation, and erratic movement. They range in size from 0.5 m to 300 m in diameter with heights of over 500 m for some FWs that develop during wildland and forest fires. Fire tornadoes, fire whirls, swirling fires, and firenadoes are all terms used to define the spiral formation of a buoyancy-driven, swirling diffusion flame (Graham, 1955).

With the current climate conditions, the occurrence of wildfires have significantly increased across Canada and the United States, resulting in the need for more research in the field of fire safety engineering. In 2016, in St. Albert, Alberta a bush fire turned into a FW. It was traveling so quickly that one of the firefighters had to jump into the lake to escape from the heat (CBC News, 2016a). In Southern California, USA, in August 2016 fire whirls forced 82 000 people to flee the area. By the end of the day, it was a 7 300 Ha (73 km^2) monster and destroyed hundreds of homes (CBC News, 2016b). In 2018, the Guardian News (CNN, 2018) reported firefighters in British Columbia lost their hose as they were trying to extinguish a FW. In another instance in 2018, a FW in Northern California killed eight people and destroyed over 1 500 structures (The Guardian, 2018). More recent FW sightings were in July and August 2021, in Northern, California (Los Angeles Time, 2021). Two such naturally occurring fire whirls are shown in Fig. 1-1.

(a) (b)

Figure 1-1: Naturally occurring fire whirls in (a) Alberta, Canada (CBC News, 2016a), and (b) California, USA (CBC News, 2016b).

Although there has been a substantial increase in the number of studies investigating FW dynamics over the past decade, there remains a lack of general analysis methods and many unexplained phenomena. Indeed, in a recent paper, Baukal (2018) discussed the possibility of fire whirls as a natural phenomenon to explain the biblical story of the pillar of fire that led the Israelites out of the wilderness and into the promised land. Studies have shown that the formation of FWs requires a source of ambient vorticity. FWs are standing vortex structures which make them unpredictable and dangerous.

Since it is difficult to study FWs spontaneously formed in wildland or urban fires, they have been studied using a variety of small-to-medium-scale experimental facilities. With laboratory-scale experiments there are two geometrical configurations often used to generate a fire whirl. They are open configurations and enclosed configurations. With open configurations, strategically placed fires in cross-flow are used to induce a FW. With enclosed configurations, air is either entrained tangentially into the enclosure by the buoyant diffusion flame, or circulation is imposed on a buoyant diffusion flame. Tohidi *et al.* (2018), in a recent review discussed their fluid dynamics, conditions for their

formation, and the structure of fire whirls and describe in detail both open and enclosed configurations.

Most studies have investigated the dynamics of gas-fueled and liquid pool FWs using fire whirl generators (FWGs), where swirling is mechanically induced through a rotating screen or naturally induced by tangential entrainment of air into the buoyant fire plume (*e.g.*, split cylinders, fixed frame, *etc*.). A comparison between a laboratory-scale free burning (FB) propane fire and a FW from a 3 inch diameter sand-packed burner at a heat release rate (HRR) of 11.1 kW is shown in Fig. 1-2.

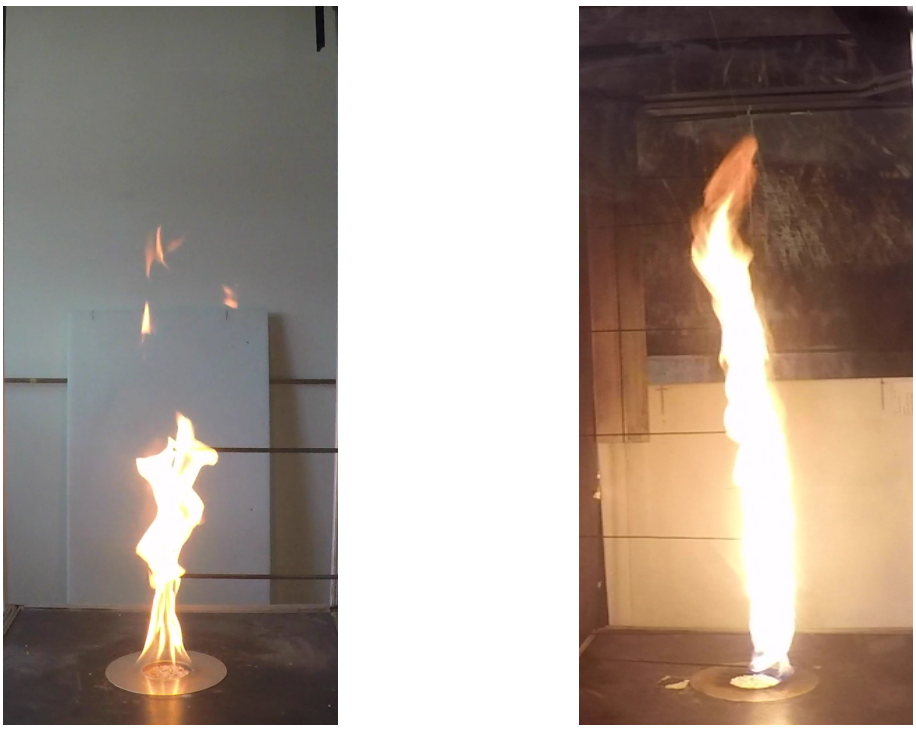

(a) (b)

Figure 1-2: Comparison of (a) FB and (b) FW propane flames for gas burner of 3 inch diameter and HRR of 11.1 kW.

Kuwana *et al*. (2008) showed that when FWs formed, they can be ten times more harmful than normal FB fires, thus making them a major safety concern. Guo *et al.* (2013) analyzed

the effect of inlet gap size on liquid-fueled FW stability. Lei *et al.* (2015) used a fixed-frame apparatus to investigate the effect of heat release rate on propane-fueled FWs. Lei *et al.* (2016) further explored the impact of system type and configuration on stability for both gas and liquid-fueled FWs. Two years later, Lei *et al.* (2017a) performed experiments to analyze the impact of apparatus configuration and operating conditions on flame precession. Yu *et al.* (2013) conducted a series of experiments to examine the effect of inlet gap size on liquid-fueled FW stability. Chow and Han (2011) used experiments while Yuen *et al.* (2018) used numerical simulations to examine the impact of air inlet asymmetry on fire dynamics. Along with many other studies, these investigations have shown that the type and configuration of the apparatus, as well as the fuel and heat release rates, have a strong impact on the dynamics and stability of the fire whirls. Although many studies have been performed, the impact of air inlet asymmetry on FW stability has only been investigated in a few studies. Past research has identified that FWs pose a significant hazard in wildland fires, commercial and residential building fires, and industrial facility fires due to increased flow velocities, flame heights and temperatures, heat radiation effects, and burning rates.

The FWs studied in this work are all considered to be small to medium scale. Small-scale FWs are 0.1–1 m tall. Medium-scale FWs are 1–10 m tall, and large-scale FWs are 10–100 m tall (Snegirev *et al*., 2004).

1.2. Objectives

The overall objectives of this research were to develop a better understanding of fire whirl formation and propagation and to develop better models for the prediction of their

behaviour. To address these challenges, a comprehensive review of the literature on FWs was undertaken, identifying gaps in knowledge, evaluating different models, and compiling a "roadmap" of the most promising models that may be used and under which conditions. Currently, the most promising models rely on computational fluid dynamics (CFD) methods because these methods are based on a theoretical framework that can potentially resolve the complex fluid dynamics involved. Therefore, the focus in the review is on identifying gaps that must be filled to enable the selection and development of sub-models for comprehensive CFD-based modelling of FWs.

To perform a comprehensive validation of predictive models, it was necessary to conduct experiments at different scales, with a range of chamber configurations, and over a broad range of conditions. A fixed-frame facility was constructed with adjustable walls, allowing the number of inlets and gap widths to be changed. This permitted experimentation on fire whirl formation and behaviour. Experiments were conducted using gas flames (propane), since they are less complex than cribs to analyze using a variety of burner sizes and HRRs. Further experiments were done using solid fuel wooden "crib" structures to investigate the impact of fire whirls on fire spread rates. Three different crib sizes with various packing densities were used to develop scaling parameters.

Finally, the experimental data was used for the validation of model predictions. Although there are a variety of open-source and commercial software packages that can be used for fire simulation, Fire Dynamics Simulator (FDS) has been chosen because it is commonly used by other researchers, it is open-source and freely available, and it is commonly used and industry accepted for analysis by practicing fire protection engineers.

1.3. Thesis Organization

In this work, both FB fires and FWs were investigated using gaseous (propane) and solid (wooden cribs) fuels. Flame heights and temperature profiles of propane FB and FW were measured using a variety of burner sizes, apparatus configurations, and heat release rates. For the wooden cribs, spread rates and burning rates were also determined. A general literature review on fire whirls discussing dimensional parameters, flame height correlations, and the type of FWG is presented in Chapter 2. The experimental set-up for both gaseous and solid FB and FW experiments is discussed Chapter 3. The numerical set-up, including the geometry and mesh dependence, is presented in Chapter 4. The FB gas data is discussed in Chapter 5, and it is compared with other research from the literature using flame height correlations. The FW data is analyzed in detail to determine which parameters affect the formation and stability. The dimensional analysis used for the FB flames was then used on the FW data. The results from Chapter 5 were used to examine the crib fires in Chapter 6, (*i.e.*, number of inlets, gap size, and chamber configuration). The FB data for cribs is presented in Chapter 6, and it is compared with other research from the literature. Furthermore, the correlations used by previous researchers were applied to the data, and an improved correlation was proposed. The FW data from the cribs were then investigated using dimensional and non-dimensional correlations as well as an analysis on the comparison of FB and FW cribs. Conclusions and recommendations for future work are presented in Chapter 7.

1.4. Significance

The spinning behaviour that makes fire whirls fascinating to observe also makes them highly unpredictable and dangerous. These types of fires do not only occur in wildfires, but similar phenomena can also occur in partially enclosed spaces (eg., buildings, container ships) making their understanding even more critical. In either case, the formation of fire whirls can greatly increase the spreading rate and decrease the predictability of wildfires, residential and commercial building fires, and industrial fires. As the climate warms, wildfires are becoming more intense and common. Therefore, FWs are also becoming more common and have been linked to spot fires. These spot fires can form multiple small fires ahead of the advancing fire front, the configuration of which can lead to the formation of FWs in different locations. Fire whirls pose increased risks to both public and private property, as well as commercial and industrial facilities and public safety. It is therefore important to understand their behaviour.

Additional research into the mechanisms governing flame height, burning rates, fire spread rates, and temperature profiles for gas-, liquid-, and solid-fuel fire whirls is ongoing. Many researchers are investigating pool and gas FWs, but minimal work is being undertaken with wooden structure FWs. As FWs form in forest fires, they are often started from wood and debris and a lot of similarity exists between natural FWs and those generated in the lab. This thesis contributes to research of solid fuel FWs as well as highlights the importance of developing and validating a computational fluid dynamics (CFD) model for FWs. To date, many numerical simulations have been completed with most of them using liquid or gaseous fuels. However, there is still a lack of consensus as to which parameters work best

for FW modelling. The validated numerical simulations can be modified and used for large-scale fire spread predictions. Based on the current theoretical models, it was found that they are not always applied correctly to the experimental data, thus proving the importance of having a range of laboratory experiments to assist in explaining and validating fire whirl behavior.

Another importance of this work is highlighting the differences between a free burning and fire whirl flame, which can be help advise fire practitioners. Currently there is no specific training on how to deal with fire whirls and safe practices need to be taught so if a FW occurs the fire practitioner can deal with it differently than they would for a FB fire.

The findings of this research project are critical for validating existing comprehensive fire modelling tools and to advise fire safety practitioners on the risks of FWs. This will help to formulate proper emergency measures for cases when a fire whirl is absent or present.

Chapter 2: Literature Review

2.1. Dimensional Analysis of Fire Whirls

Many numerical models have been developed during the past decade to predict fire behaviour, but their validation for large-scale fires is difficult due to the lack of experimental data. Dimensional analysis is a very important tool in fire research as it aids in developing simplifications for many phenomena such as HRR, flame heights, radiative heat transfer, and velocity profiles. Without its application it would be difficult to link small-scale experimental measurements and with large-scale fires. Tohidi *et al.* (2018) applied the Buckingham-Π theorem to develop thirteen non-dimensional groups, shown in Table 2-1. These non-dimensional groups provide a powerful technique that can help develop empirical correlations for fire whirls.

Table 2-1: Dimensionless groups relating to fire whirls.

Dimensionless group		Physical significance
Π_1	$\frac{U_z}{\sqrt{gH}}$	U_z is the axial velocity and H is the flame height. Represents the Froude number and plays a role of buoyancy in the flame formation.
Π_2	$\frac{\rho\Gamma}{\mu}$	ρ and μ are the density and dynamic viscosity of the gas. Γ is the circulation. Represents the vortex core due to the azimuthal velocity (swirling behavior).
Π_3	$\frac{H}{L_h}$	L_h is the diameter of the fire whirl or the gap spacing size. Dimensionless flame height.
Π_4	$\frac{\dot{m}}{\rho\sqrt{gL_h^5}}$	Ratio of the fuel flow rate to advection rate. Momentum buoyancy. Can be set to a constant value for a gas burner.
Π_5	$\frac{U_r L_h}{\Gamma}$	Represents circulation based on spacing and velocity. Swirl number.
Π_6	$\frac{\dot{Q}}{\rho C_p \Delta T U_z L_h^2}$	If multiplied by Π_1 represents the $\dot{Q}^*$parameter. Dimensionless fire power.
Π_7	$\frac{C_p\mu}{\kappa}$	Represents the Prandtl number. κ is the thermal conductivity of the gas.
Π_8	$\frac{\Delta\rho}{\rho}$	Pressure gradient. Assumed to be uniform for the ambient fluid.
Π_9	$\frac{\Delta T}{T}$	Tempurature gradient. Assumed to be uniform for the ambient fluid.
Π_{10}	$\beta\Delta T$	β is the coefficient of thermal expansion of the gas.
Π_{11}	$\frac{g\rho^2 L_h^3}{\mu^2}$	Multiplying by Π_{10} gives the Grashof number.
Π_{12}	$\frac{U_r}{U_z}$	Radial velocity U_r over axial velocity. Represents the swirling behavior.
Π_{13}	$\frac{\rho L_h D_S}{\dot{m}}$	D_S is the molecular diffusion coefficient of species. Represents the Peclet number. Average velocity of the fuel vaporizing.

Conducting a dimensional analysis on FB fires, Heskestad's correlation for propane fires can be simplified as follows:

$$H = f\left(\dot{V}, D, u_{boy}\right) \tag{2-1}$$

where the flame height, H is a function of volumetric flow rate, $\dot{V}$, diameter of the burner, D, and buoyant velocity, u_{boy}. Applying the Buckingham-Π theorem to these variables leads to the following non-dimensional groups:

$$\Pi_1 = \frac{H}{D} \qquad\qquad \Pi_2 = \frac{D^2 u_{boy}}{\dot{V}}$$

where $u_{boy} = \sqrt{gH}$, which leads to

$$\frac{H}{D} = \frac{D^2\sqrt{gH}}{\dot{V}} \tag{2-2}$$

As heat from the flame draws air upwards, the air gaps induce the fire whirl by natural convection causing the flame to rotate and increase in height. Conducting a dimensional analysis on FWs, Heskestad's correlation for propane fires can be modified as follows:

$$H = f\left(\dot{V}, D, u_{boy}, s\right) \tag{2-3}$$

where s is the gap width. Applying the Buckingham-Π theorem to these variables leads to the following non-dimensional groups:

$$\Pi_1 = \frac{H}{D} \qquad\qquad \Pi_2 = \frac{D^2 u_{boy}}{\dot{V}} \qquad\qquad \Pi_3 = \frac{s}{D}$$

Combing Π_1/Π_3 leads to the following expression:

$$\frac{H}{s} = \frac{D^2\sqrt{gH}}{\dot{V}} \tag{2-4}$$

Hartl and Smits (2016) studied FWs generated with split cylinders around a Méker burner using dimethyl ether (DME) as the fuel. They proposed that the flame height was a function of the gap size between two offset cylinder halves placed around the fuel source. The gap size, *s* and the HRR, $\dot{Q}$, could be changed independently. Their dimensionless groups were based on three different diameters: D_w the diameter of the FW, D_c the diameter of the cylinder, and D_b the diameter of the burner. They investigated the dependence of these parameters on the flame height, with the following nondimensional groups:

$$H^* = f_1(S^*, q^*, \frac{\Delta\rho}{\rho_o}, \frac{\Delta T}{T_o}, \frac{gD_b}{C_p\Delta T}, \frac{D_w}{D_b}) \tag{2-5}$$

where $H^* = H/D_b$, C_p is the specific heat of the air at ambient temperature, ΔT and $\Delta\rho$ are the changes in temperature and density at the flame front, T_o and ρ_o are the ambient air temperature and density, $Q^* = \dot{Q}/c_P\rho_o\Delta T\, D_b^2\sqrt{gD_b}$, and $S^* = S/D_c$. They assumed that the circulation was independent of height, leading to the following equation:

$$H^* = f_2(S^*, Q^*) \tag{2-6}$$

The formation of a fire whirl requires three conditions: (1) a generating eddy; (2) a fluid sink within the eddy; and (3) friction or drag of air at the ground boundary of the eddy (Bryam & Martin, 1970). The hot gas generated by the fire serves as the fluid sink, which entrains ambient air into the flame with angular momentum from the generating eddy. The equation of motion for a Newtonian fluid with varying density and viscosity can be stated as follows:

$$\underbrace{\frac{\partial}{\partial t}(\rho\vec{u})}_{\substack{\text{Rate of increase}\\ \text{of momentum}}} = -\underbrace{\nabla\cdot(\rho\vec{u}\cdot\vec{u})}_{\substack{\text{Rate of momentum gain}\\ \text{by advection}}} - \underbrace{\nabla P}_{\substack{\text{Pressure forces}\\ \text{on an element}}} - \underbrace{\nabla\cdot[\hat{\tau}]}_{\substack{\text{Rate of momentum gain}\\ \text{by viscous transport}}} + \underbrace{\mathcal{F}_B}_{\substack{\text{Body forces}\\ \text{on an element}}} \tag{2-7}$$

where $[\hat{\tau}]$ is the stress tensor arising from the viscous forces that can include turbulent components if time-averaged mean flow is being considered, and P is the static pressure, *i.e.,* the difference between the total pressure and the hydrostatic pressure in a quiescent air flow.

Vorticity $\vec{\omega}$ is a vector field which gives a local measure of the instantaneous rotation of a fluid. In other words, it is a measure of the spin about an axis and is defined mathematically as the curl of the velocity.

$$\vec{\omega} = \nabla\times\vec{u} \tag{2-8}$$

The vorticity equation, which governs the evolution of vorticity in the flow, is obtained by applying the definition of vorticity from Eq. (2-7) and taking the curl of the equation of motion, Eq. (2-8), divided by density (Snegirev *et al.*, 2004; Forthofer & Goodrick, 2011; Tohidi *et al.*, 2018):

$$\underbrace{\frac{\partial\vec{\omega}}{\partial t}}_{\substack{\text{Rate of change}\\ \text{of vorticity}}} + \underbrace{(\vec{\mathrm{u}}\cdot\nabla)\vec{\omega}}_{\substack{\text{Rate of vorticity}\\ \text{transport by advection}}} = -\underbrace{\vec{\omega}(\nabla\cdot\vec{\mathrm{u}})}_{\substack{\text{Tilting or}\\ \text{Dilation}}} \underbrace{+(\vec{\omega}\cdot\nabla)\vec{\mathrm{u}}}_{\substack{\text{Stretching or}\\ \text{Compression}}} \underbrace{-\nabla\frac{1}{\rho}\times\nabla P}_{\text{Baroclinic torque}} - \underbrace{\nabla\times\left(\frac{\nabla\cdot[\hat{\tau}]}{\rho}\right)}_{\substack{\text{Vorticity generation}\\ \text{by viscous shear}}} - \underbrace{\frac{1}{\rho}\nabla\times\mathcal{F}_B}_{\substack{\text{Vorticity changes}\\ \text{through body forces}}} \tag{2.9}$$

The left-hand-side of Eq. (2-9), *i.e.,* the substantial derivative $D\vec{\omega}/Dt$, accounts for the temporal (*i.e.,* the time rate of change of vorticity at a point) and spatial transport of

vorticity by advection as a result of air flow throughout the domain. Thus, vorticity generated in one location can influence the conditions at another location.

Each of the terms on the right-hand-side of Eq. (2-9) represent the various sources by which vorticity is changed, generated, or dissipated. The first term $\vec{\omega}(\nabla \cdot \vec{u})$ describes the tilting, or dilation, of vorticity as a result of velocity gradients (*i.e.,* the transformation of horizontal vorticity into vertical vorticity and *vice versa*, as shown in Fig. 2-1(a)). The second term $(\vec{\omega} \cdot \nabla)\vec{u}$ represents the effects of expansion on the vorticity field and describes how flow convergence, stretches vortices thereby increasing the magnitude of vorticity in the direction of stretching shown in Fig. 2-1(b), or, conversely, how flow compresses vortices thereby decreasing the magnitude of vorticity in the direction of compression. Indeed, vortex stretching is the mechanism by which turbulent kinetic energy is transferred from the larger to the smaller length scales. In a fire, heat release causes large changes in density, leading to high expansion rates in which case $\nabla \cdot \vec{u}$ is positive, and because of the negative sign in front of this term, expansion will decrease the magnitude of the vorticity. These first two terms, tilting/dilation and stretching/compression, do not generate new vorticity; they only redistribute vorticity that has already been generated in the flow.

(a) Example of tilting—*i.e.,* the transformation of horizontal vorticity into vertical vorticity and *vice versa*.

(b) Example of vortex stretching—*i.e.,* the effects of expansion on the vorticity field.

Figure 2-1: Tilting (a) and stretching (b) of a propane fire whirl with D_b = 102.3 mm and HRR = 5.6 kW; frames taken 5 s apart.

The third term $\nabla\frac{1}{\rho}\times\nabla P$, referred to as the solenoidal or baroclinic torque, represents vorticity generated from unequal acceleration when the pressure and density gradients are not parallel. In a fire, there is a horizontal temperature gradient caused by rapid heat release, and this temperature gradient is not aligned with the vertical pressure gradient. It is the resulting misalignment of these two gradients that causes rotational motion leading to mixing of cold and hot fluid in order to restore balance. The fourth term $\nabla\times\left(\frac{\nabla\cdot[\hat{\tau}]}{\rho}\right)$ represents the generation of vorticity through viscous shear stress and accounts for the effects of viscous diffusion on the distribution of vorticity. Viscous stress causes vorticity in the flow to diffuse in space. The last term in Eq. (2-9), $\frac{1}{\rho}\nabla\times\mathcal{F}_B$, accounts for changes in vorticity due to external body forces acting on a fluid element, such as gravity, electric, or magnetic fields. In the absence of any external body forces other than gravity, the only body force is due to buoyancy, in which case $\mathcal{F}_B = (\rho - \rho_0/\rho)\vec{g}$, and the last term in Eq. (2-9) can be written as $\nabla\frac{\rho_0}{\rho}\times\vec{g}$ where ρ_0 is a reference density.

2.2. Flame Height

Many researchers have developed flame height correlations for free burning (buoyant) fires using a wide variety of fuels (gaseous and liquid) and different burner diameters. Thomas (1960) has derived the following expression using a simple dimensional analysis for a buoyant diffusion flame resulting from a single-fuel system issuing from an orifice of diameter *D* with low initial momentum:

$$\frac{H}{D} = f_1\left(\frac{u^2}{gD}\right) = f_2\left(\frac{\dot{V}^2}{gD^5}\right) \tag{2-10}$$

in which *H* is the visible flame height, *g* is the gravitational acceleration, *u* is the velocity at the orifice, and $\dot{V}$ is the volumetric fuel flow rate. The fuel flow rate is not only a measure of the amount of fuel but also the amount of air required for combustion. Furthermore, $\dot{V}/D^2$ represents both the velocity and the momentum of the flow.

Steward [1970] proposed the following flame height correlation:

$$\frac{H}{D} = N_{co} \tag{2-11}$$

where N_{co} is the dimensionless group given as

$$N_{co} = \frac{\dot{Q}^2(r + w/\rho_o')^2}{\rho_a^2 \Delta H_c^2 g D^5 (1-\omega)^5} \tag{2-12}$$

where $\dot{Q}$ is the HRR, ΔH_c is the heat of combustion of the fuel, *r* is the stoichiometric air to fuel ratio, w is the inverse volumetric expansion ratio, ρ_o' is the density of the fuel at ambient condition, ρ_a is the density of the ambient air, and *D* is the radius of the jet flame.

Heskestad [1983] originally proposed the following correlation:

$$H/D = -1.02 + 15.6N^{0.2} \qquad 10^{-6} \leq N \leq 10^{5} \tag{2-13}$$

where N is a dimensionless parameter, which is given by

$$N = \frac{c_{P_\infty} T_\infty}{g\rho_\infty^2 (\Delta H_c/\gamma)^3} \cdot \frac{\dot{Q}_{chem}^2}{D^5}$$

in which c_{P_∞} is the specific heat, T_∞ the ambient temperature, ρ_∞ is the density of the air, $\dot{Q}_{chem}$ is the theoretical HRR assuming complete combustion, ΔH_c is the LHV of the fuel, and γ is the mass stoichiometric ratio of air to volatiles. Setting

$$A = 15.6\left[\frac{c_{P_\infty} T_\infty}{g\rho_\infty^2 (\Delta H_c/\gamma)^3}\right]^{0.2} \tag{2-14}$$

hence Eq. (2-13) can be written as

$$H/D = -1.02 + A\dot{Q}_{chem}^{0.4} \tag{2-15}$$

where for many fuels $A \approx 0.235$ mkW$^{-0.4}$.

The HRR is (kW) is given by

$$\dot{Q}_{chem} = \varrho_\infty \dot{V} (\Delta H_c/\gamma) \tag{2-16}$$

Rearranging Eq. (2-16) gives

$$\dot{V} = \dot{Q}_{chem}/\rho_\infty (\Delta H_c/\gamma) \tag{2-17}$$

Now substituting for $\dot{V}^2$ from Eq. (2-17) into the second Pi group on the *RHS* of Eq. (1) results in[1]

[1] This was derived by Heskestad and is given as Eq. (13.4) in the SFPE Handbook, 5th ed., p 400.

$$\left(\frac{\dot{V}^2}{gD^5}\right) \equiv \left[\frac{1}{g\rho_\infty^2(\Delta H_c/\gamma)^3}\right]\frac{\dot{Q}_{chem}^2}{D^5} = N \tag{2-18}$$

Heskestad defined a dimensionless Froude number as

$$\dot{Q}^* = \dot{Q}_{chem}/\left(\rho_\infty c_{P_\infty} T_\infty D^2\sqrt{gD}\right) \tag{2-19}$$

Eq. (2-19) can be rearranged as

$$\dot{Q}_{chem}^2 = \left(\rho_\infty c_{P_\infty} T_\infty\right)^2 D^5 (Q^*)^2 \tag{2-20}$$

Now substituting for $\dot{Q}_{chem}^2$ from Eq. (2-20) into Eq. (2-18) gives the relationship between *N* and $\dot{Q}^*$ as

$$N = \left[\frac{c_{P_\infty} T_\infty}{\Delta H_c/\gamma}\right]^3 \cdot \dot{Q}_{chem}^2 \tag{2-21}$$

According to Heskestad (1998), the parameter $\dot{Q}^*$ does not account correctly for the observed variations in flame height (increasing flame height with increasing ambient temperature), while the parameter *N* does; for this reason, *N* is considered the more appropriate scaling parameter.

However, the recommended flame height correlation given in the SFPE Handbook (Heskestad, 2016) is the Heskestad's correlation (Heskestad, 1963) in the form given by McCaffrey (1995). He correlated flame heights from buoyant diffusion pool fire flames using the following:

$$H/D = -1.02 + 3.7{Q^*}^{0.4} \tag{2-22}$$

where *D* is the equivalent diameter of the fuel source. The dimensionless form of the heat release rate Q^* can be evaluated by the following equation in terms of $\dot{Q}$ (W ≡ kg m^2 s^{-3}),

density of ambient air ρ_∞ (kg m^{-3}), specific heat capacity $c_{p\infty}$ (kJ kg^{-1} K^{-1}), ambient temperature T_∞ (K), gravitational acceleration g (m s^{-2}), and diameter of fuel tray D (m).

$$Q^* = \frac{\dot{Q}}{\rho_\infty c_{p\infty} T_\infty \sqrt{gD} D^2} \tag{2-23}$$

These correlations will be further examined in Chapter 5.

A fire whirl presents additional difficulties when trying to formulate a height correlation. This is due to circulation, the diameter of the FW, and the inflow at the base (Hartl *et al.*, 2016). The restriction of air reduces the amount of oxygen to the flame and causes the flame to get taller. The FW flames produce thinner diameters and larger heights than the FB fires with the same HRR and fuel source diameter. This phenomenon has been studied experimentally by Hartl *et al*. (2016), Lei *et al*. (2011; 2015), Kuwana *et al*. (2008; 2013), Zhou *et al*. (2013), and Chuah *et al*. (2007).

Kuwana *et al*. (2008) developed the following flame height correlation for small pool fires using dimensional analysis:

$$\frac{H}{L} \sim \left(\frac{\Gamma}{gL^3}\right)^{1/3} \tag{2-24}$$

where H is the flame height, and L is the horizontal length scale *i.e*., diameter. For large pool fires they obtained the following:

$$\frac{H}{L} \sim \frac{\Gamma}{gL^3} \tag{2-25}$$

where H is independent of circulation and is controlled by the burning rate.

Chuah *et al*. (2007) used an analytical model to predict the FW flame shapes and flame height. They concluded the FW flame height is only a function of burning rate, which is dependent on flame temperature and the FW core diameter. Kuwana *et al*. (2011) used spilt cylinders to analyze the flame height of weak FWs using an ethanol pool fire and a methane burner flame. They developed an analytical model that showed the flame height is a function of burning rate, fuel type, and pool diameter:

$$H = \frac{u_z d/2D_m}{4ln[1/(1-V)]} \tag{2-26}$$

where u_z is the average gas velocity at the liquid surface, d is the pool or burner diameter, V is the mixture fraction, and D_m is the mass diffusivity. They also observed with the presence of a whirl, the flame becomes thinner than the corresponding FB tests. Klimenko and Williams (2013) proposed the following height expression:

$$\frac{H}{d} = \frac{u_o d}{8\alpha_{eff} D_m V_{st}} = \frac{Pe}{8\alpha_{eff} V_{st}} \tag{2-27}$$

where d is the pan diameter, D_m is the mass diffusivity, u_o is the average velocity, α_{eff} is viscous core coefficient which is $\alpha_{eff} = 2$ for a Burgers vortex, and V_{st} is the mixture fraction at H. Thus, the height is related to the burning rate, pan diameter, and fuel type. Hartl and Smits (2016) proposed that the flame height is a function of circulation, $H^* = 0.74(\Gamma^*)^{1.11}$, and the geometry of the enclosure, and the HRR from the fire control the circulation. Lei *et al*. (2017a) conducted a series of tests in a square fixed-frame facility using propane and heptane fuels. Lei *et al*. (2011) initially developed the correlation, $H^* \cong K\left(\dot{Q}\Gamma^{*2}\right)^m$, to correlate both their propane and heptane FW data. They defined the

dimensionless circulation as $\Gamma^* = \Gamma/\left(\sqrt{g} \cdot d^{3/2}\right)$, in which d is the fuel diameter, K is a comprehensive dimensionless quantity, and m is a constant. However, the two fuels formed two separate fitted lines. To fit the flame heights of any fuel type they proposed the following semi-empirical correlation based on turbulence suppression:

$$H^* = \Pi^{1/(2+n)} - 1.75(1 - \beta\overline{Ri})^{-1} \tag{2-28}$$

where $H^* = H/d_0$, and $\Pi = B\left(\frac{k_{pf}}{k}\right) d_0^{(0.5-n)} \dot{Q}^*(1 - \beta\overline{Ri})^{-2}$, which is a dimensionless parameter, and $B = A/0.46^2$. The turbulence is represented by $(1 - \beta\overline{Ri})$, and $\dot{Q}^*(1 - \beta\overline{Ri})^{-2}$ is similar to $\left(\dot{Q}^*\Gamma^{*2}\right)$. $\overline{Ri}$ is the mean Richardson number in the axial direction for swirling flow. Lei (2017b) also proposed a correlation for the core radius (b_v) for propane FW when $z < H$:

$$b_v = 2.44\dot{Q}^{0.29} \tag{2-29}$$

They concluded that flame height is correlated with HRR, the mean Richardson number, and the axial velocity parameters.

Gao *et al*. (2019) used a square-based vertical shaft with one corner inlet to investigate gasoline pool fires. They obtained a flame height correlation of $H/D = X{\dot{Q}^*}^{2/5}$, where D is the fire source diameter, and X is a constant characteristic of the FW. In their study, X was 5.07. They concluded that the gap width is a key parameter for determining the flame height and swirling intensity, and they formed the following empirical formula:

$$H/D = \frac{XL_{ff}}{L_{ffmax}} \dot{Q}^{*2/5} \tag{2-30}$$

where L_{ff} is the fitted flame height to the dimensionless gap width, and L_{ffmax} is the maximum flame height. Zou *et al*. (2017) also correlated flame height with the corner gap width in a square vertical shaft for a gasoline pool FW and found a linear relationship.

2.3. Comparison of Fuels

2.3.1. Liquid pools

A pool fire is a turbulent diffusion flame above a horizontal pool of vaporizing flammable liquid in which the vaporizing liquid has zero or very low initial momentum. There are three categories of pool fires: (1) confined pool fires in which the pools' diameter holds constant; (2) unconfined pool fires in which the pool spreads as it burns; and (3) fires on water.

The surface temperature of the liquid in a pool fire is very near the boiling point (or the end point of an ASTM distillation curve). The liquid fuel is heated up to its boiling point, evaporates, and then burns in the vapour phase. The burning rate per unit area of the pool is given the symbol $\dot{m}''$ [kg m^{-2} s^{-1}]. A simple energy balance gives the following (Babrauskas, 1983):

$$\dot{m}''\Delta H_g = \dot{q}''_{rad} + \dot{q}''_{conv} - \dot{q}''_{re-rad} - \dot{q}''_{loss} \tag{2-31}$$

in which $\dot{q}''_{rad}$ (kW m^{-2}) is the radiative heat flux absorbed by the pool, $\dot{q}''_{conv}$ (kW m^{-2}) is the convective heat flux to the pool, $\dot{q}''_{re-rad}$ (kW m^{-2}) is the radiative heat flux that radiates back from the pool, and $\dot{q}''_{loss}$ (kW m^{-2}) is the heat flux that is lost to the enclosure walls by conduction and any other transient heat losses. The last two terms of Eq. (2-31) are usually

small in comparison to the radiative and convective fluxes and are, therefore, ignored. Thus,

$$\dot{m}'' = \dot{q}''_{tot}/\Delta H_g \tag{2-32}$$

in which $\dot{q}''_{tot}$ is the total heat flux received by the fuel surface.

The earliest quantitative work on fire whirls was an experimental study by Emmons and Ying (1967). They measured the mass loss rate of acetone in a fuel pan surrounded by a rotating screen, thereby enabling them to independently vary the circulation rate. It was discovered that the mass loss rate increased steadily with ambient circulation; however, no definitive explanation for this phenomenon was suggested. Muraszew *et al.* (1979) conducted experiments on fire whirls within a stationary cylinder with a conical section at the top and a series of tangential inlets (6 in total) located in the bottom section. The fuels were acetone and wood cribs. Many later researchers conducted experimental studies using Emmons and Ying's method of imposing circulation with a rotating screen, or by using solid walls with asymmetrically placed openings whereby the fire induces the circulation. Although there have been many studies on FWs since Emmons and Ying's seminal work, there is still limited experimental and theoretical results on burning rates of fire whirls (Lei *et al.,* 2015).

Hartl and Smits (2016) studied fire whirls generated with split cylinders around a 38.1 mm diameter burner using DME as the fuel. They used Stereo Particle Image Velocimetry (SPIV) to measure the flow field velocities within and around the FW. From their SPIV measurements they concluded that air was entrained into the fire whirl along the base plate, and that the air above this layer moved away from the FW thereby creating a recirculation

zone. They stated the circulation plays an important role in the scaling of FWs, but in a fixed-frame FWG the circulation is only a function of the HRR and the gap width. In other words, it is the geometry of the enclosure and the HRR from the fire that controls the circulation. Finally, Parente *et al*. (2019) compared their numerical results with the experimental results of Hartl and Smits (2016) in which they plotted the dimensionless flame height against the dimensionless circulation. The correlations resulted in $1.9\left(\Gamma^{*0.8}\right)$, where $\Gamma^{*} = \Gamma/\left(\sqrt{g} \cdot d_0^{3/2}\right)$.

2.3.2. Gaseous fuels

The benefits of conducting FW experiments with a gaseous fuel are (1) they are more easily repeatable, (2) gaseous fuels (*e.g.*, propane) are cost effective, and (3) the flow rates can be controlled, which means that the heat release rates (HRR) are known. A number of researchers have used gaseous fuels in fixed-frame apparatus, *e.g*., Lei *et al*. (2015) and Lei and Lui (2016), and split cylinders, *e.g*., Kuwana *et al*. (2011), Lei *et al*. (2017b), Hartl and Smits (2021; 2016).

Lei *et al.* (2015) investigated propane FWs in their fixed-frame apparatus. They used a 300 mm diameter gas burner with a 50 mm thick porous bed made of glass beads. Seven HRRs of 25, 50, 100, 150, 200, 250, and 300 kW were studied. They made extensive measurements of temperature profiles (axial and radial), velocity profiles, air entrainment, and flame height. The plotted the centreline excess temperature ($\Delta T = T - T_\infty$) as a function of the normalized height $Z = z/H$ in which T is the temperature at height z, and T_∞ is the ambient temperature. They indicate that the end of the continuous flame occurs at $Z = 0.77$, *i.e.,* at 77% of the average flame height, $\Delta T \approx 1000$°C (1 273 K). However, the

value of ΔT varies considerably for different values of the HRR when $Z > 1$, *i.e.,* in the plume region where z is greater than H.

Lei *et al*. (2015) investigated the difference in flame precession between a square-based fixed-frame FWG and a small-scale rotating screen FWG using a propane gas burner of 50 mm diameter. They found that the precession frequency was similar in both FWGs, concluding that the flame precession frequency is dominated by aerodynamics not the FWG geometry or HRR. Lei and Liu (2016) investigated the transition process between FW and FB propane flames, which was similar to the observations from the present study in Fig. 1-2. Lei *et al*. (2017b) further analyzed the flame height, correlating it to a Richardson number related to the average flow quantities and developed as Eq. (2.28).

2.3.3. Solid fuels

Crib fires can fit into three categories: (1) non-propagating fires in which the fire is ignited uniformly as studied by Gross (1962), Block (1971), and McAllister (2015); (2) propagating fires in which the fire is ignited in the centre and spreads outwards as studied by O'Dogherty and Young (1964), Smith and Thomas (1970), Delichatsios (1976), Pegg (1980), Hu *et al.* (2006), Xu *et al.* (2008), and Diab *et al.* (2020); and (3) long rectangular cribs ($l >> h$) to study fire spread rates as used by Fons *et al.* (1960).

With crib fires it is not possible to measure the fuel flow rate directly; instead, the weight loss $\dot{m}$ must be measured. Thomas (1962) proposed a correlation to determine the flame height for a crib derived from Eq. (2.10):

$$\frac{\dot{V}^2}{gD^5} = \frac{\dot{m}''^2}{\rho_0^2 gD} \tag{2-33}$$

For a crib characteristic dimension D, the mass flux is given by $\dot{m}'' = \dot{m}/D^2$. Since,

$$\frac{H}{D} \propto \frac{\dot{V}^2}{gD^5} \tag{2-34}$$

the normalized flame height can be equal to the right side of Eq. (2-33), leading to the following expression:

$$\frac{H}{D} = k\left(\frac{\dot{m''}}{\rho_o\sqrt{gD}}\right)^a \tag{2-35}$$

where H is the flame height, $\dot{m}''$ is the burning rate per area ($\dot{m}'' = \dot{m}/l^2$), ρ_o is the air density, g is gravitational acceleration, and k and a are constants. For circular crib fires, D is the diameter; for square cribs D is the side length of crib (l); and for rectangular cribs, $D = \sqrt{(Wl)}$, where W is the width, and l is the length.

To date, only a few papers on solid fuel fire whirls have been published. The first was Martin *et al*. (1976) who used wood cribs (Douglas fir) and investigated the burning rate difference between FB crib fires and crib FWs. He concluded that there was a significant increase in the burning rates of solid fuel fire whirls: burning rates were 1.4–4.2 times larger than the burning rates of the FB flames. Chow and Han (2011) completed two sets of experiments in which they used toothpicks to build a crib and wood chips. Using a vertical shaft fire chamber, they examined FW formation and flame heights for liquid and solid fuels. Their investigation found that wood chips formed larger flame heights than

wood cribs. However, no comparison was done between FB and FW cases for flame height and burning rate.

Pinto *et al*. (2017) used forest fuels (needles, straw, dead leaves, and mixed shrubs) in a medium-scale FWG with one and four corner gaps (circular intake chamber). They observed that the FW flame height and diameter were larger and smaller than FB fires, respectively. They compared the flame height and heat release rate with full-scale fire whirls. They developed the following correlations for the diameter of the container (d_c) against the diameter of the fire whirl (d_w) as well as for the flame height (H) against HRR ($\dot{Q}$):

$$d_w = 0.41 d_c^{0.39} \tag{2-36}$$

$$H_{FB} = 0.18 \dot{Q}_{FB}^{0.46} \text{ and } H_{FW} = 0.35 \dot{Q}_{FW}^{0.38} \tag{2-37}$$

2.4. Types of Fire Whirls Generators

Table 2-2 provides a list of facilities used for fire whirl experiments, with advantages and disadvantages for each type of system. A diagram of each chamber type is shown in Fig. 2-2.

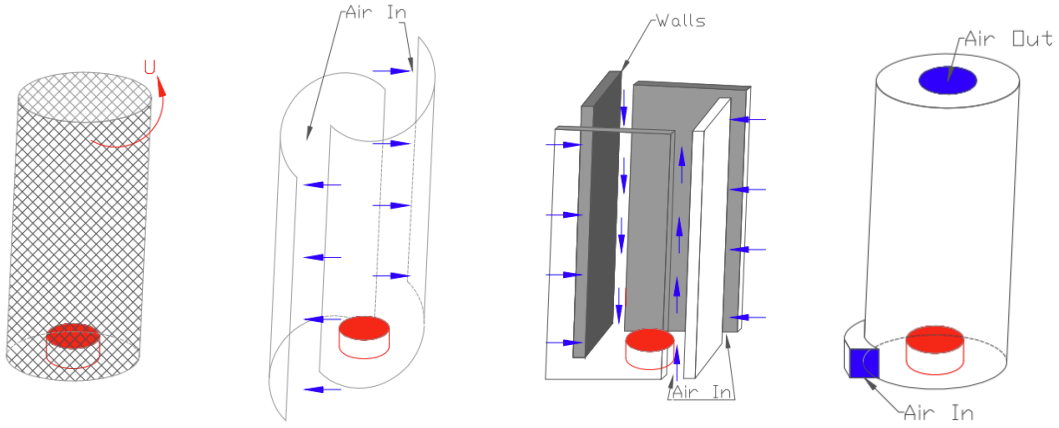

Rotating Screen **Spilt Cylinders** **Fixed Frame** **Circular Intake**

Figure 2-2: Diagram illustrating the main types of different FW generators.

Table 2-2: Comparison of the different FW generators.

Facility	Advantages	Disadvantages	References
Rotating screen	Controls circulation	Difficult to insert measurement probes	Lei *et al.* (2017a); Lei & Liu (2016); Lei *et al.* (2015); Chigier *et al*. (1970); Emmons & Ying (1967)
Split cylinders	Cost effective	Difficult for measurements	Hartl & Smits (2021, 2016); Parente *et al*. (2019); Yamada & Kuwana (2019); Wang *et al*. (2018); Kuwana *et al.* (2011).
Fixed frame	Easy to place probes for measurement. Simple adjustments can be made, *i.e.,* number of openings, gap size, *etc.* Shape can be changed, but most researchers use square.	Difficult to measure circulation. May produce additional vortices in the system due to the recirculation zones at the corners.	**Square:** Hariharan *et al*. (2021); Wang *et al*. (2018); Lei *et al*. (2017b, 2016, 2015, & 2013); Zhou *et al*. (2013); Chuah et al. (2013) **Hexagonal**: Lei & Li (2016); Yu *et al*. (2013) **Vertical Shaft (One inlet):** Gao *et al. (*2019); Zou *et al.* (2019); Yuen *et al*. (2018); Chow *et al*. (2017)
Circular intake	Circulation can be adjusted. The air entrainment can be fixed.	Difficult to adjust measurements within.	Pinto *et al.* (2017); Martin *et al.* (1976)

The fixed frame facility was chosen because of its simple geometry, advantages such as ease in measuring the temperature with thermocouples, having the ability to adjust the walls and openings, and the fixed glass walls allow for video measurement of the flame height. Furthermore, the fixed-frame apparatus does not impose the circulation on the fire, the fire controls the circulation.

2.5. Summary

Many flame height models have been presented for fire whirls. However, their accuracy is questionable when applied to a broad range of conditions, fuels, and geometries. Pinto *et al*. (2017) stated that the Burgers vortex cannot be used for a FW due to the complexity of the flow associated with density and temperature changes near the flame. No specific flame height correlation has been found for FWs. This justifies the importance of experimental data and laboratory experiments to explain and validate fire whirl behaviour. It is important to evaluate and to understand the differences, advantages, and limitations encountered when using solid fuels as opposed to gaseous fuels. There is a gap of research completed on fire whirls using solid fuels, more specifically structured solid structures such as wooden cribs. The existing flame height and burning rate correlations used for FB flames have been used for FW flames to compare and demonstrate how well they correlate. Detailed analysis of crib FWs will close a gap in literature as no other researcher has done an extensive study on this topic.

Chapter 3: Experimental Methods

3.1. Fire Whirl Generator

A small-scale, square-base, fixed-frame fire whirl generator (FWG) with dimensions of 0.61 m × 0.61 m × 1.22 m high, as shown in Fig. 3-1, was designed, and built to study the dynamics of fire whirls. The front and rear housed 6.35 mm thick tempered glass sheets, and the two sides housed 6.35 mm thick aluminum sheets. The four sides were supported in tracks, which enabled them to slide. Thus, the air gap could be adjusted to any desired width. For some experiments, aluminum plates (0.79 m × 0.102 m × 6.35 mm) were affixed at the top of the air gaps to restrict the openings to the lower part of the enclosure. The base and frame were constructed of aluminum. The base plate had an opening to accommodate the propane burners or the weighing platform on which the cribs were placed. An extract hood extending approximately 300 mm beyond the sides of the chamber and covered the top of the unit for the first three sets of propane experiments and first set of crib experiments conducted in a lab at the university. For the fourth set of propane experiments, and the second set of crib experiments the hood was removed, and the apparatus was relocated to the Canadian Armed Forces (CAF) burn rooms at the Damage Control Training Facility (DCTF) Kootenay in Herring Cove, Nova Scotia, Canada.

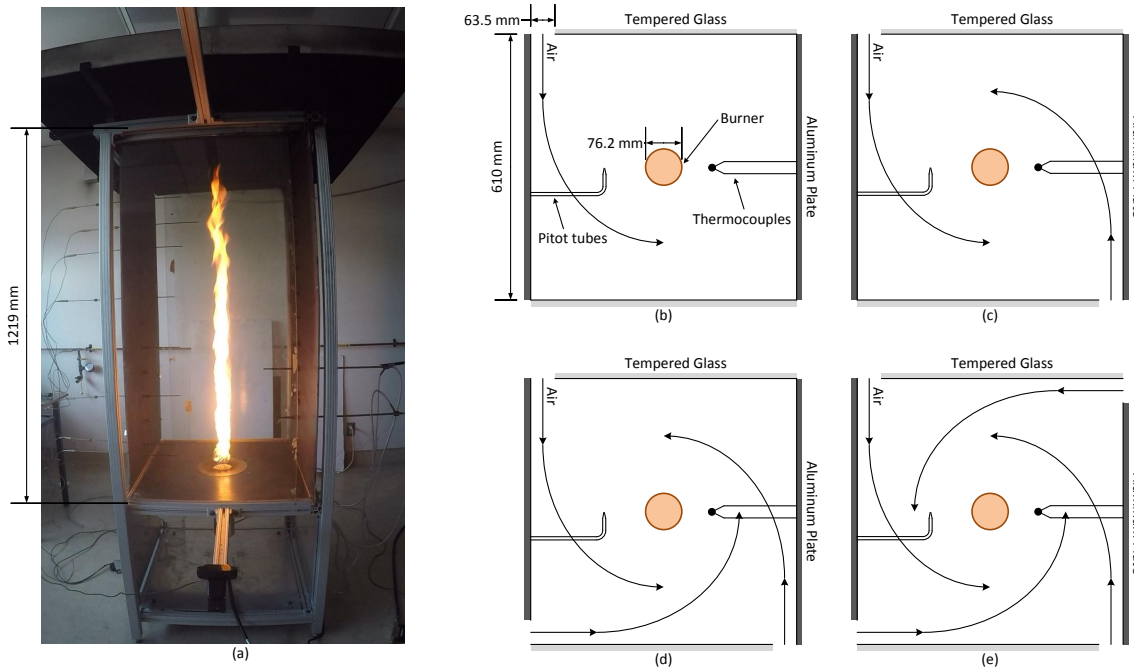

Figure 3-1: (a) Picture of the experimental apparatus. Description of the four investigated configurations: (b) one inlet, (c) two inlets, (d) three inlets, and (e) four inlets.

3.2. Propane Experiments

The first set of gaseous fuel experiments were used to determine the parameters that made the most stable fire whirl. They were also used for initial comparison of flame height and flame temperature of a flame with and without fire whirl formation, (*i.e.*, to compare FWs with FB, buoyant diffusion flames).

Propane fuel was delivered to the chamber by one of four different burners. They were fabricated from schedule 40 steel piping of nominal 2 in, 3 in, 4 in, and 6 in diameters. The actual internal diameters were 52.5 mm, 77.9 mm, 102.3 mm, and 154.1 mm. The uniformity of the flow across the surface area of the burner was checked by flowing air through the system at different flow rates and checking the velocity across the outlet with an anemometer. The base plate of the apparatus had an opening to accommodate the

different diameter gas burners. Each burner was packed with wire wool at their base and then filled with sand. This produced a low initial momentum burner with the fuel evenly distributed over the cross-sectional area. The mass flow rate, and hence the heat release rate, was controlled by a mass flow meter (FMA-2068A Omega engineering) to give propane flow rates. The HRRs were chosen based of the limitation of the flow meter used and gas supply pressure. The maximum flow rate that could be produced was 14 LPM. At low HRR (5.56 kW, i.e., 4 LPM) a FW was formed, however the flame height was small, so the majority of HRRs were conducted with 6, 8, 10, and 12 LPM respectively (corresponding to 8.33, 11.1, 13.9, and 16.7 kW, respectively based on a lower heating value (LHV) for propane of 46.3 MJ kg^{-1})

For the first set of experiments, stable FWs were formed by setting the air gaps to 450 mm high × 65 mm wide. The FB flames were formed by removing the tempered glass front and back walls. Temperatures were measured with type K thermocouples, centered in the chamber. The thermocouples had a 1.52 mm diameter exposed bead. Eight thermocouples (T1–T8) were positioned at heights of 50, 100, 300, 500, 700, 900, 1 000, and 1 100 mm above the burner rim. Measurements were made at six different radial distances: 0 (centre of the burner), 20, 40, 60, 90, and 150 mm.

In the second set of experiments, the influence of the air gap width on the formation and flame height of the FW was investigated. The 77.9 mm (nominal 3-in) burner diameter was used with an HRR of 11.1 kW. The four-inlet configuration was used, and a full height gap of 1.22 m high × 65 mm wide was maintained. A total of fourteen tests was completed with the air gap width, *s*, set between 20 and 200 mm in increments 20 mm, and 250, 270, 300, and 320 mm. A gap width of 320 mm corresponds to an opening half the length of the side

of the FWG.

In the third set of experiments, the stability of the FWs was studied as a function of the number of openings. The openings were varied from one to four inlets, as shown in Fig. 3-1. Air was admitted through these opening by the natural entrainment. The size of the air gap was set to three different configurations: full height (1.22 m high × 65 mm wide); half height (0.45 m high × 65 mm wide); and mixed, which was a combination of half and full air gaps. The half and mixed air openings used aluminium plates (0.79 m × 0.102 m × 6.35 mm) to restrict the opening at the top of the air gaps, thereby directing the air to lower part of the enclosure. The HRRs used were approximately 8.3 and 11.1 kW. Temperatures were measured at the same vertical locations as before (T1–T8) and at radial distances of 0 (centre of the burner), 20, 40, 60, and 100 mm.

In the fourth set of experiments, the influence of the hood on the stability of the fire whirls was examined. All temperature measurements were taken at the centreline of the burner with type K thermocouples positioned at heights of 50, 100, 300, 400, 500, 700, 800, 900, 1 000, 1 100, 1 380, 1 480, and 1 580 mm above the burner rim. The propane flow rates used were 5–12 $dm^3\ min^{-1}$. The FB flames were formed with all the walls removed, one wall in place, and two parallel walls in place. The measured flame heights were compared with flame heights of FB tests using the Thomas, Steward, Heskestad, and McCaffrey flame height correlations.

The propane FW and FB studies focused on developing a deeper understanding of the fire dynamics for various apparatus configurations. Specifically, experiments were performed to study the effect of inlet gap size, number of gaps, burner diameter, and HRR on FW

dynamics and stability in a fixed-frame apparatus. Propane was used as the fuel in these studies because gaseous fuels allow the system to operate under stable conditions for a long period of time and permit direct adjustment of the heat release rate.

3.3. Wood Crib Experiments

Propane experiments enable the study of the inherent dynamic effects caused by the fire whirl. Studying crib fires extends the work of gaseous fuels by including the effects of spread through a structured fuel source and formation of the FW above a solid fuel.

Cribs of yellow poplar hardwood (*Liriodendron tulipifera*), which is knot-free, were built and placed in an environmental chamber at 20°C and 50 % relative humidity for ten days, which resulted in approximately a 9 % moisture content. The moisture content was determined using ASTM D4442-92 (Standard Test Methods for Direct Moisture Content Measurement of Wood and Wood-Base Materials). Method B—"Secondary Oven-Drying Method with a precision of ± 1 %" was used. The moisture content is reported as an whole number. For the six-inch cribs, each crib was built by gluing n square cross-section sticks of thickness $b = 12.7$ mm and length $l = 152.6$ mm per layer with equal spacing s between each stick. All cribs had an aspect ratio (stick length/thickness) of 12. The variation in n resulted in cribs with different porosities ε. Each crib had $N = 6$ layers giving a height $h = 76.2$ mm. A typical crib is shown in Fig. 3-2.

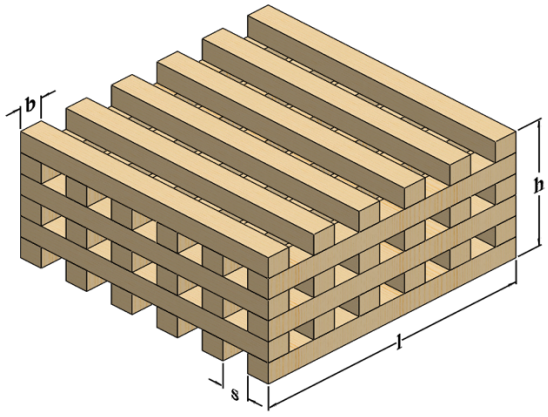

Figure 3-2: Schematic of a typical crib showing important dimensions.

The base plate of the FWG apparatus had an opening to accommodate a weighing platform, attached to a 20 kg top loading balance (Radwag WLC 20/A2). The cribs were placed on top and weight-time data was collected at a rate of 14 samples per second, with an accuracy of 0.1 g. This platform had a small central ignitor cup, the top of which was flush with the base, in which 2 mL of ethanol and a wick were used to initiate each propagating fire. The fire whirls were produced by setting the air gaps to 450 mm high × 65 mm wide, which resulted in stable FWs. For obtaining data on cribs without the formation of a FW, *i.e.*, FB crib fires, the front and rear tempered glass panels were removed.

As before, thermocouples (T1–T8) were positioned at heights of 50, 100, 300, 500, 700, 900, 1 000, and 1 100 mm. Radial measurements were taken from the centreline (0 mm), quarter of the crib (38 mm), crib edge (76 mm), and outside of the crib (114 mm) for the FWs, while for the FB crib fires they were taken from the centreline and staggered between the three other positions.

The thermocouples were interfaced to a PC via a National Instruments DAQ module (NIcDAQ-9174; in conjunction with a NI-9213 thermocouple module). Data acquisition

was handled through a LabVIEW® program which averages 10 samples from each instrument and records them every 1.2 s. All data was stored in an Excel spreadsheet for data analysis. No corrections were made for radiation.

A GoPro HERO4 Silver camera and a webcam (Logitech C920 HD pro Webcam 1080p) were used to record the flame spread rate, flame shape, and flame height.

The second set of experiments was completed at DCTF with the hood removed. Three sizes of crib were used with stick lengths l of 76.2, 152.6, and 228.6 mm (3, 6, and 9 inch). Each crib had $N = 6$ layers giving heights h of 38.1, 76.2, and 114.3 mm. Thirteen type K thermocouples were positioned at heights of 50, 100, 300, 400, 500, 700, 800, 900, 1 000, 1 100, 1 380, 1 480, and 1 580 mm. Measurements were taken from the centreline (0 mm) and edge of the crib (38.1, 76.2 and 114.3 mm). The weight-time data was collected at a rate of 5 samples per second.

3.4. Data Processing

3.4.1. Flame height

The flame height was captured using a GoPro HERO4 Silver camera, and videos were exported into MATLAB for subsequent partitioning into frames. The extracted images were cropped at a width of 40 cm (leaving 20 cm on either side of the vertical centreline through the crib) and a height of 120–130 cm from the base of the burner/crib. A typical cropped image of the visible flame is shown in Fig 3-3(a). Flame heights were determined using a customized color threshold. The filtering process produced images with a black background as shown in Fig. 3-3(b). The flame shape was determined using contour lines,

and the flame height was estimated from the maximum vertical dimension (*i.e.,* maximum y-coordinate). The maximum vertical coordinate on the flame contour in each image (one per second) was converted to centimetres using the known pixel size (pixels/cm).

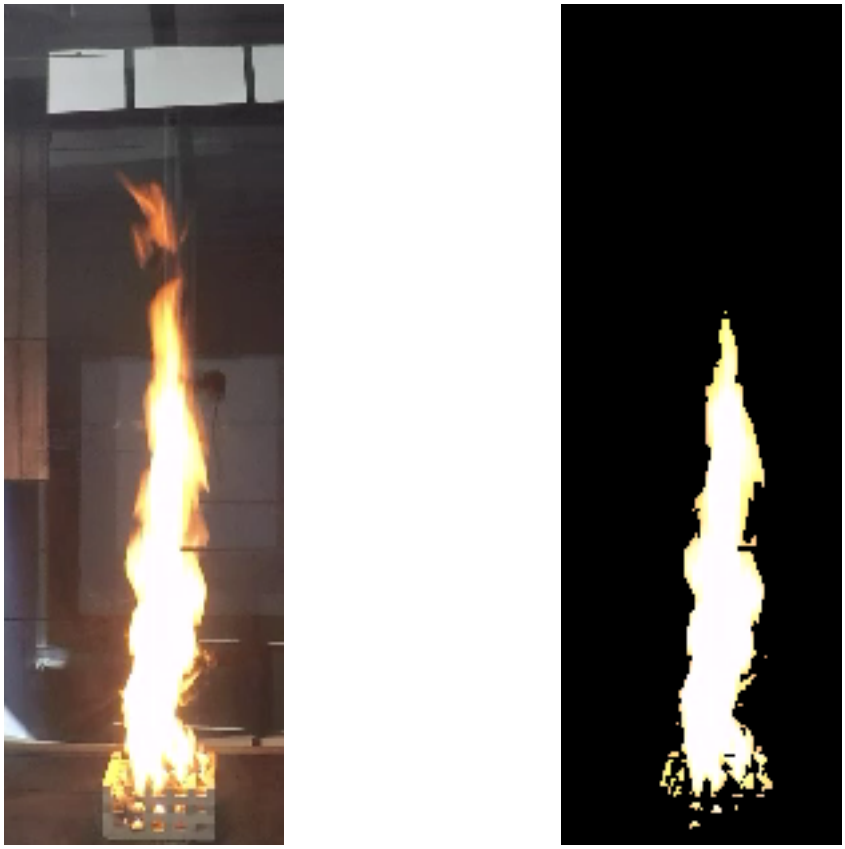

(a) (b)

Figure 3-3: Examples of video images used to determine flame heights: (a) cropped image of the visible flame, and (b) colour threshold image of the flame.

Figure 3-4 shows a comparison between the instantaneous flame heights of FW and FB propane fires. The flame heights fluctuate about a mean value, with the FW average being greater than the FB average.

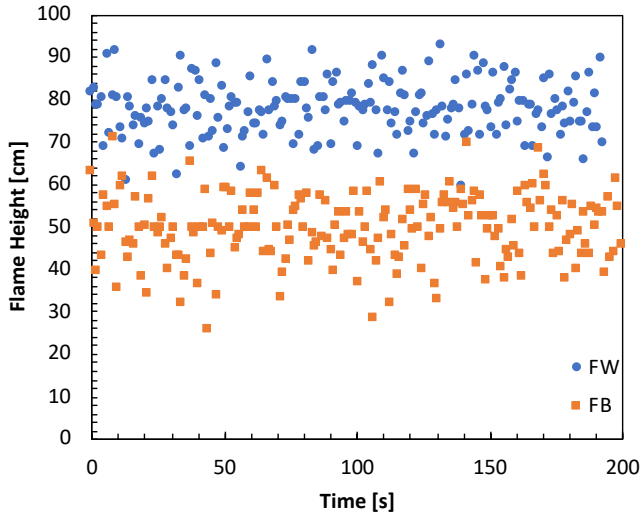

Figure 3-4: Instantaneous flame height data for FW and FB propane fires using 6 in (154.1 mm) diameter burner with an HRR of 8.3 kW.

A typical set of flame height data determined from the video frames is shown in Fig. 3-5(a). The mean flame height for cribs was determined from intermittency data during the quasi-steady burn period as shown in Fig. 3-5(b). Observation of the video of the fire shows that the luminosity of the lower part of the flaming region appears quite steady, whereas the upper part is somewhat intermittent. Figure 3-5(b) has been used to define the mean flame height *H*. It shows the variation of flame intermittency *vs.* height, which is defined as the fraction of time that part of the flame exceeds a particular height. The intermittency decreases from unity well within the flame, to lesser values in the intermittent flame region, and finally reaches zero outside the flame region. The significance of the mean flame height *H* is that it is the distance above the base where the intermittency has dropped to 50 %. Thus, the mean flame height indicates the level where the combustion reactions are essentially complete, and the inert plume begins. Determination of mean flame height based upon intermittency is consistent with flame heights that are averaged by eye, although tending to be slightly lower than visual observation (Heskestad, 2016). Since cribs

of the same geometrical configuration have slightly different quasi-steady burning rates and flame heights, all the flame height data from cribs with the same configuration were "binned" and H was determined from intermittency data rather than averaging values from tests with individual cribs. In the case of crib FWs, a minimum of four tests for each geometrical configuration was conducted. For the FB experiments, two tests were conducted for each geometrical configuration.

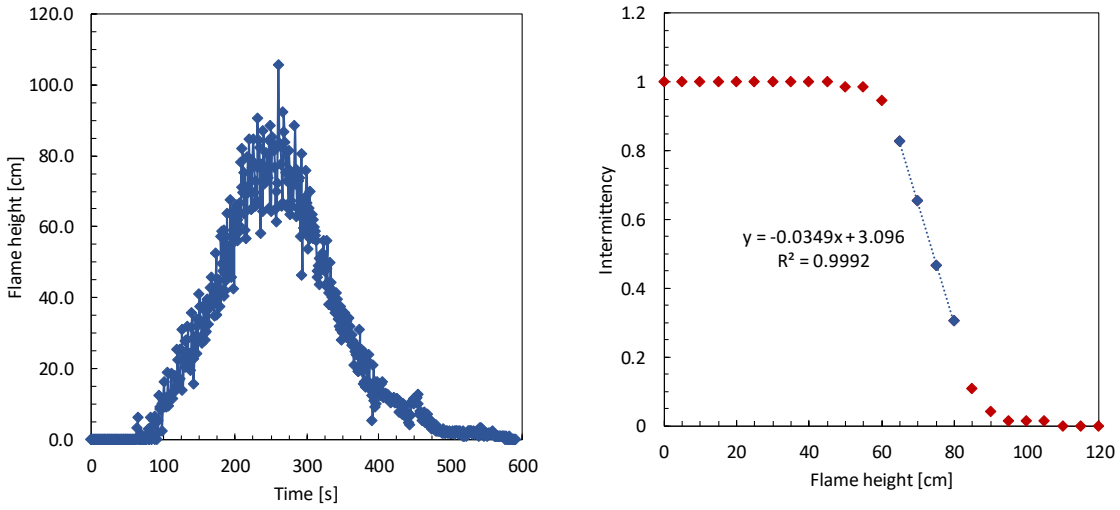

(a) Height *vs.* time (b) Intermittency *vs.* height (225–300 s)

Figure 3-5: Flame height data for a 6 in (152.6 mm) crib with $n = 6$ with a fire whirl.

Three distinct flame regions have been observed with FBs and FWs—the continuous, intermittent, and plume regions. The continuous region is below $z/H = 0.7$, where z is the axial height and H is the flame height. The intermittent region is in the range of $0.7 < z/H < 1.2$, where 1.2 represents the fluctuation of luminous flame tip (Tohidi *et al.,* 2018). The plume region is above the flame tip where the hot gases disperse.

3.4.2. Flame precession and flame spread

The flame precession and spread rate were examined by using a webcam (Logitech C920

HD pro Webcam 1080p), and the videos were exported into a MATLAB script that separated them into frames. The flames in the stable FWs experienced small oscillations in their visible height, and they precessed anticlockwise irregularly around the burner.

The flame precession images from the videos were analyzed to estimate the mean horizontal position and the maximum extent of the flame boundary. The image processing procedure and results from this analysis are summarized in Fig. 3-6. Videos of at least two minutes were recorded for each experiment after stabilization. Frames were extracted every $^1/_3$ s from the videos and the frames were cropped to a width of approximately 20 cm and a height of approximately 30 cm.

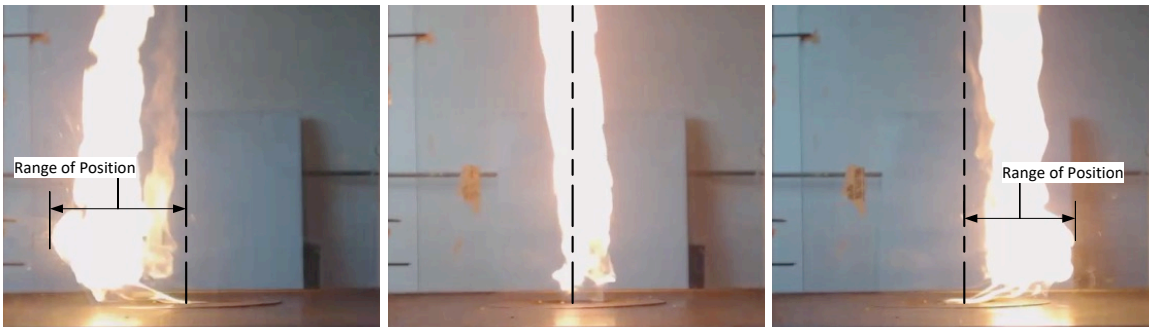

Figure 3-6: Cropped images of the wandering effect for the fire whirl experiment.

Figure 3-7 shows an example of a cropped image. Image analysis was used to convert the flame profile into a binarized image (Fig. 3-7(b)). The horizontal minimum and maximum extents of the flame and its mean horizontal position were calculated from the binarized image and recorded for each frame using an automated image processing code written in MATLAB.

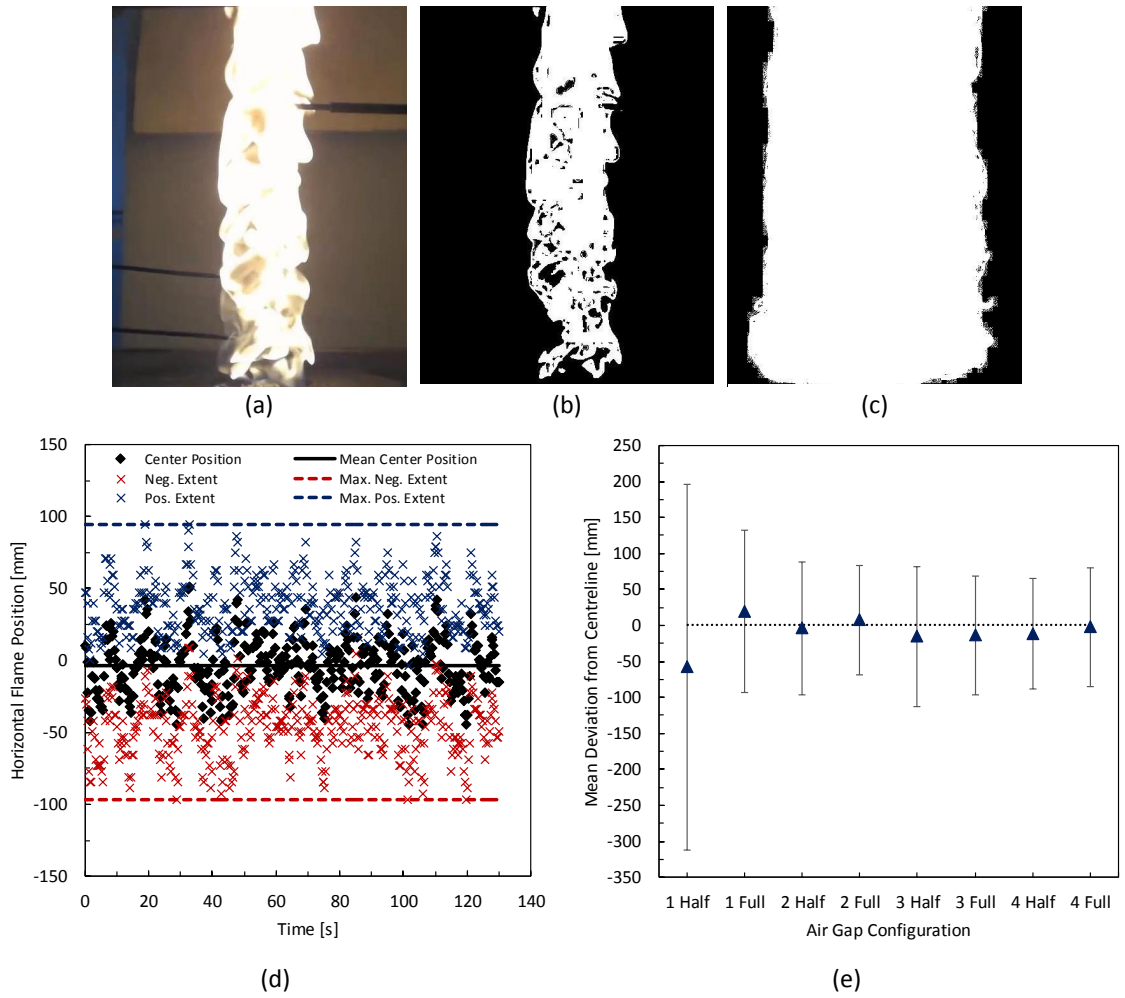

Figure 3-7: Flame wandering data showing (a) an instantaneous image of a flame, (b) a binarized instantaneous image of a flame, (c) the maximum extents of flame motion for the 2 inlet half open configuration, (d) the temporal variation of mean flame and maximum horizontal flame extent for the 2 inlet half open configuration, and (e) the mean position and range of motion for various configurations.

The filtered sum of the binarized frames was used to generate a visualization of the maximum extents of the flame (Fig. 3-7(c)). Figure 3-7(d) shows the time series of recorded flame positions and flame extent data for the two inlet half open experiment with an 8.3 kW HRR. Figure 3-7(e) shows a comparison of the data from the 8.3 kW experiments for the 3 in (77.9 mm) diameter burner with full height and half height air gaps with various number of openings having a gap width of 64 ± 5 mm. The error bars indicate

the global minimum and maximum of the horizontal location of the flame and the triangles indicate the mean horizontal flame position. Figure 3-8 shows a flame precessing around the centreline and is an example of how the range of position is collected.

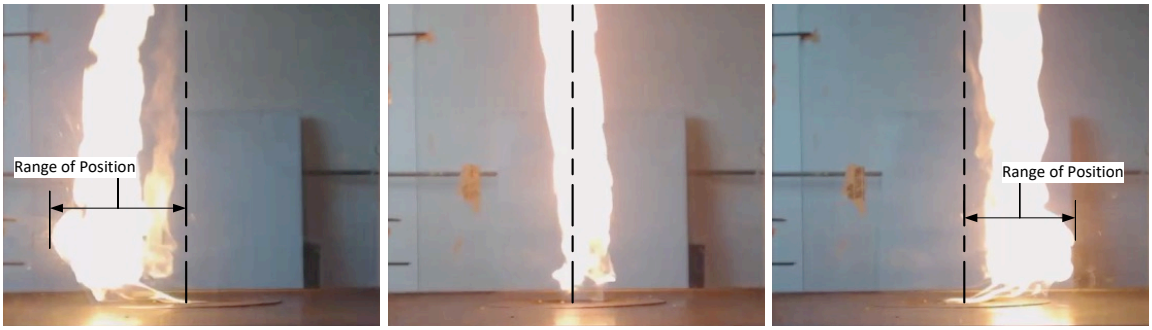

Figure 3-8: Cropped images showing the wandering effect observed in FW experiments.

3.4.3. Wood crib spread rate

The spread rate data was collected by placing one frame per second into Image J software. The software identified where the flame was and as time passed the flame grew in width, which was recorded into a spreadsheet. Figure 3-10 is the plotted flame width *vs.* time, and the slope of graph represents the spread rate (cm s^{-1}).

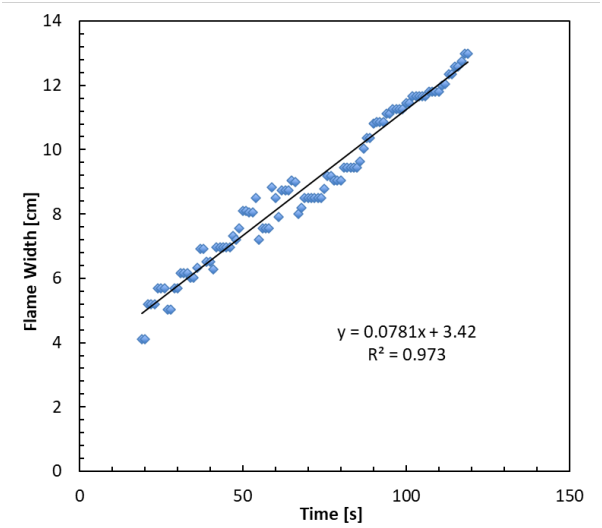

Figure 3-9: Raw data of the spread rate for a 6 in (152.6 mm) crib (n = 4) fire whirl.

3.4.4. Wood crib burning rate

Figure 3-10 shows the weight-time history for a 6 in (152.6 mm) crib with $n = 5$. The top left panel shows the measured raw weight-time data, which is a decreasing function. However, the noise in the data is masked due to the high sampling rate, and the bottom left panel shows that the data cannot be directly numerically differentiated to yield a burning rate estimate. The top right panel shows the smoothed weight-time data using a Gaussian-weighted moving average filter with 500 data points. This filtering method was chosen because it provided a smoothed burning rate estimate and did not significantly impact the predicted peak burning rate when compared to local linear regression. As shown in the bottom right panel, this smoothed data can be numerically differentiated to give a burning rate estimate. The burning rate during the quasi-steady period was determined through linear regression of the linear portion of the smoothed weight-time data (see top right panel of Fig. 3-10), which gives an average of the peak value of the numerically differentiated smoothed data. The start and end times for the linear regression were 25 seconds on either side of the peak value of the numerically differentiated smoothed data, *i.e.,* a 50 s window around the peak value (see bottom right panel of Fig. 3-10). In all cases, the difference between the average burning rate during the quasi-steady period and the peak (maximum) burning rate determined from the numerically differentiated data, with the exception of the very open-packed cribs (n = 3), was within the range of 0 to 5 %.

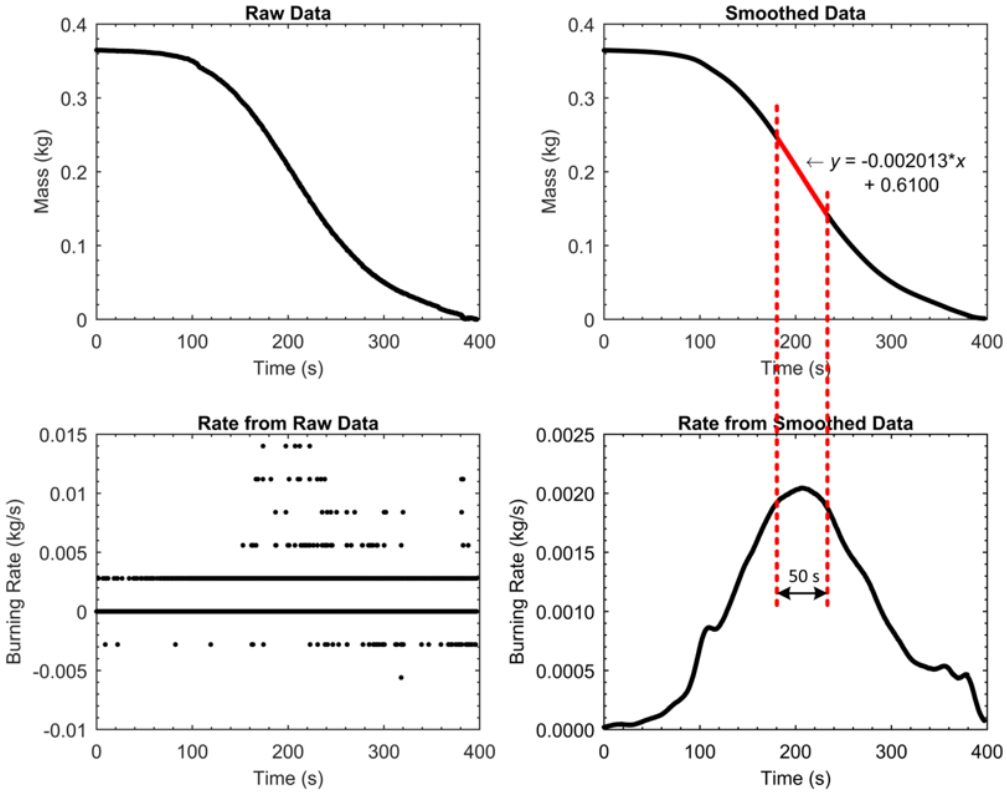

Figure 3-10: Burning rate data for a 6 in (152.6 mm) crib FW experiment with $n = 5$ showing raw data of mass *vs*. time (top left), smoothed data of mass *vs*. time (top right), burning rate computed from the raw mass *vs*. time data (bottom left), and burning rate determined from smoothed mass *vs.* time data.

3.4.5. Thermocouple temperature measurements

The thermocouples were interfaced to a PC via a National Instruments DAQ module (NIcDAQ-9174; in conjunction with a NI-9213 thermocouple module) and was controlled through a LabVIEW® program, which averages 10 samples from each instrument and records them every 2.2 s. All data was recorded in an Excel spreadsheet for data analysis. Similar to the height data, the gaseous flame temperature data had some fluctuation but

produced a relatively flat graph (left side of Fig. 3-11). The crib temperature data produces a parabolic graph (right side of Fig. 3-11).

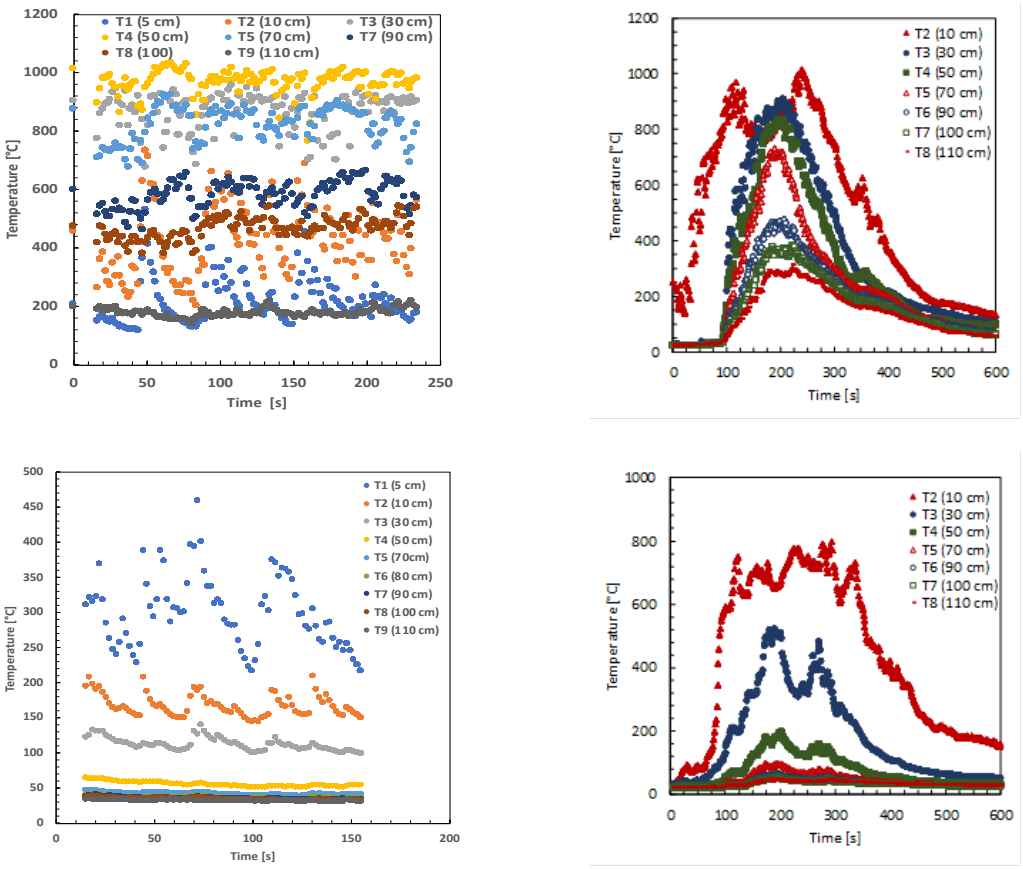

Figure 3-11: Temperature profiles for FW and FB gas and crib experiments with raw data of temperature *vs*. time for gaseous FW (top left), crib FW (top right), gaseous FB (bottom left), and crib FB (bottom right) cases.

The centreline profiles were generated for gaseous FWs and FB fires by averaging 100 seconds of the data. The radial temperature profiles were recorded at 0, 20, 40, 60, and 100 mm. The three regions were examined: (1) the continuous flame, (2) the intermittent flame, and (3) the plume region. The temperature was then plotted according to McCaffrey's correlation, which can be used for intermittent and continuous flame regions with different constants, as shown in Fig. 3-12.

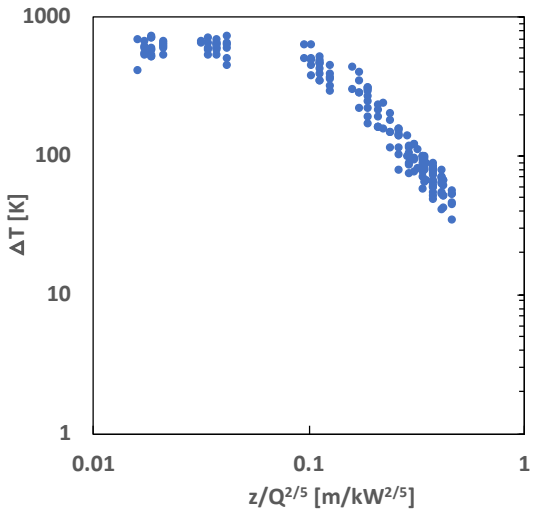

Figure 3-12: Free burning centreline temperature profiles for various propane experiments.

The average temperatures within the crib flames were calculated by taking 10 % of the time from when the temperature starts to climb to the peak, shown by the dotted lines in Fig. 3-13. Then using that time to average the temperature at the peak. For example, Fig. 3-13 shows the crib beginning to climb at approx. 50 s and reaches the peak at 250 s. Therefore, 10 % of this would be 20 s. The temperature would be averaged from 230-270 s. With crib FWs, there were four regions: (1) combustion within the crib, (2) the continuous flame, (3) the intermittent flame, and (4) the plume region. The error bars were calculated using the root-mean-square error (RMSE) method. The crib data was plotted in the same manner as the data for the propane flames.

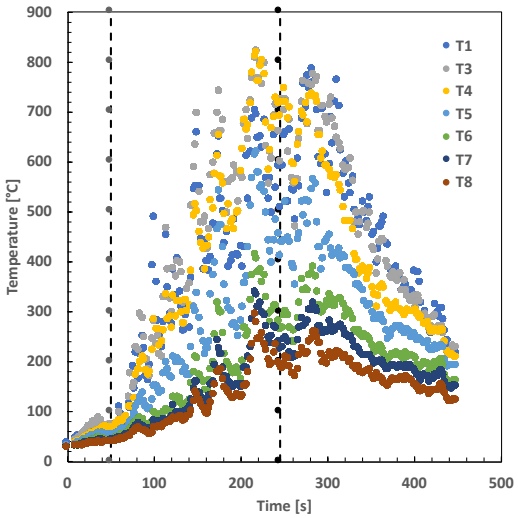

Figure 3-13: Centreline temperature data of the 6 in (152.6 mm) crib (n = 6) fire whirl.

Chapter 4: Numerical Methods

Fire Dynamics Simulator (FDS) (FDS, 2022) was used to simulate the propane FWs with different HRRs and FWG configurations. The chamber modelled was a fixed-frame facility with four walls, two aluminum and two glass. The gap size was varied on a case-by-case basis. The objective was to compare simulation results from FDS with data from the propane FW experiments and to identify limitations of and areas for improvement in the adopted modelling approaches. The primary focus of this study was on fire whirl formation, stability, temperature profiles, and flame height.

4.1. Governing Equations

The most common CFD-based approaches for modelling turbulent fires are based on RANS (Reynolds-averaged Navier-Stokes), URANS (unsteady RANS), and LES (large-eddy simulation) methods. Direct numerical simulation is normally not feasible for large-scale fires. In this study, an LES turbulence model was employed. In LES, the goal is to resolve the large-scale unsteady energy-carrying geometry-dependent anisotropic eddies, but the effect of the smallest scales in the flow are included through the sub-grid scale (SGS) model.

FDS is an LES code that solves the low-Mach number equations, with emphasis on transport of smoke and heat. Due to the large scales of fires, it is often not possible to resolve all geometry-dependent anisotropic eddies. Therefore, the default settings within FDS are tuned towards a very large-eddy simulation (VLES), where more of the scales are handled by the SGS model. All simulations in this work were conducted using FDS version

6.7.0. The technical details of the mathematical models used in FDS are described in the FDS Technical Reference Guide (2022) and will not be repeated in this section.

4.2. Model Implementation

A successful model should capture both the qualitative and quantitative aspects of a fire whirl. Qualitative observations should include the transition from a buoyant diffusion gas flame to a stable fire whirl, and the stability of the fire whirl. If the qualitative properties of the simulation match experimental observations, then the quantitative properties—*e.g.*, flame height and temperature profiles—should also reasonably match the experimental data.

4.2.1. Model parameters

Thermocouple probes with the same properties as those in the experiments were used to record temperatures within the simulation. Preliminary tests were performed with different SGS and wall modelling approaches, but the default Deardroff model was found to be the most suitable. In this model, the eddy viscosity v_t is calculated using the following expression:

$$v_t = C_v\sqrt{k_{sgs}\Delta} \tag{4-1}$$

where C_v is an empirical constant with a default value of 0.1, Δ is a length on the order of size of a grid cell, and k_{sgs} is the unresolved (sub-grid scale) kinetic energy which is estimated with an algebraic closure based on scale similarity.

The default combustion rate model in FDS is a mixing-controlled, mixture-fraction model based on the eddy dissipation concept (EDC). The default FDS combustion model settings

were used in this study, and propane was specified as the fuel. The default FDS settings were also retained for solving the radiative transport equation (RTE).

4.2.2. Geometry

Various FWG chamber configurations were simulated. In all cases, the total geometry (chamber and surroundings included within the simulation domain) for the simulation domain had a square base of 1 000 mm × 1 000 mm and a height of 4 500 mm. The space around the outside of the chamber was included within the simulation domain to ensure more realistic inlet/outlet conditions. An annotated image of the simulation domain is shown in Fig. 4-1. Only a portion of the top of the domain is shown to facilitate visualization of the chamber. The aluminium (grey) and glass (blue) panels are shown in the image, and the provided dimensions for the chamber correspond to one of the configurations used for experiments.

Burners were initially modelled using a square inlet having an equivalent cross-sectional area to the experimental burners. However, initial simulations showed that a square inlet required significantly more mesh resolution than a circular inlet to form a stable whirl. Therefore, a circular inlet was used for all simulations presented in this work. The FWs were found to stabilize within the first 15 s of the simulation, and all simulations were run for at least 45 s. Data were averaged after the simulations has reached a pseudo-steady-state for 30 s in the interval 15–45 s.

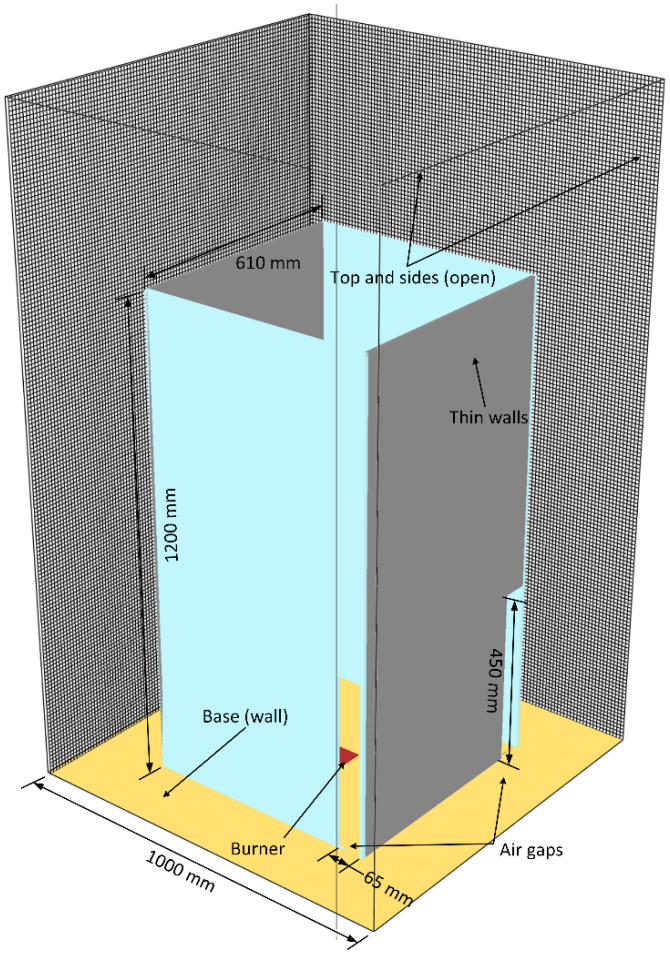

Figure 4-1: Annotated image showing one of the simulated FWG configurations and the simulation domain (top of the simulation domain has been cropped to facilitate visualization).

4.2.3. Mesh dependence

A refinement study was performed using five computational meshes containing 562 500 (M1), 1 386 000 (M2), 1 964 880 (M3), 2 573 136 (M4), and 3 126 096 (M5) cells to analyze the impact of mesh resolution on predictions. The finer meshes had significantly higher resolution in the vicinity of the flame. Therefore, although the mesh cell count is not drastically increased compared to the coarser meshes, the computational demand was significantly higher due to the lower required time steps.

To test mesh refinement, simulations were performed for a 3 in (77.9 mm) burner diameter, four air gaps of 450 mm height × 65 mm width, HRR of 11.1 kW, and a wall height of 1 200 mm. It was found that only the M4 and M5 meshes predicted stable fire whirls. To ensure the best possible results considering available computational resources, the M5 mesh was used for all other simulations.

The FDS validation guide (FDS, 2022) provides the following equation to calculate the characteristic fire diameter D^*:

$$D^* = \left(\frac{\dot{Q}}{\rho_o c_p T_o \sqrt{g}} \right)^{2/5} \tag{4-2}$$

where $\dot{Q}$ is the HRR, ρ_o is the ambient air density, c_p is specific heat, T_o is the ambient air temperature, and g is gravitational acceleration. The FDS validation guide (FDS, 2022) suggests calculation of a plume resolution index as $D^*/\delta x$, where δx is the length of the cells spanning the fire. For mesh M5 at a HRRs of 8.3, 11.1, and 16.7 kW, the plume resolution index based on the cell length in the vicinity of the fire is 56.5, 63.4, and 74.6 respectively. These values are in the high range (*i.e.*, good flame resolution) compared to most of the validation cases provided in the FDS validation guide. The values are also equivalent to, or higher than, similar simulations reported in recent studies in the literature (Gao, 2021; Fang, 2020).

Images of mesh M5, including the overall domain and a close-up view of the flame region are provided in Fig. 4-2.

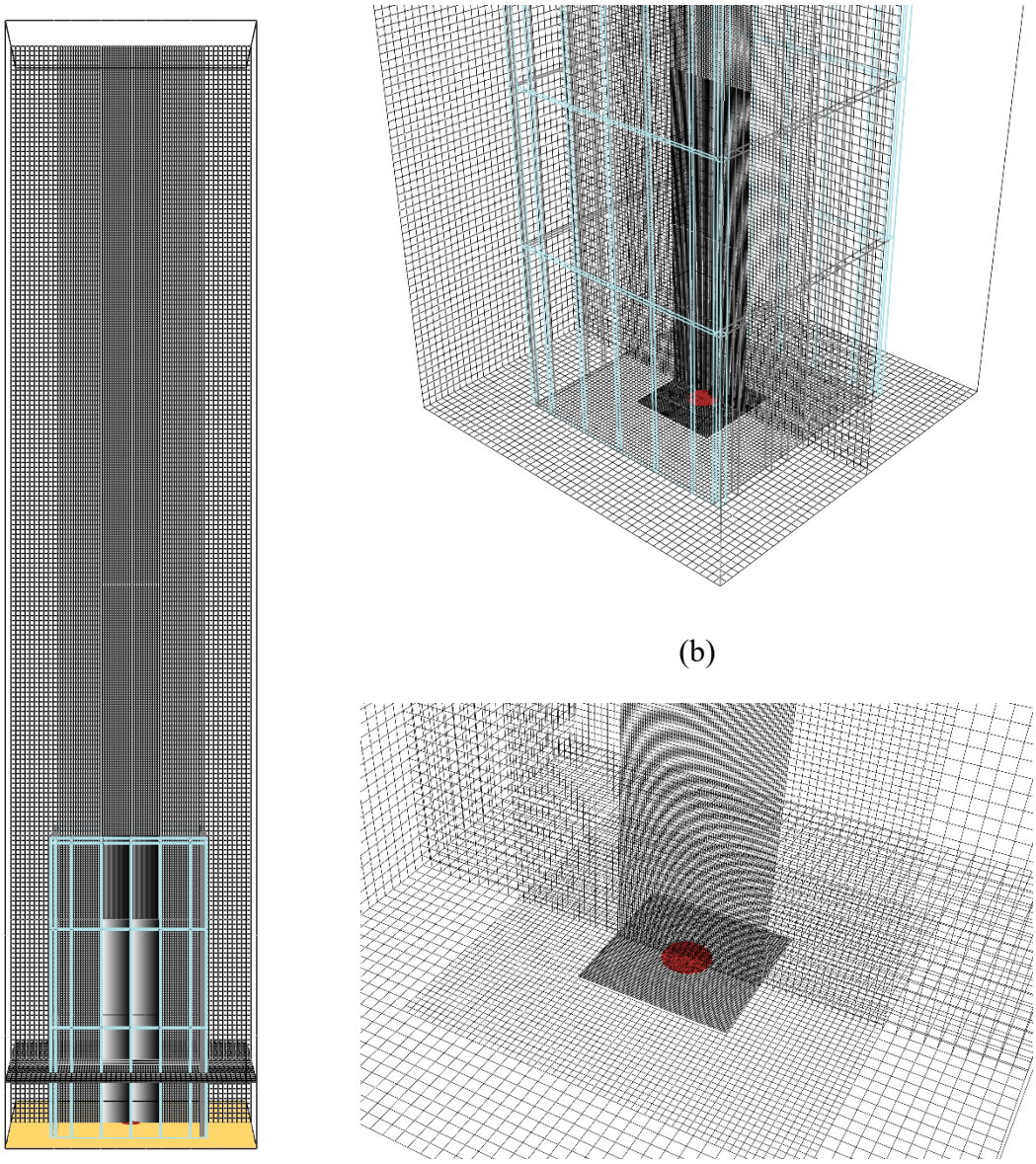

(a) (b) (c)

Figure 4-2: Images of mesh M5 showing (a) the overall domain, (b) a close-up of the flame region, and (c) a close-up of the burner region. Mesh length size across the burner is 2.5 mm.

4.3. Summary of Simulations

The simulation results were compared with the experimental data to validate the selected models. Table 4-1 lists the simulation cases that were completed in this work in addition to the mesh refinement studies.

Table 4-1: Summary of simulation cases completed in this work.

Chamber wall height analysis			
Burner size (in)	**HRR (kW)**	**Wall height (m)**	**Gap size (four inlets if not otherwise stated)**
3	8.3	1.2	Full height × 65 mm
3	8.3	2.6	Full height × 65 mm
3	8.3	4.0	Full height × 65 mm
3	11.1	1.2	Full height × 65 mm
3	11.1	2.6	Full height × 65 mm
3	11.1	4.0	Full height × 65 mm
3	16.7	1.2	Full height × 65 mm
3	16.7	2.6	Full height × 65 mm
3	16.7	4.0	Full height × 65 mm
Mesh refinement study			
3	11.1	1.2	450 mm height × 65 mm
Gap width study			
3	11.1	1.2	Full height × 65 mm
3	11.1	1.2	Full height × 105 mm
3	11.1	1.2	Full height × 205 mm
3	11.1	1.2	Full height × 305 mm
Number of inlet(s) study			
3	11.1	1.2	One inlet, 450 mm height × 65 mm
3	11.1	1.2	One inlet, Full height × 65 mm
3	11.1	1.2	Two inlets, 450 mm height × 65 mm
3	11.1	1.2	Three inlets, 450 mm height × 65 mm
Burner size and HRR study			
2	11.1	1.2	450 mm height × 65 mm
6	11.1	1.2	450 mm height × 65 mm
2	8.3	1.2	450 mm height × 65 mm
6	8.3	1.2	450 mm height × 65 mm
2	16.7	1.2	450 mm height × 65 mm
6	16.7	1.2	450 mm height × 65 mm
3	8.3	1.2	450 mm height × 65 mm
3	16.7	1.2	450 mm height × 65 mm

Chapter 5: Dynamics of Propane Fire Whirls

In this chapter, the different flame height correlations for FB fires are compared with data from this study and literature data. This analysis is followed by an investigation of how changing the fuel flow rate, gap size, and number of inlets impacts FW formation and stability, FW diameter, and FW height.

5.1. Free Burning Flame Heights

The flame height data for FB buoyant propane diffusion flames was plotted according to the Thomas correlation (Thomas, 1960). The mean flame height was normalized by the burner diameter. Figure 5-1 shows the data for completely unconfined flames (*i.e.,* with no walls affixed to the apparatus), with one wall, and with two parallel side walls attached (*i.e.,* partially confined with the front and rear glass panels removed).

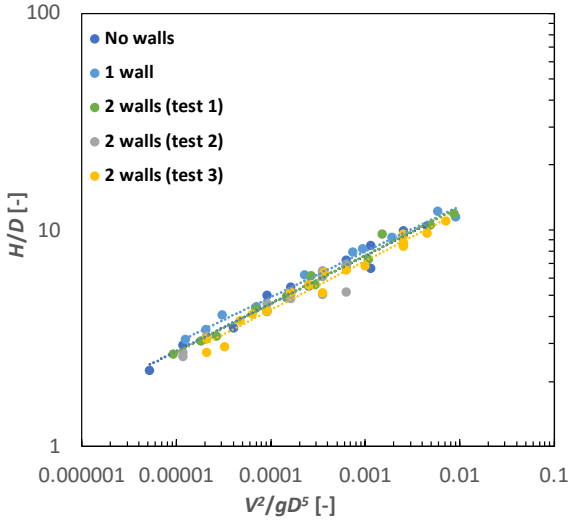

Figure 5-1: The FB propane fires with no walls, 1 wall, and 2 walls plotted according to the Thomas correlation.

The effect of the side walls on the flame height was negligible, so all sets of data can be considered as FB and are fitted by a power law:

No walls $$H/D = 34.85\left(\dot{V}^2/gD^5\right)^{0.22} \quad r^2 = 0.975 \qquad (5\text{-}1a)$$

1 wall $$H/D = 34.1\left(\dot{V}^2/gD^5\right)^{0.21} \quad r^2 = 0.982 \qquad (5\text{-}1b)$$

2 walls $$H/D = 35.03\left(\dot{V}^2/gD^5\right)^{0.22} \quad r^2 = 0.980 \qquad (5\text{-}1c)$$

Overall $$H/D = 35.07\left(\dot{V}^2/gD^5\right)^{0.22} \quad r^2 = 0.977 \qquad (5\text{-}2a)$$

Subsequently, all the data points were plotted for all four flame height correlations discussed in Chapter 2 to discover which flame height correlation would be most suitable going forward. Figure 5-2 shows the data for FB propane flames correlated using (a) Thomas's correlation, (b) Steward's N_{co} parameter, (c) Heskestad's N parameter, and (d) McCaffrey's Q^* on logarithmic axes.

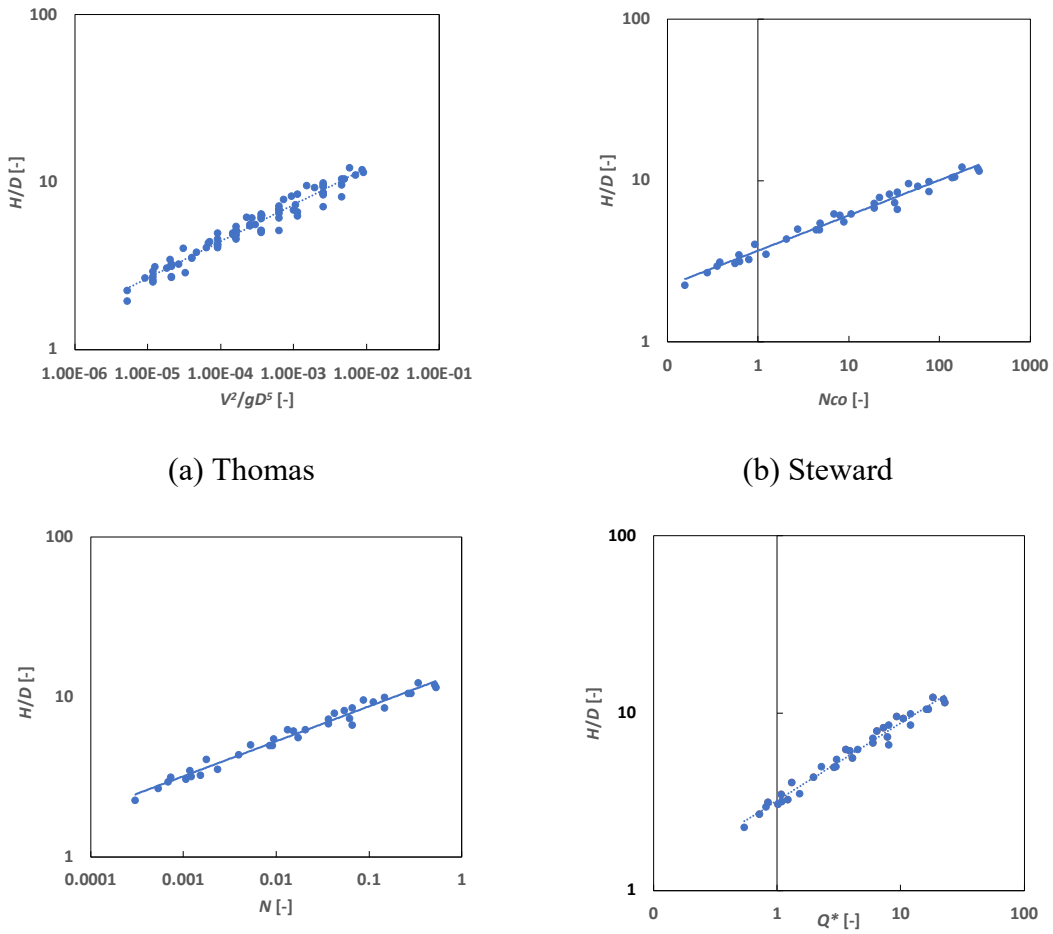

(a) Thomas (b) Steward

(c) Heskestad (d) McCaffrey

Figure 5-2: Free burning buoyant propane diffusion flame height data plotted according to four common correlations.

The Thomas correlation is shown by Eq. (5.2a). The other three flame height correlations from Fig. 5-2 are given by the following expressions:

Steward's correlation	$H/D = 3.685{N_{co}}^{0.22}$	$r^2 = 0.977$	(5-2b)
Heskestad's correlation	$H/D = 14.44(N)^{0.22}$	$r^2 = 0.977$	(5-2c)
McCaffrey's correlation	$H/D = 3.208(Q^*)^{0.44}$	$r^2 = 0.977$	(5-2d)

Heskestad's N parameter is based on the Thomas (1960) correlation modified by the properties of the fuel and air so as to be applicable to all fuels. Steward's N_{co} parameter is comprised of Thomas's correlation modified by terms containing the inverse volumetric expansion ratio due to combustion and the stoichiometric air to fuel mass ratio. It is therefore not surprising that they all resulted in the same exponent and value of r^2 as the Thomas correlation but with a different constant. Data plotted according to McCaffrey's Q^* resulted in an exponent twice that of the Thomas, Steward, and Heskestad correlations. However, the r^2 is the same as the Thomas correlation.

As pointed out by Zukoski (1995), because the heat of combustion per unit mass of air $(\Delta H_c/\gamma)$ is approximately constant for most gaseous hydrocarbon fuels and hydrogen, incorporating the term $\left(\gamma c_{P_\infty} T_\infty/\Delta H_c\right)$ in N_{co}, N, or Q^* makes little difference in the flame height correlations. Furthermore, the scatter in experimental data (visual flame height *vs.* flame heights from intermittency) is too large to allow one correlating parameter to be chosen over another. Therefore, going forward any of the flame height correlations could be considered.

Several researchers have plotted flame heights for a range of fuel types and HRR. Table 5-1 and Fig. 5-3 compares a number of these experiments with the present work:

Table 5-1: Experimental studies on FB flame height using propane fuel.

Reference	Set-up
Sugawa and Sakai (1997)	Investigated the flame height, flame width, and radiation to an adjacent vessel from a jet flame. Propane flow rates of 100, 200, and 400 dm3 min^{-1} (1.67×10^{-3}, 3.33×10^{-3}, and 6.67×10^{-3} m^3 s^{-1}) through pipes with bore diameters of 6.5, 9.2,12.7, and 27.6 mm were used.
Hu *et al*. (2013)	Measured flame height and lift-off distance of propane turbulent jet diffusion flames from nozzles with diameters of 4, 5, 6, 8, and 10 mm. Experiments were performed at Hefei, China (50 m, 100 kPa) and Lhasa, Tibet (3 650 m, 64 kPa).
Zhang *et al*. (2014)	Measured the flame extension of a vertical jet flame impinging on a horizontal surface above the flame, such as a ceiling. They also measured the unconfined flame height (*i.e.,* without the plate above the flame). A 14 mm diameter nozzle was used and five HRRs of 0.47–2.36 kW were tested.
Huang *et al*. (2019)	Measured the flame height using a circular burner size with diameter of 34 cm and HRRs of 14.1, 28.3, 42.3, 56.5, and 70.7 kW.
Wang *et al*. (2017)	Measured the flame height in a chamber with two vertical walls that were 1.5 m wide and 3 m high. The propane was delivered through nozzles with diameters of 3, 6, and 10 mm. The volumetric flow rates were from 1 to 9 SLPM.

Free burning propane flame height data from various researchers was plotted in Fig. 5-3 using the Thomas correlation. All data are reasonably well correlated, with the largest burner diameter giving the smallest values of H/D and the smallest burner diameter giving

the largest values of *H*/*D*. Sugawa *et al*. (1997), Hu *et al*. (2013), and Wang *et al*. (2017) correspond to the highest values of $\left(\dot{V}^2/gD^5\right)$, Zhang *et al.* (2014) to intermediate values, and the data from the present work and that of Huang *et al*. (2019) to the lowest values. Sugawa *et al*. (1997) used small burner diameters with very large HRR. Hu *et al*. (2013) and Wang *et al*. (2017) used small burner diameters with medium to small HRR. Zhang *et al*. (2014) used small diameter burners with very small HRR, whereas the present work and that of Huang *et al*. (2019) used large diameter burners with intermediate HRRs, larger than Zhang *et al*. (2014) but smaller than Sugawa *et al*. (1997).

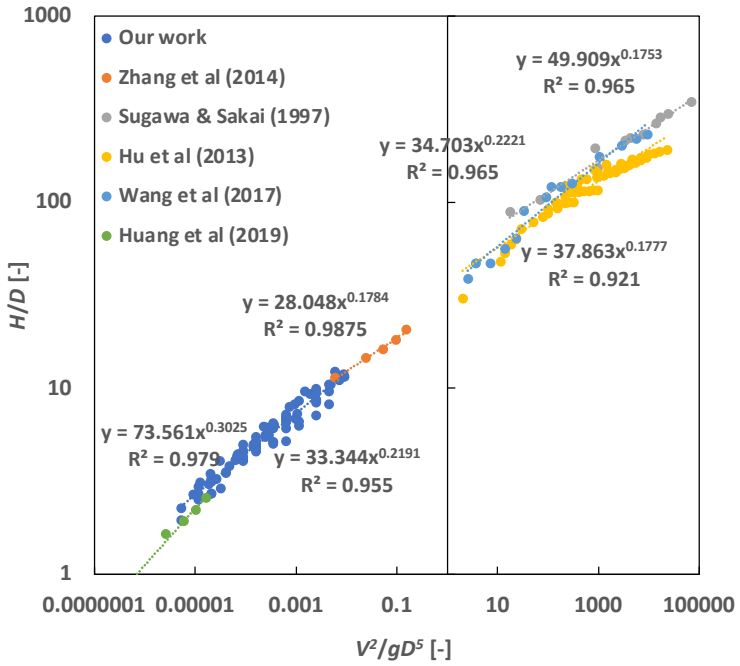

Figure 5-3: Free burning flame height data plotted according to the Thomas correlation.

5.2. Fire Whirl Flame Heights

When observing the difference between FW and FB flame heights, it is apparent that FWs produce a much greater flame height than the FB fires. Also, the diameter of FB flames is

similar to that of the burner diameter D. However, the diameter of the FW flame D_o in most cases is much different than the burner diameter. Furthermore, FWs exhibit a lift height L, as shown in Fig. 5-4, whereas the FB fires do not. This lift height is also present in jet fires, which was investigated by Bradley *et al*. (2016).

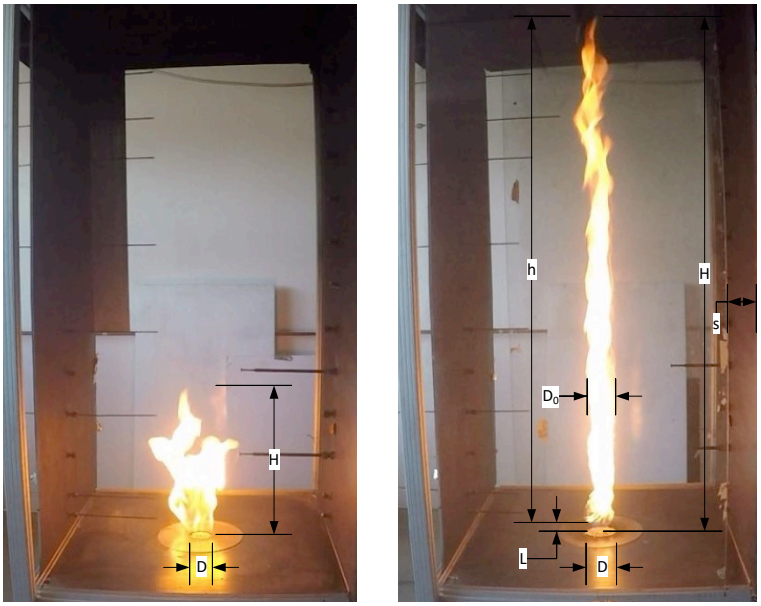

Figure 5-4: Images of free burning (left) and fire whirl (right) flames showing height and diameter for the 2 in (52.5 mm) diameter burner with an HRR of 13.9 kW.

The mechanism that stretches the FW is the buoyant accelerating hot gases from the fire. As the FW is stretched, the flame height increases and causes the diameter of the flame to shrink. This phenomenon is a result of conservation of angular momentum; as the mass moves closer to the centre, the FW spins faster. It was noted that D_o did not vary greatly when D changed, as shown in Fig. 5-5.

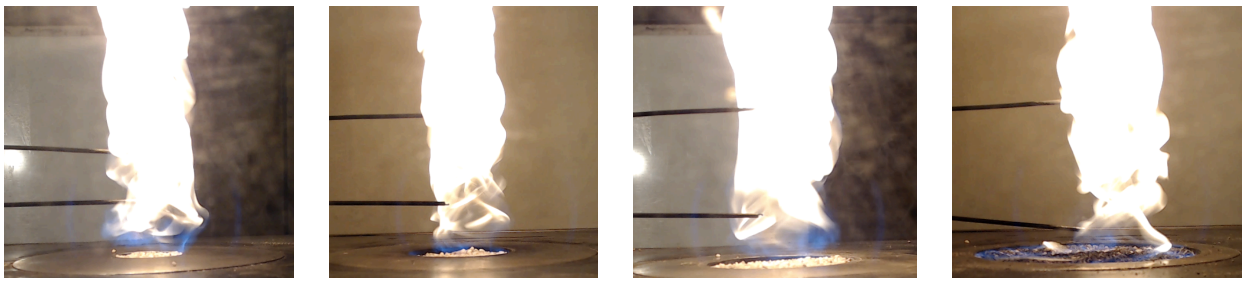

(a) 2 inch (b) 3 inch (c) 4 inch (d) 6 inch

Figure 5-5: The diameter of the fire whirl for approximately 11 kW HRR with different burner diameters.

However, when the HRR increased so did D_o, as shown in Fig. 5-6 and 5-7. There is a strong dependence on HRR, as shown by the fitted correlations provided in Table 5-2.

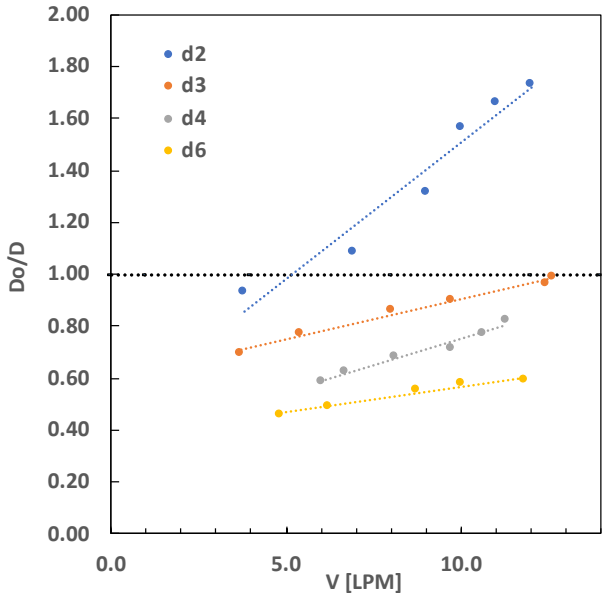

Figure 5-6: Ratio of the FW diameter (D_o) to the burner diameter (D) plotted against the fuel flow rate.

Table 5-2: Correlations of (D_o/D) as a function of propane flow rate from Fig. 5-6.

d2	$D_o/D = 0.105V + 0.460$	$r^2 = 0.946$	(5.3a)
d3	$D_o/D = 0.031V + 0.595$	$r^2 = 0.986$	(5.3b)

d4	$D_o/D = 0.04V + 0.348$	$r^2 = 0.971$	(5.3c)
d6	$D_o/D = 0.02V + 0.367$	$r^2 = 0.969$	(5.3d)

The data on Fig. 5-6 show that in some cases D_o is as low as half the size of D. Keeping the same flow rate (11.1 kW) and changing the burner diameter from 2 in to 6 in, which is 3 times greater, only increases D_o by a factor of 1.29. In comparison, the change of D_o with HRR for a burner diameter of 3 in is shown in Fig. 5-7.

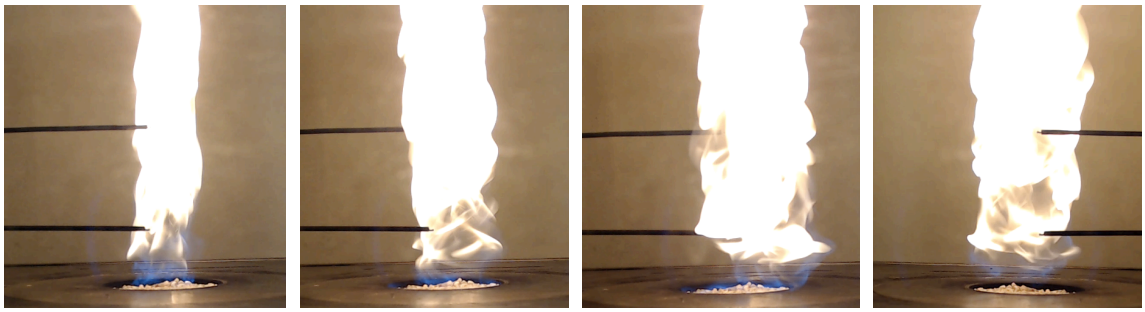

(a) 5.5 kW (b) 11.1 kW (c) 13.5 kW (d) 17.2 kW

Figure 5-7: Change of the diameter of the fire whirl D_o with HRR for the 3 in (77.9 mm) diameter burner.

The FW flame heights were 1.5 to 1.6 times larger than FB flame heights for the same burner size and HRR, as shown in Fig. 5-8. The error bars indicate the standard deviation of the sample size across repeat samples. Additionally, the flame heights did not have a large dependence on the burner diameter. The numerical simulations produced FW flame heights within the error bars of the experimental data. This validates that the model can predict similar flame heights to the test cases and indicates that the flame height is not dependent on the burner size.

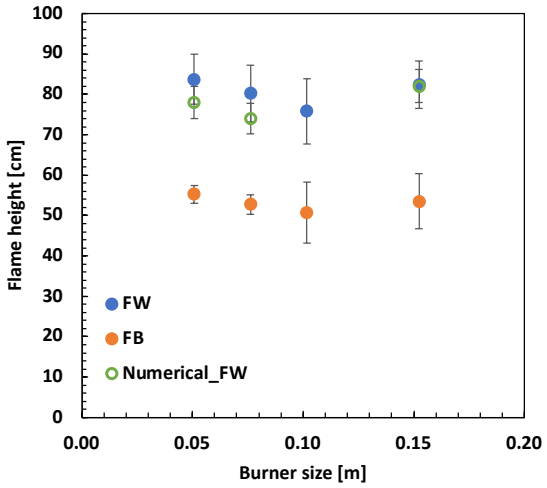

Figure 5-8: Numerical and experimental FW and experimental FB flame height for burner diameters and an HRR of 11.1 kW.

In Fig. 5-9(a), the normalized flame heights H^* were plotted for the experimental FB flames, the FW flames, and Heskestad's correlation for three different HRRs with burner diameters of 52.5, 77.9, 102.3, and 154.1 mm. (2, 3, 4, and 6 in). The experimental FB data was a close match to Heskestad's correlation ($H/D = -1.02 + 3.7\dot{Q}^{*2/5}$), but not for the experimental FW data. The following correlation provides the best fit for the FB data:

$$H^* = H/D = -0.273 + 3.2\dot{Q}^{*2/5} \qquad r^2 = 0.96 \qquad (5\text{-}4)$$

For the FW experiments, the correlation was different by a factor of approximately 1.34, but it still had a $\dot{Q}^*$ dependence of approximately 2/5. The best fit line for this data in Fig. 5-9(a) is expressed by the following expression:

$$H^* = H/D = 4.29\dot{Q}^{*2/5} \qquad r^2 = 0.97 \qquad (5\text{-}5)$$

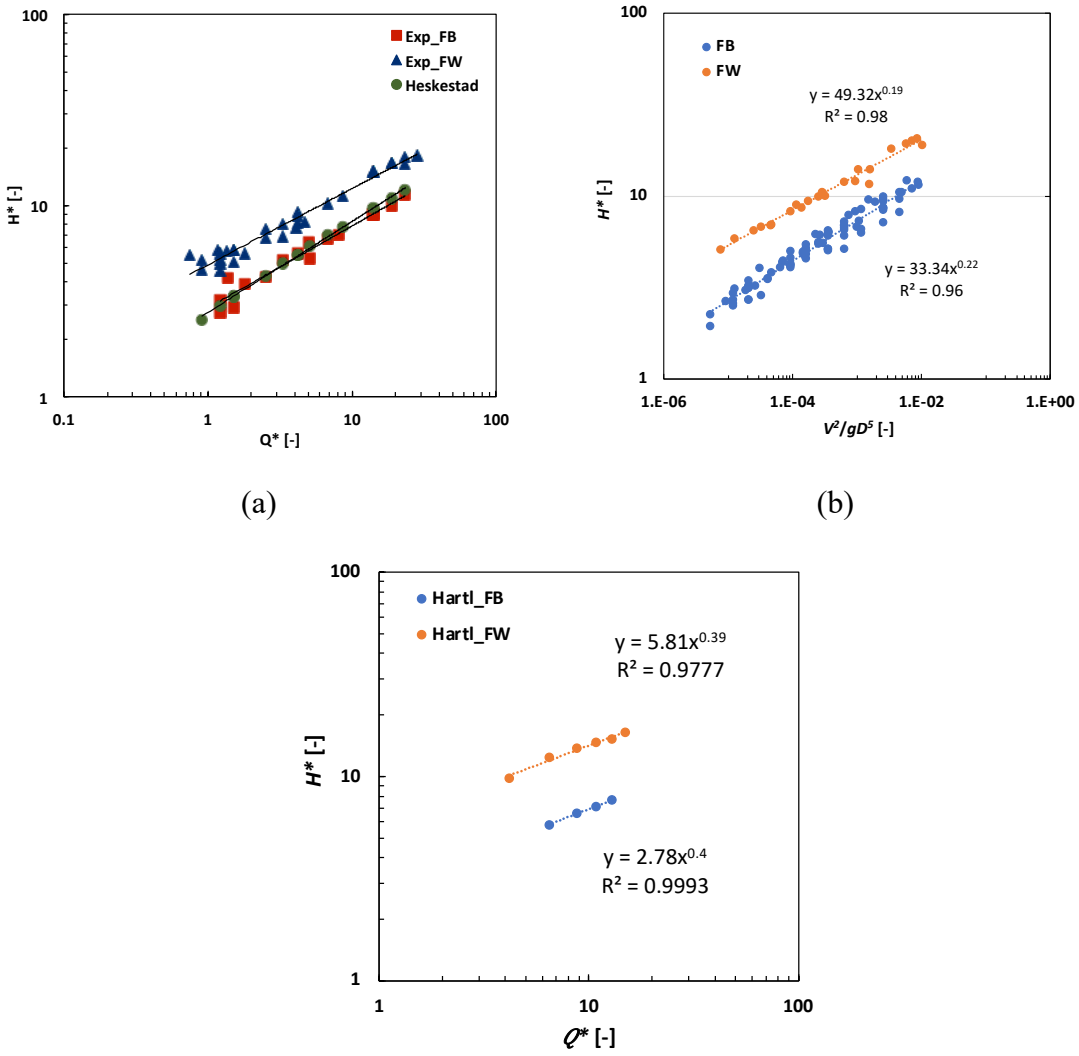

Figure 5-9: Normalized flame height, $H^* = H/D$, for experimental free burning and fire whirl data using (a) Heskestad's $\dot{Q}^*$ correlation, (b) Thomas's correlation, and (c) the experimental data of Hartl *et al*. (2015).

The normalized flame heights for FB fires and FWs were plotted using the Thomas correlations (Fig. 5-9(b)) and a similar trend was observed as before. In Fig. 5-9(c), the experimental data of Hartl *et al.* (2015) for FB and FW flame heights were plotted according to Heskestad's correlation, and comparable trends were observed. Both the FW data from the present work and the data from Hartl *et al.* (2015) are correlated to a power of approximately 2/5 with a coefficient larger than the FB case. The correlation for the FW

data from Hartl *et al.* (2015) was two times larger than that of the FB data.

Chow *et al*. (2015) established a correlation for H^* for pool fire whirls of $H^* = 3.59\dot{Q}^{*2/5}$. The experimental data from the present study and that of Chow *et al.* (2015) both lead to similar results. Zou *et al*. (2017) noted that their FW experimental data was double that predicted by the Heskestad correlations for FB cases and proposed the following two equations for the average flame height.

$$lnH^* = \ln\left[\left[\frac{DC(0.37Q^*)^p}{H_p}\right]\right] + 2.79m\ln\Gamma^* \tag{5-6a}$$

$$H^* = 0.36\Gamma^{*1.11} \tag{5-6b}$$

In these equations, H^* and Q^* are the dimensionless flame height of the fire whirl and the dimensionless heat release rate. $H^* = H/H_p$, where H_p is the dimensionless flame height for free burning flames, D is the fuel tray diameter, $\Gamma^* = \Gamma\sqrt{gD^3}$ is the dimensionless circulation, and C and p are constants.

With all these correlations for proposed flame height of FWs, there is still no general expression established, and many uncertainties remain. In the following sections, the dependence of the flame height on the heat release rate and gap width will be discussed.

5.2.1. Effect of heat release rate

For a single gap size of approximately 65 ± 5 mm wide and 457 mm high, it was observed that the flame height does not vary significantly with the change of burner size. There is

more of a dependence on the HRR than the burner diameter, as shown in Fig. 5-10 and Eq. (5-7). The FW flame heights followed a linear regression with HRR:

$$H = A \cdot HRR + B \tag{5-7}$$

in which A has a range of 2.70–3.80 and B has a range of 60-66 with correlation coefficient of r^2 from 0.91 to 0.99. The error bars show the standard deviation.

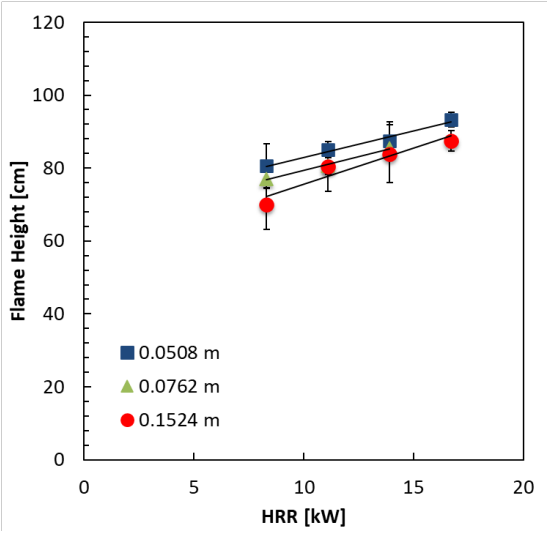

Figure 5-10: The flame height for different burner sizes and HRRs for fire whirls.

Comparing experiments with and without the hood attached to the top of the FWG, the trends were determined to remain the same. However, the flame heights increased by 10–30 % when the hood was removed, as shown in Fig. 5-11(a). The stability of the fire whirl did not change and remained stable throughout all tests. The slope of flame height *vs.* HRR increased without the hood by roughly two times that with the hood, as shown in Fig. 5-11(b). This demonstrates that the hood constrained the flame heights as the HRR increased, whereas without the hood the flames were able to get taller. A linear correlation was still best suited with r^2 values of 0.93–0.97 (without the hood). Nevertheless, the FB flame

heights remained similar whether the hood was present or absent. When comparing the flame heights of the FWs and FB fires with no hood, FW flames were 1.65 to 2 times higher. Pinto *et al*. (2017) also observed the effect of the flow stagnation that is produced by the presence of the ceiling. All simulations were performed without the presence of a hood. In all case the simulations underpredict the flame heights and give flame heigh estimates closer to the measured values with the hood. Nevertheless, the simulations show the trend with increasing HRR.

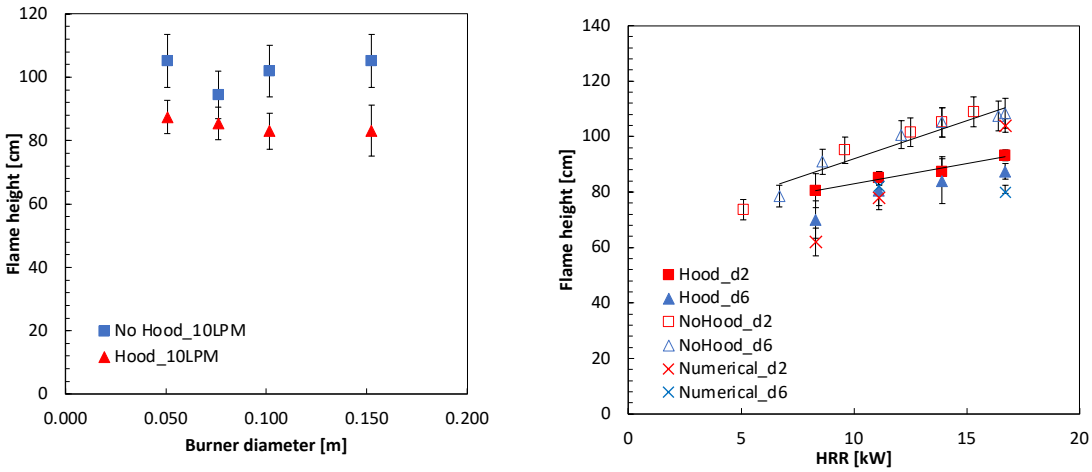

(a) (b)

Figure 5-11: Flame height dependence on the hood configuration of the FWG, burner diameter, and HRR: (a) FW data at 13.9 kW, and (b) FW experiments and numerical results using 2 in (52.5 mm) and 6 in (154.1 mm) burner diameters.

Figure 5-11 shows a significant difference in flame height when the chamber does not have a hood. To investigate whether increasing the wall height of the chamber would also produce larger flame, numerical simulations were used. Although it is recognized that there is a difference between the experimental data and numerical predictions, as shown in Fig. 5-11, it is expected that the simulations should provide a reasonable prediction of the trend when wall height is increased. For the simulations, wall heights of 1.2 m (the wall height

used in the experiments), 2.6 m, and 4.0 m were used. Four corner gaps were used that extended all the way to the top of the walls, and the 3 in (77.9 mm) diameter burner was simulated. The effect of the wall height on flame height was predicted using three different HRRs of 8.3, 11.1, and 16.7 kW, and the results are shown in Fig. 5-12. The lowest HRR had less impact on the flame height, but as the HRR increased so did the impact of the wall height on the resulting flame height. Changing the wall height from 1.2 m to 4.0 m, the FW with HRR of 16.7 kW had a flame height that changed from approximately 0.76 m to 1.08 m. This is approximately a 42% flame height increase. Therefore, to accurately investigate FWs with large HRRs, a taller chamber must be used. It is likely that the flame heights of the smaller HRR FWs were less impacted by the wall height increase because their height did not approach the top of the chamber.

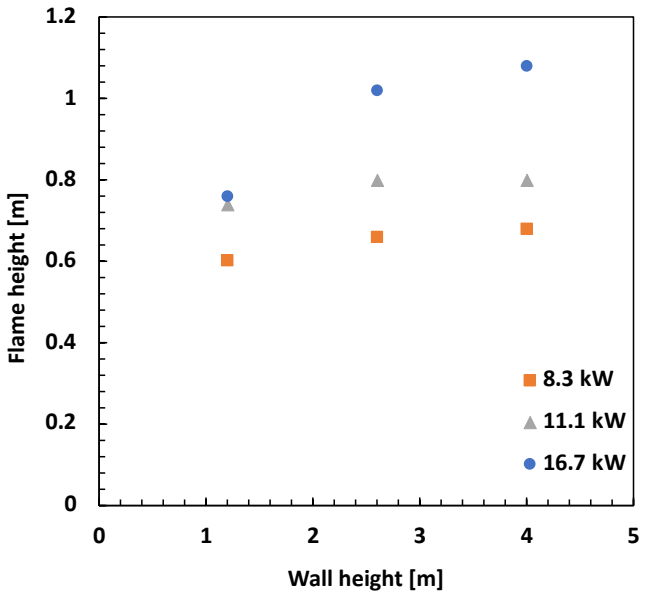

Figure 5-12: Predicted effect of the chamber wall height and HRR on the FW flame height for a 3 in (77.9 mm) diameter burner.

5.2.2. Effect of gap size

The experimental data for the FB and FW cases were plotted using the result of the

dimensional analysis given by Eq. (2-4) (simplified Heskestad's correlation). As shown in Fig. 5-13(a) and (b), the data was found to fit a power law with r^2 values of 0.97 and 0.98 for the FB and FW cases.

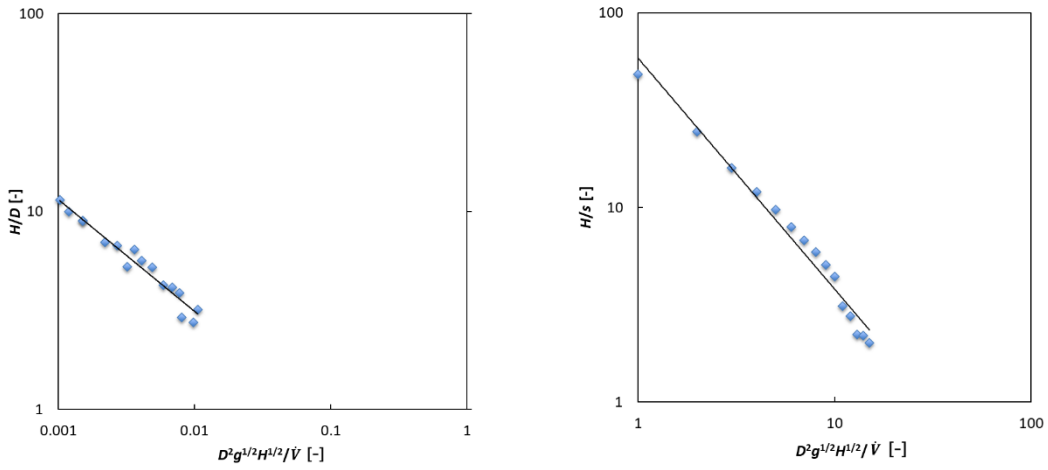

(a) (b)

Figure 5-13: The dimensional analysis given by Eq. (2-4) plotted for (a) free burning and (b) fire whirl experiments.

The FW data exhibits a large dependence on air gap width *s*. A series of experiments were completed using the 3 in (77.9 mm) diameter burner and an HRR of 11.1 kW to determine the impact of gap size on the flame height. The results are shown in Fig. 5-14 and Fig. 5-15. The normalized flame heights were plotted versus S^*, which is the normalized gap size:

$$S^* = s/L_c \tag{5-15}$$

where L_c is the side length of the chamber, and *s* is the gap width.

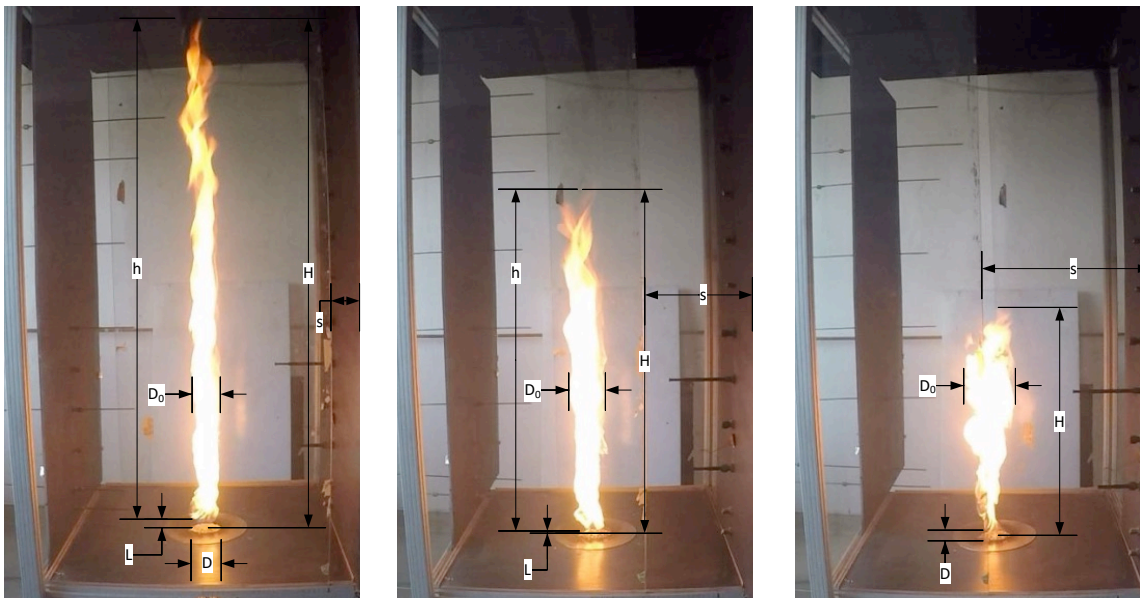

(a) s = 60 mm (b) s = 200 mm (c) s = 320 mm

Figure 5-14: The visible flame height at different gap widths s.

As the gap width increased, the shape of the fire whirl changed from a long thin flame with a semi-constant D_0 to a shorter flame structure with a changing D_0. The larger gap sizes produced larger D_0 at the top of the flame and smaller D_0 closer to the burner, as shown in Fig. 5-14(c). This behaviour is consistent with higher air entrainment and lower inlet velocity associated with a larger gap size resulting in a lower circulation. The data was correlated by a parabolic function with r^2 = 0.99 using the following expression (Fig. 5-15):

$$H^* = -27.56S^{*2} + 6.34S^* + 12.43 \quad (5\text{-}16)$$

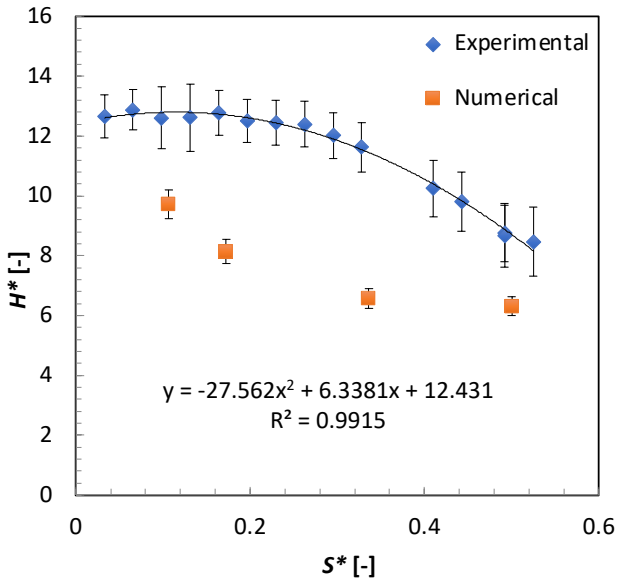

Figure 5-15: Experimental and numerical normalized flame height plotted against the normalized gap size. Error bars indicate RSME.

The vertex of this function yields a maximum for a gap size of approximately 70 ± 5 mm, which agrees with the stability tests shown in the following section. This indicates that more stable FWs have larger flame heights. A stable and strong fire whirl was produced with an S^* of 0.1 to 0.25. To yield a stable FW, the gap size cannot be too small or too large. However, when the normalized gap size is as large as 0.5 (half of the chamber length) a fire whirl was still formed but with half the size in height. After this $S^* = 0.55$, the fire whirl no longer formed and turned into a free burning flame. The simulations results produced shorter flame heights than the experimental data, especially for larger gap sizes. It is likely that more resolution would be required for the intermediate gap sizes to make more accurate predictions due to the increased flow complexity.

Hung *et al*. (2021) stated that FWs can only be generated when the gap width lies within a certain range. The height of their chamber was 1.45 m, and their optimal gap width ratio was 0.09 to 0.29 in the vertical shaft model with one opening. A linear correlation between

flame height and mass fuel burning rate can be determined for different liquid fuels. Gao *et al*. (2019) studied the effect of gap width with a fixed-frame facility (H_c = 9 m) with one opening. They determined that the strongest FW formed when the gap width S^* was 0.15–0.2. They also observed that when the gap width was too small no fire whirl formed and as the gap grew a fire whirl began to form. The fire whirl became stable at an optimal gap width and within that range the flame heights were also the largest. As the gap width grew larger the fire whirl became shorter and unstable.

The next set of experiments examined the influence that the number of air gap openings had on the fire whirl by varying from one to four inlets (Fig. 3-1(b)–(d)). The air gap was set to one of three different configurations: fully open (F), comprising 1 220 mm high × 65 mm wide gaps; partially open (P), comprising 457 mm high × 65 mm wide gaps; and mixed, which used a combination of half and fully open air gaps. Table 5-3 summarizes the eleven combinations of openings which were tested at two HRR of 8.3 and 11.1 kW.

Table 5-3: Combinations of air gaps tested.

Combinations	Number of Openings			
	1	2	3	4
F–Fully Open	FCCC	FCFC	FFFC	FFFF
P–Partially Open	PCCC	PCFC	FPPC	PFPF
C–Closed		PCPC	PPPC	PPPP

As shown in Fig. 5-16, the flame heights did not vary significantly with the number of openings at a single HRR when a stable FW was formed. The one-inlet partially open case

at HRR of 11.1 kW, and both one inlet cases at HRR of 8.3 kW, did not produce stable FWs. This is indicated on the graph both by lower mean flame heights and by larger variations. All other cases produced stable FWs with similar flame heights. The error bars were calculated using the RSME method, which indicated the degree of variation. From these results and visual observations, it was concluded that four-inlet partially open case was the most stable. The experiments were repeated three times as well as completed with and without the hood, which showed similar trends in all cases.

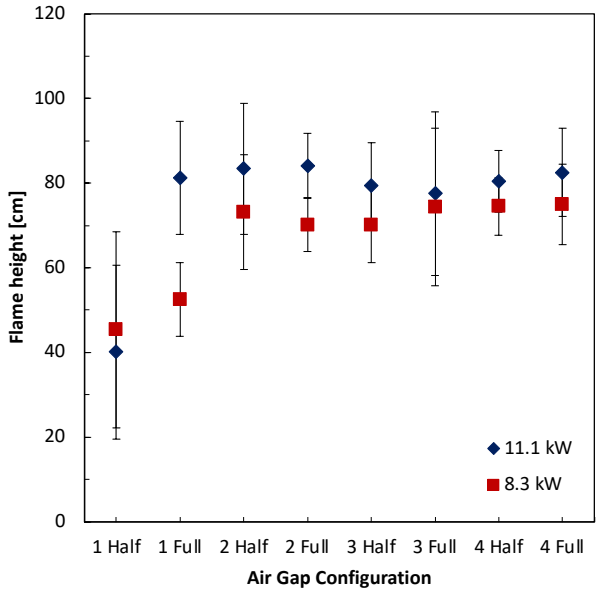

Figure 5-16: Variation of flame height for different inlet configurations with HRRs of 8.3 kW and 11.1 kW using the 3 in (77.9 mm) diameter burner.

The FDS simulations for the number of inlets produced unstable FWs for the one-inlet partially and fully open gap cases for both HRRs. The two-, three-, and four-inlet partially open gap cases produced stable FWs with flame heights between 78 and 82 cm. These results are similar to the experimental data, which corroborates that the flame height is a weak function of the number of inlets except for the one-inlet case.

5.3. Flame Temperature

The centreline averaged temperature profiles of the FWs are parabolic with a maximum between 30 and 50 cm in height. The maximum temperature is close to 1 000 °C and then decreases steadily with height. Many researchers (Emmons and Ying, 1967; Lei, 2015; Wang, 2015) have observed the type of "hump-like" profile that is shown in Fig. 5-17(a). Conversely, the FB profiles decrease as the height increases and have a maximum temperature of approximately 650 °C. The FW flame temperature is much higher than that of the FB flame. This follows the experimental data and analysis of Lei *et al.* (2015), which they explained by the reduced mixing between the hot products and the entrainment of cool air for FWs. Comparing the temperature profiles obtained for different burner diameters, there is no significant difference, especially in the FW cases. The error bars in Fig. 5-17 depict the root-mean-square error (RMSE) and provide a measure of the variability in the data due to flame oscillation and precession.

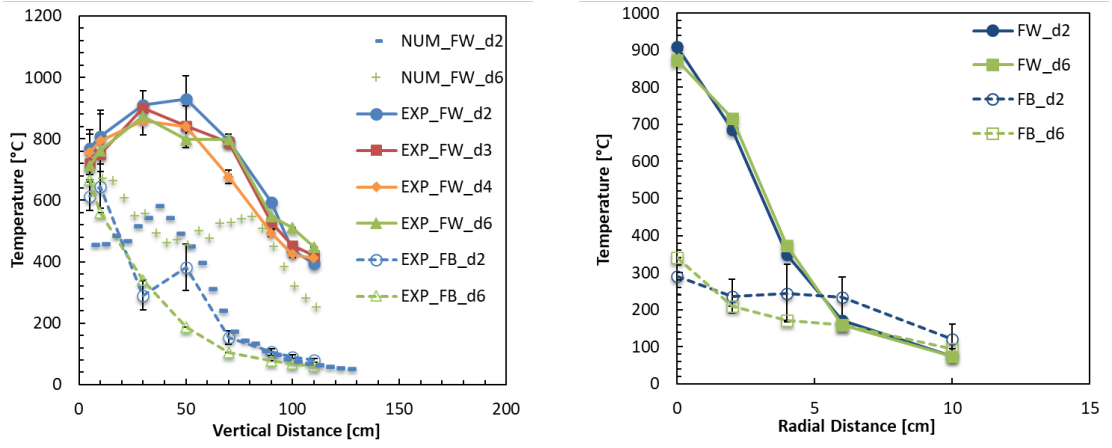

(a) Centreline profile (b) Radial profile at z = 30 cm

Figure 5-17: Temperature profiles of FWs and FB fires with HRR of 11.1 kW and 2 in (52.5 mm) and 6 in (154.1 mm) burner diameters.

The measured centreline averaged temperatures and simulations results for the FWs using the 2 in (52.5 mm) and 6 in (154.1 mm) burner diameters are presented in Fig. 5-17(a) and Fig. 5-18. The simulations underpredicted the flame temperature compared the experimental data. However, the trend and shape are generally similar in that they produce the "hump-like" profile and decrease drastically in the plume region. Although stable fire whirls were formed in the simulations, it was observed that these FWs often moved in and out of the centreline. It is likely that this increased motion around the centreline led to lower mean temperature estimates than observed for the experiments. It is likely that the temperature predictions would be closer to the experimental data if higher mesh resolution and/or more resolved radiation predictions were used.

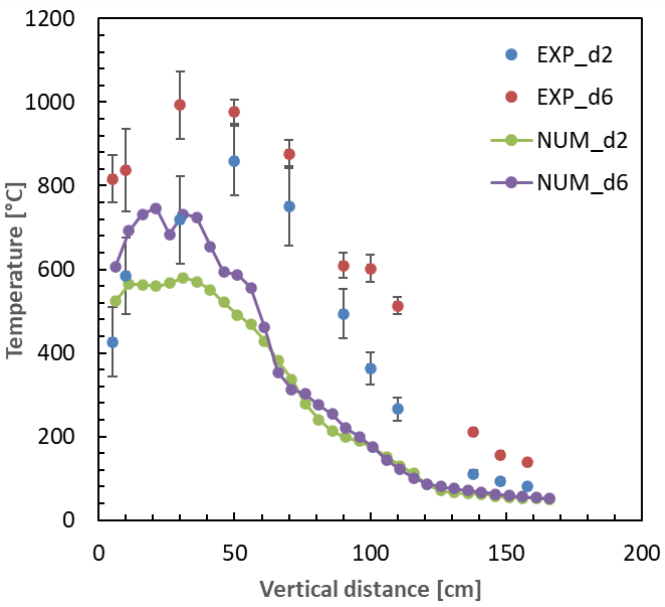

Figure 5-18: Numerical and experimental data for FW centreline temperature profiles with 16.7 kW HRR for 2 in (52.5 mm) and 6 in (154.1 mm) burner diameters.

Lei *et al.* (2015) studied propane FWs in a square-based, fixed-frame apparatus and estimated the entrainment coefficient with HRRs of 25, 50, 100, 150, 200, 250, and

300 kW. The values of ΔT as a function of normalized flame height ($Z = z/H$, where z is the height above the burner outlet) indicate that the end of the continuous flame occurs at $Z = 0.77$, *i.e.,* at 77 % of the average flame height. At this point, $\Delta T \approx 1\,000$ °C (1 273 K). The intermittent region occurs in the range of $0.77 < z/H < 1.22$, and they state that $\Delta T \sim Z^{-1.79}$. In the plume region, $z/H > 1.22$, Lei *et al.* (2015) plotted different HRRs, which resulted in slopes between –1.51 and –0.09. In the present work, the continuous flame region is from 10 to 50 cm for FW and 10 to 30 cm for FB. The intermittent region for FW is 70 to 100 cm and 50 to 70 cm for FB. The plume regions are 110 cm and above for FW and above 70 cm for FB.

Fig. 5-19(a) displayed the slope for the continuous, intermittent and plume region for the FW flame, which are 0.24, –1.42, and –1.85. If the plume region was spilt into the different HRR and plotted with Lei *et al.* (2015) data (Fig. 5-19(b)), the data provides two different slopes. The HRR with 10 to 20 kW and 5 to 10 kW in this work are similar to the HRR of Lei *et al.* (2015) at 200 to 300 kW and 100 kW.

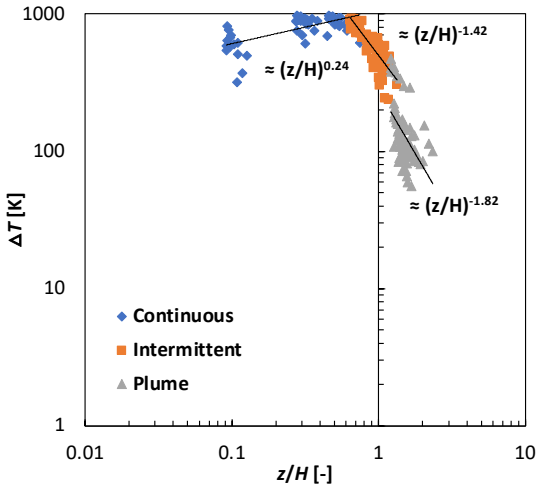

(a) Three distinct flame regions

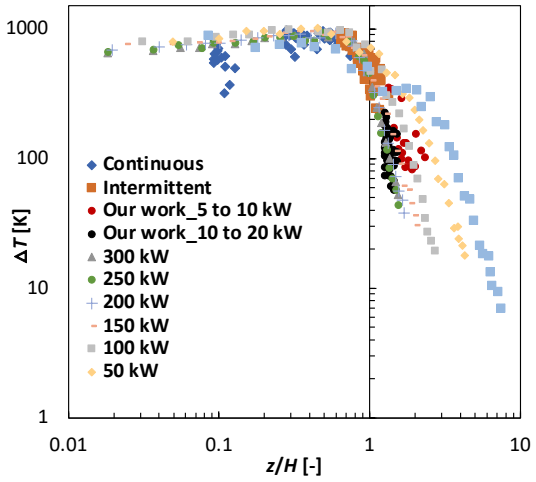

(b) Separated plume region observed by Lei *et al.* (2015) for for different HRRs ranging from 25 kW to 300 kW

Figure 5-19: Centreline temperature profiles for FWs versus the normalized height z/H.

Figure 5-20 shows the comparison of the flame temperature at the centreline between FW and FB fires. Like Grishin (2005), the FW flame is approximately 1.2 times greater than the FB flame in the core (10 cm). Due to the intermittent and plume regions being at different heights, the difference between the flame temperatures increased rapidly. The maximum flame temperature for the FW was approximately 1.3 to 1.6 times greater than the FB flame. The FW maximum flame temperature occurred between 30 to 50 cm, whereas the maximum FB flame temperature occurred between 5 to 10 cm.

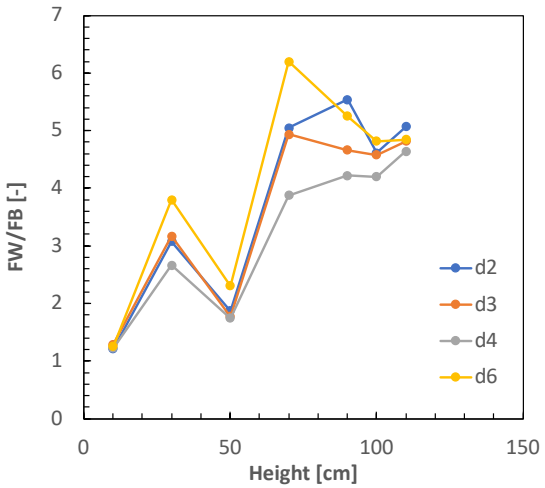

Figure 5-20: Comparison of FW and FB flame temperature at 11.1 kW.

Zukoski *et al*. (1981a, b) determined another method used to estimate the flame height by using the axial centreline temperatures from the experiments. The edge of the visible flame height corresponds to an average centreline temperature of approximately 500–550 °C. His study was for FB flames; however, Fig. 5-21(a) shows an example of this method used on a FW flame. The flame height in this example would be approximately 90 ± 10 cm. Since the thermocouples are spaced by 20 cm, the temperatures that fall within the range can be interpolated, but this is a rough estimate. Fifteen random FW experiments were chosen with different HRR and burner diameters, and the flame heights estimated using image processing and temperature interpolation were compared. This comparison is shown in Fig. 5-21(b). Comparing the two methods reveals general agreement. Thus, there is general agreement between visual observations and flame temperatures, further validating the results. This is a good method to determine if there is general agreement between temperature measurements and visual flame height..

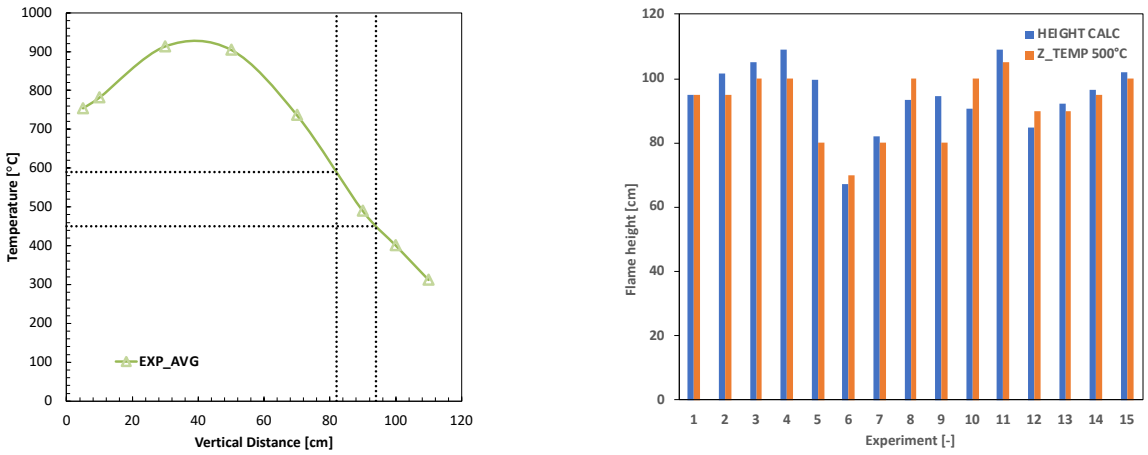

(a) (b)

Figure 5-21: (a) Interpolation of the flame height from axial temperature profile data at the centreline. (b) Comparison of flame heights obtained through temperature profile interpolation and image processing.

5.3.1. Effect of heat release rate

Plotting the temperature according to McCaffrey (1979), the effect of the heat release on the temperature was determined. The plume region is a focus as it provides useful information for fire detection and smoke movement (Drysdale, 1992). Figure 5-22 shows the free burning centreline temperature plotted according to McCaffrey's ($z/Q^{2/5}$) correlation.

$$\Delta T_0 = \left(\frac{\varsigma}{0.9\sqrt{2g}}\right)^2 \left(\frac{z}{\dot{Q}^{2/5}}\right)^{2\eta-1} T_0 \qquad (5\text{-}17)$$

According to McCaffrey, the constants ς and η for the continuous, intermittent, and plume region are 6.8 [$m^{1/2}$ s^{-1}] and ½, 1.9 [m $kW^{-1/5}$ s^{-1}] and 0, and 1.1 [$m^{4/3}$ $kW^{-1/3}$ s^{-1}] and $-1/3$. The range of $z/\dot{Q}^{2/5}$ [m $kW^{-2/5}$] for the continuous region is < 0.08, the intermittent region is 0.08–0.2, and the plume region is > 0.2. Each region is given a slope (η) plume, intermittent, and continuous with η of 0, -1, and $-5/3$ respectively (Drysdale, 1992). The

experimental data for the free burning flames was plotted, $(T_0 - T_\infty)\ vs.\ z/\dot{Q}^{2/5}$, and the three regions are shown in Fig. 5-22. McCaffrey stated the coefficient for the power is 0, -1, and -1.67 for the continuous, intermittent, and plume regions. For the FB data, the coefficients were very similar and equal to 0.03, -1.16, and -1.76 respectively.

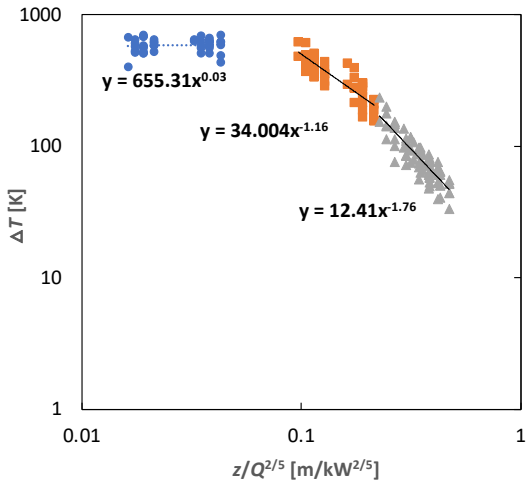

Figure 5-22: Centreline temperature difference plotted according to McCaffrey's correlation for the FB flame.

When the FW flame temperatures were plotted against $z/\dot{Q}^{2/5}$, the coefficient for the continuous, intermittent, and plume regions were 0.26, –1.14, and –2.25, as shown in Fig. 5-23(a). The data were very scattered and did not correlate well. When the flame temperature was plotted against $\dot{Q}^{4/5}$, the regression coefficient went from r^2 of 0.7 to 0.9 with power coefficients of 0.18, –2.08, and –1.97, as shown in Fig. 5-23(b).

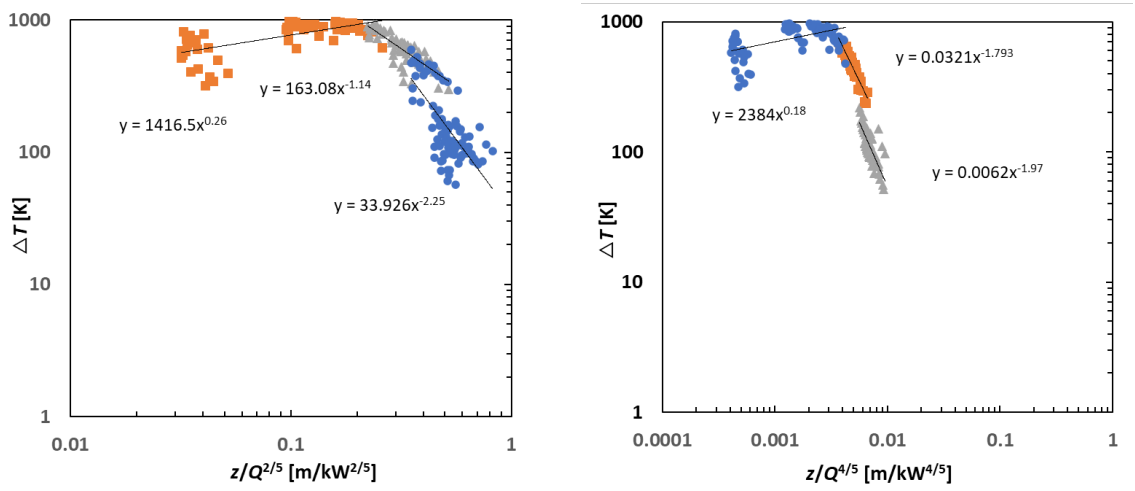

(a) (b)

Figure 5-23: Centreline flame temperature for FWs plotted against (a) $z/\dot{Q}^{2/5}$ and (b) $z/\dot{Q}^{4/5}$.

The temperature distribution as a function of z in the intermittent flame for FB is known to be correlated by $\Delta T \sim z^{-1}$, and the plume region is correlated by $\Delta T \sim z^{-1.7}$ with an r^2 of 0.99. Conversely, as shown in Fig. 5-24, the FW plume temperature gives $\Delta T \sim z^{-3.7}$, which means the temperature cools faster with height above the flame in the FW situations.

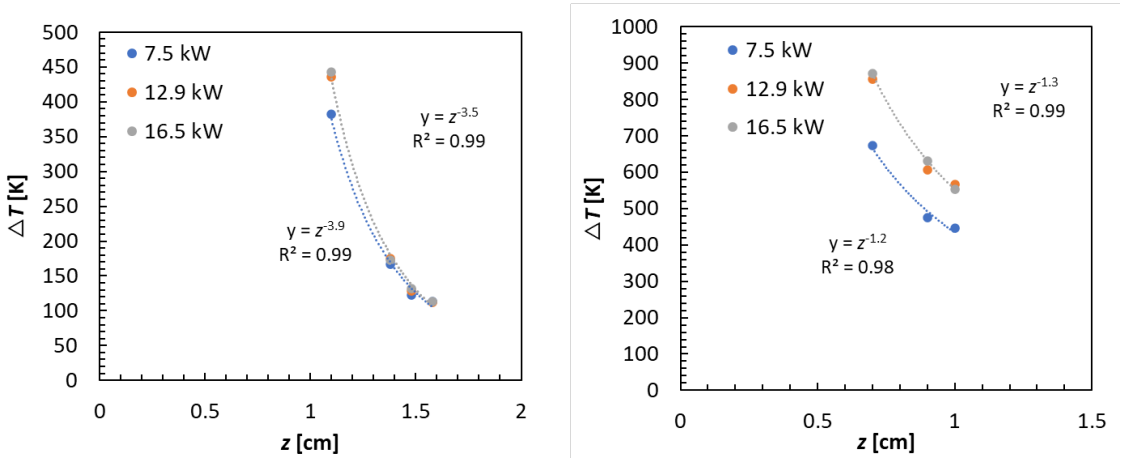

(a) (b)

Figure 5-24: Centreline FW flame temperature plotted against z in (a) the plume region and (b) the intermittent region.

5.3.2. Effect of number of gaps

The temperature fluctuation can be related to the stability, with less fluctuation leading to higher mean flame temperatures and less variability in the temporal temperature data. Figure 5-25 shows temperature over 200 s for the continuous and intermittent regions. The 1- and 2-inlet cases with full gaps have more oscillation in the data than the 3- and 4-inlet data. Only the 1-inlet half gap case exhibited FB-like qualities as the flame temperature is much lower than all the others. However, it is important to note that the 2-inlet half gap case was unstable at times, which can be seen by the oscillation in temperature data (Fig. 5-25(d)). Nevertheless, the average flame temperatures for all cases were consistent, and no strong dependence on gap number was observed.

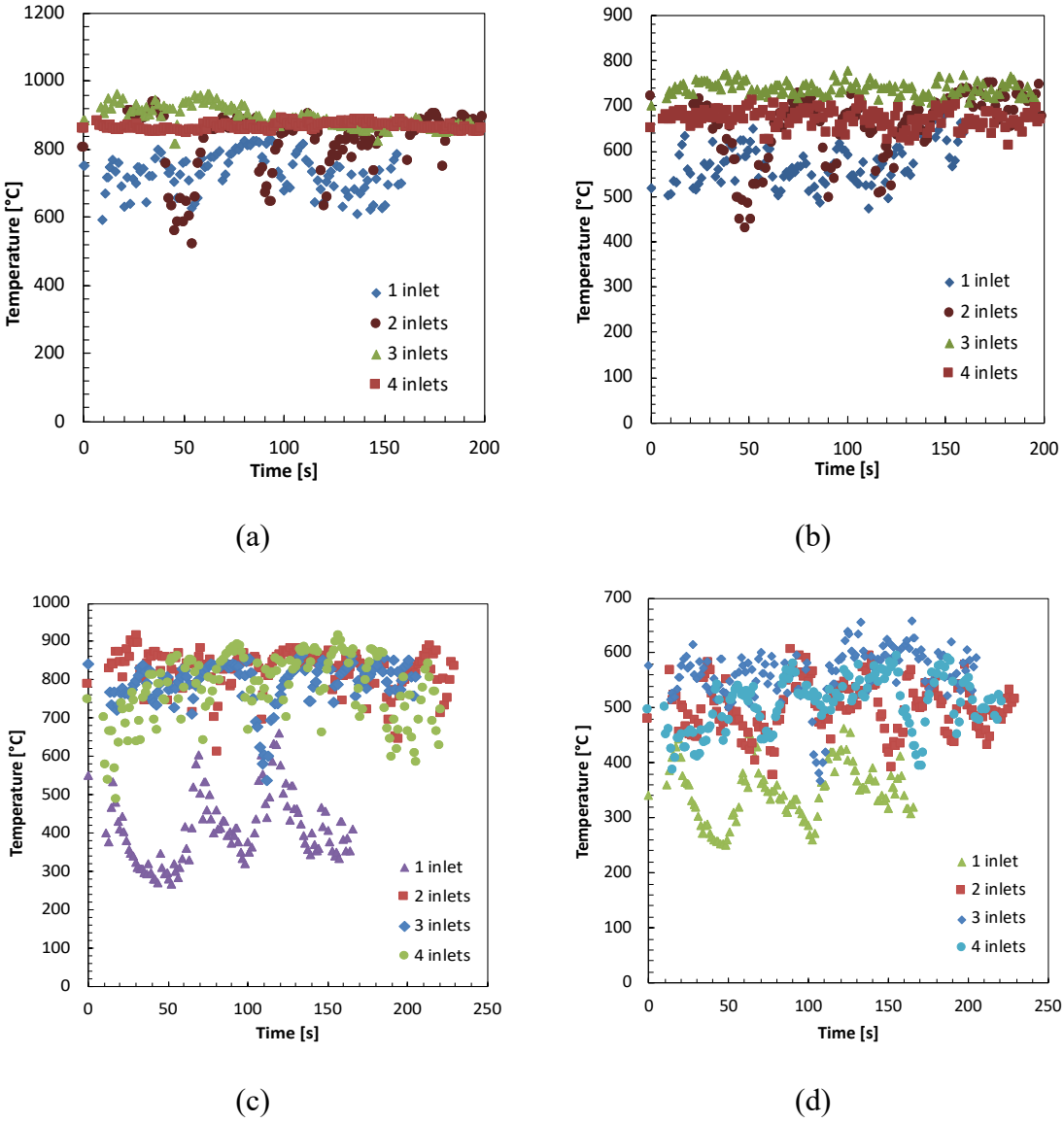

Figure 5-25: Centreline temperature profiles with different number of openings: (a) continuous region for full gap case at 11.1 kW, (b) intermittent region for full gap case at 11.1 kW, (c) continuous region for half gap case at 8.3 kW, and (d) intermittent region for half gap case at 8.3 kW.

Further analysis of the 4-inlet experiments with different gap openings—full, mixed, and half—is shown in Fig. 5-26. There was not a large difference in the centreline temperature profiles as the gap sizes changed with no major fluctuation in data. The intermittent region produced the most oscillations, which was explained by Drysdale (1992) to be caused from the instability at the boundary layer between the fire plume and the surrounding air. The

oscillation in the intermittent region can determine the rate of air entrainment into the flame (Zukoski, 1981). Visually, at the intermittent region, the flame was rising upwards through the plume and burning out, which produced ghost flames.

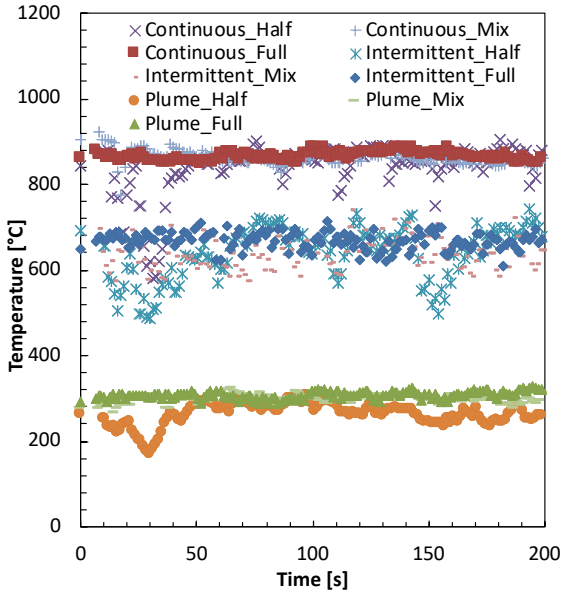

Figure 5-26: Comparison of centreline temperature in the three regions of a FW flame with HRR of 11.1 kW for half, mixed, and full gap cases. Temperatures are plotted at heights of 30 cm (continuous), 70 cm (intermittent), and 110 cm (plume).

Figure 5-27 shows the measured and simulated centreline temperature profiles. Similar to the measured temperature the 2- and 3-inlet cases produce similar temperature. The simulation unpredicted the temperature for these cases, but overpredicted the temperature for the 4-inlet case. The measured peak temperatures in all three cases were very similar.

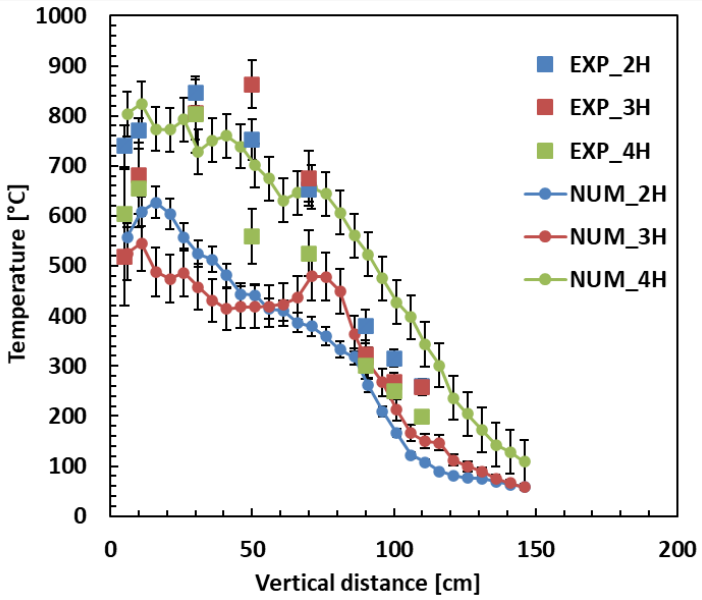

Figure 5-27: Numerical and experimental centreline temperature profiles for 2-, 3-, and 4-inlets with half gap with 11.1 kW HRR for 3 in (76.2 mm) burner diameter.

5.3.3. Effect of chamber configuration

The effect of the chamber's hood is discussed in more detail in this section. As shown in Fig. 5-28, the FB flame temperatures did not differ significantly whether the hood was there or not.

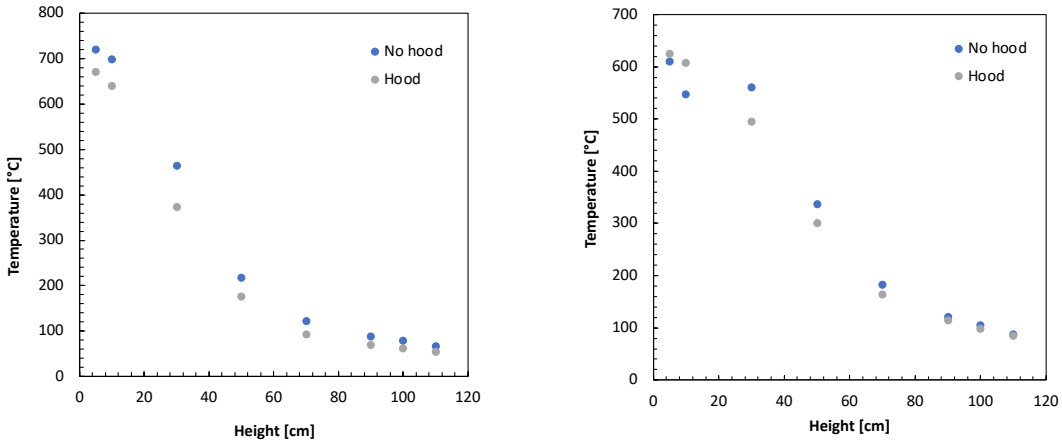

(a) (b)

Figure 5-28: The centreline temperature profile for FB flames without the hood (No hood) and with the hood (Hood): (a) burner diameter of 6 in (152.4 mm) at 8.3 kW HRR, and (b) burner diameter of 3 in (77.9 mm) at 13.9 kW.

The FW centreline flame temperatures differed in the continuous and plume regions. In the continuous region, the flames produced with the hood were hotter flames than those produced without the hood. At higher HRRs, the difference was not as significant as at the lower HRRs. In the intermittent region, the flame temperatures were similar, but the flames produced with the hood were less hot. In the plume region, the difference between to two flame temperatures grew further apart, with the flames produced with no hood being greater than those produced with a hood. The cause of these differences is that, in the continuous region, the mixing is more pronounced when the hood is present, which results in a higher temperature, as shown in Fig. 5-29. The difference in plume region is due to the flame height being larger when the FWs are formed without a hood, which was discussed in section 3.2.2.

All simulations were performed without the presence of a hood. The measured temperatures with no hood agreed more with the predicted simulations. At the flame core,

the temperature is much lower and as the height increases the temperature rapidly increases to a peak. Although the simulation unpredicted the peak the trend once again is similar to the experimental data. By increasing the wall height, the simulations predict that the flame temperature also increases. The increase in the wall height generally leads to a more stable FW, which means that the temperature probe locations are exposed to the flame over more of the time, thereby leading to a higher mean temperature. As the wall height is increases, the flame also becomes taller and has a smaller diameter.

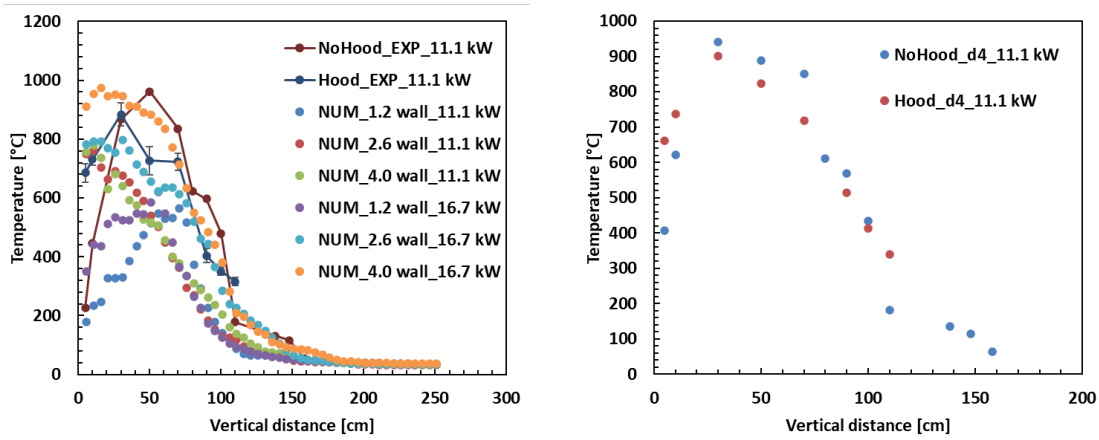

(a) (b)

Figure 5-29: Comparison of FW centreline flame temperature data (a) measured (EXP) and predicted (NUM) using a burner diameter of 3 in (77.9 mm) at 11.1 kW, and (b) measured data using a burner diameter of 4 in (102.3 mm) at 11.1 kW.

5.4. General Discussion

This study focused on developing a deeper understanding of the fire dynamics for different apparatus configurations and operating conditions. The experiments in this chapter were performed using propane as the fuel to study the effect of inlet gap size, number of gaps, and heat release rate on fire whirl dynamics and stability in a fixed-frame FWG.

The factors that did not significantly affect the flame height and temperature were the burner diameter and the change in number of inlets as long as a stable FW was formed. The factors that did affect the flame height were HRR, the presence or absence of hood above the chamber, the gap size, and the wall height of the chamber. The flame heights increased linearly with the HRR: $H = A \cdot (HRR) + B$. When the hood was present, the flame heights were noticeably (10–30 %) shorter. The gap width affected the flame height and stability significantly. It was determined that the tallest and most stable FWs were produced using a gap width of approximately 70 ± 5 mm. Changing the gap height from the partially open to the fully open gap significantly affected the 1-inlet case. However, for all other cases there was only a small change in results. It was observed that if the bottom of the inlet was blocked off, no FW would form. Thus, if a half gap configuration is chosen, the top must be covered while keeping the bottom open.

Most simulations produced a stable FW after 15 s and predicted similar flame heights and trends to the experimental data. This helps to build confidence in the model. However, it is important to recognize that flame temperatures were usually underpredicted, likely due to greater movement of the flame as well as limitations on the heat transfer and burning rate models. The model was used to predict the effect of the chamber wall height on the flame height and centreline flame temperature. The results showed a significant increase in flame height and centreline temperature for increasing wall heights. At higher HRR, the flame height grew by more than 40% for a wall height change from 1.2 m to 4.0 m. For smaller HRR, little impact of the wall height was observed.

The trends found using a propane fire source will help differentiate between inherent dynamics caused by the fire whirl and dynamic effects related to the shrinking solid structure when analyzing crib fires in future studies.

Chapter 6: Dynamics of Wood Crib Fire Whirls

Previous researchers have used wooden cribs to study the growth and propagation of FB fires because crib fires are relatively inexpensive and convenient. The earliest systematic study of crib fires was by Gross (1962), who studied non-propagating crib fires using Douglas fir with 9.2 % moisture content. Block (1970) also studied non-propagating crib fires using mainly ponderosa pine, and some experiments with birch, Idaho pine, sugar pine, maple, oak, and redwood. Gross (1962) proposed two regimes: the loosely packed regime in which the burning rate is independent of the height and porosity, and the densely packed regime in which the burning rate is a function of height and of porosity. Many other researchers, including this study, examined propagating crib fires.

Thomas (1960) has shown that fire spread within wooden cribs follows the same mechanism as fire spread in cities and forests in the absence of high winds. In this work, the dynamics of square-based, wood crib fires were investigated in a small-scale, square-base, fixed-frame apparatus. For fire whirl (FW) experiments air was admitted through gaps at the four corners of the apparatus, whereas for the free burning (FB) cribs the front and rear walls of the enclosure were removed. For the experiments presented in this study, the air gap was set to 450 mm high × 65 mm wide, which, as noted in Section 5, gave stable FWs. Each crib was built by gluing n square cross-section sticks per layer of thickness b = 6.35, 12.7, and 19.05 mm and lengths l = 76.2, 152.4, and 228.6 mm with equal spacing s between each stick, shown in Fig. 6-1. All cribs had an aspect ratio (stick length/thickness) of 12. The variation in n resulted in cribs with different porosities ε. Each crib had a total number of layers N = 6, giving heights h = 38.1, 76.2, and 114.3 mm. The geometrical

details of the cribs are given in Table 6.1. The formulae for calculating the total cross-sectional area of the vertical shafts, *i.e.,* the vent area A_v, total exposed initial surface area of the fuel A_s, and the total area of the openings on one side of a crib A_{so} are given in Appendix A.

Each crib was placed on a platform flush with the base of the FWG and had a small central ignitor cup, equivalent to 10 % of the crib base area. Ethanol and a wick were placed in the central ignitor cup and used to initiate each propagating fire. Forty-three FB crib fires and fifty-three FW crib experiments were conducted. All tests were propagating crib fires ignited at the centre and burned from the lower layer to the upper layer.

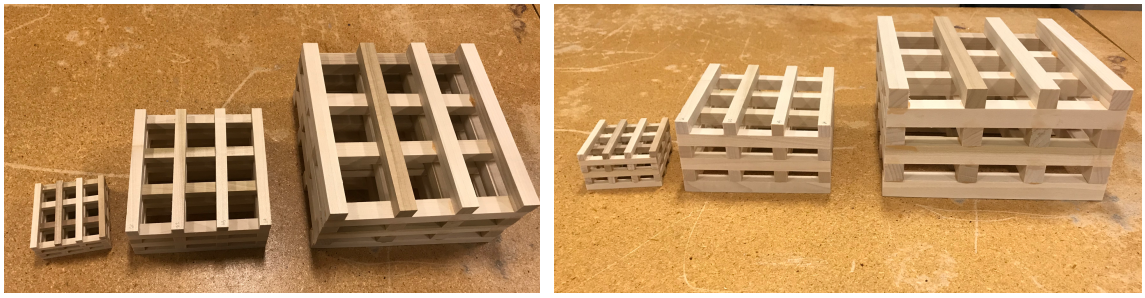

(a) (b)

Figure 6-1: Picture of the experimental wooden cribs built with four sticks per layer: (a) top view, and (b) side view.

Table 6-1: Summary of crib configurations used in the FW and FB experiments.

n / [-]	l / [mm]	s / [mm]	A_v / [m^2]	A_{so} / [m^2]	A_s / [m^2]	ε / [-]
3	76.4	28.6	0.0033	0.0029	0.033	0.75
4	76.4	16.9	0.0026	0.0025	0.042	0.67
5	76.4	11.1	0.0020	0.0022	0.050	0.58
6	76.4	7.6	0.0015	0.0019	0.058	0.50
7	76.4	5.3	0.0010	0.0016	0.065	0.42
3	152.4	57.2	0.0131	0.0057	0.12	0.75
4	152.4	33.9	0.0103	0.0051	0.16	0.67
5	152.4	22.2	0.0079	0.0044	0.19	0.58
6	152.4	15.2	0.0058	0.0038	0.22	0.50
7	152.4	10.6	0.0040	0.0032	0.25	0.42
4	228.6	0.005	0.0232	0.0076	0.36	0.67
5	228.6	0.003	0.0178	0.0067	0.43	0.58
6	228.6	0.002	0.0131	0.0057	0.50	0.50

6.1. Free Burning Cribs

The flame heights, burning rates, flame spread rates, and centreline temperature profiles were measured for FB propagating crib fires. The experimental data were analyzed and discussed using dimensional analysis and non-dimensional parameters to find suitable correlations. This follows the work of Thomas (1960), Smith and Thomas (1968), Fons *et*

al. (1963), O'Dogherty and Young (1964), Pegg (1980), and McAllister (2015). The results from this study were compared with the experiments completed by these researchers.

6.1.1. Burning rates

The burning rate of wood cribs is controlled by the number of sticks present within the crib (loosely or densely packed), the structure of crib, the exposed surface area, the ignition method and position, the type of wood used (including the moisture content), and the air supply from the room (Xu *et al.*, 2008). The progression of a 6 in FB crib fire with $n = 5$ is shown in Fig. 6-2. For a propagating crib fire ignited at the centre of the base, the fire spreads vertically and radially from the point of ignition. The phases relative to the burning rate are as follows: (a) shows the flame appearing from the surface of the crib above the point of ignition; (c) is the point at which the radial fire spread has reached the outer edges of the crib; (d) is where the maximum burning rate occurs during the quasi-steady burning period; (e) shows a point where the height of the flame is decreasing as the burning rate decreases; and (f) shows the decay of the fire as the crib structure begins to collapse prior to burnout of the embers.

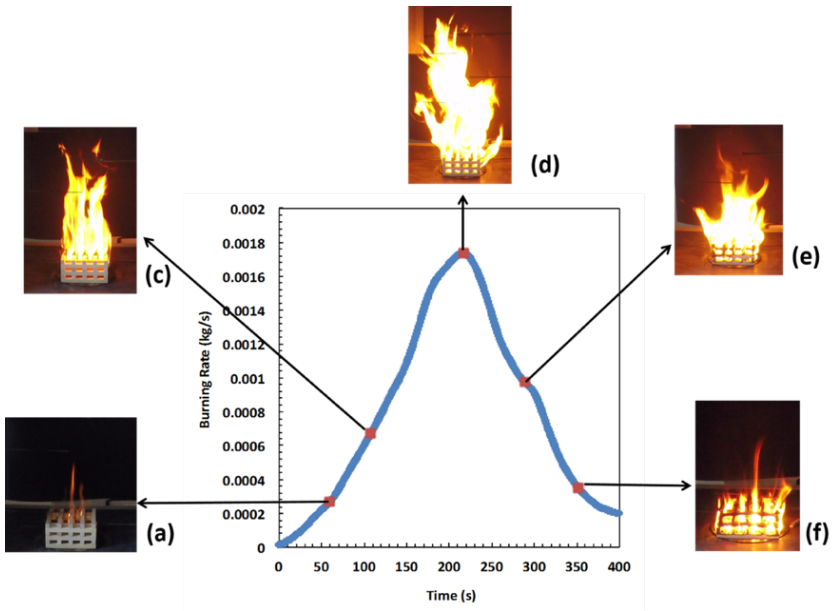

Figure 6-2: Progression of a FB 6 in crib fire with n = 5 showing the relationship between the burning rate of the crib and the visual appearance of the fire.

The burning rates for 3, 6, and 9 in cribs were plotted against the number of sticks per layer, as shown in Fig. 6-3. Table 6-2 provides parameters for the fitted correlations shown in Fig. 6-3. The correlation is of the form $\dot{m} = an^2 + bn + c$.

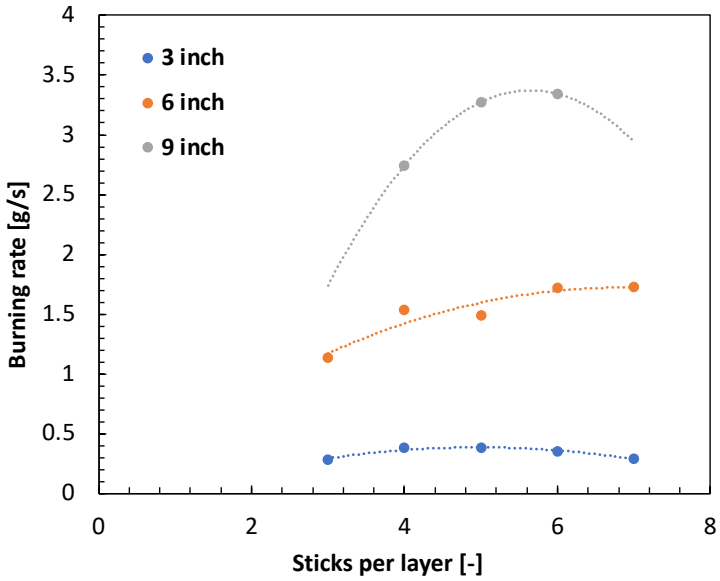

Figure 6-3: Burning rate of 3, 6, and 9 in FB crib plotted against the number of sticks per layer.

Table 6-2: Parameters for the burning rate correlations shown on Fig. 6-3.

	3-inch	**6-inch**	**9-inch**
a	-0.0238	-0.0371	-0.233
b	0.237	0.510	2.63
c	-0.202	-0.0154	-4.05
r^2	0.94	0.89	-

Crib burning rates are often correlated against the characteristic areas of the crib: A_s, A_v, or A_{so}. Burning rate data for replicate tests of the FB crib fires was plotted according to the correlation of Smith and Thomas (1970) and increased linearly with high correlation coefficients (r^2 = 0.96 and 0.99). The plot is shown in Fig. 6-4(a) on logarithmic scales, which correlates the data according to the following equation:

$$\frac{\dot{m}}{A_v\sqrt{h}} = r\left(\frac{A_s}{A_v}\right)^x \tag{6-1}$$

The correlation produced has three distinct lines, one for each crib size. If all the FB tests were plotted as a single set, a lower correlation coefficient of 0.82 is obtained (Fig. 6-4(b)).

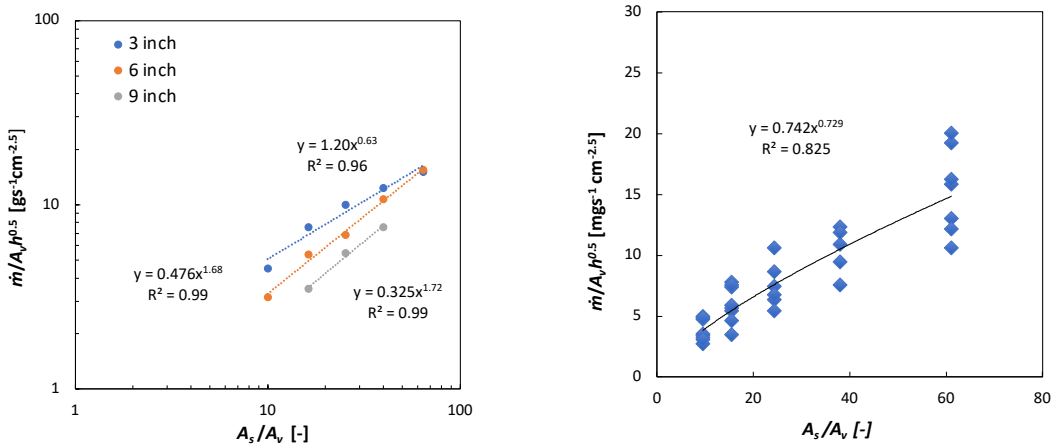

(a) (b)

Figure 6-4: The FB crib burning rate data plotted according to the correlation of Smith and Thomas (1970).

Use of the grouping $\frac{\dot{m}}{A_v\sqrt{h}}$ has a physical significance since upward velocities within the crib are determined by buoyancy and inertia; thus, the volumetric flow rate moving vertically up the vent openings is proportional to $A_v\sqrt{h}$. In an attempt to collapse the data as a single line, $\frac{\dot{m}}{A_v\sqrt{h}}$ was multiplied by b and plotted against $\left(\frac{A_s}{A_v}\right)$, as shown in Fig 6-5(a). Thus, the following correlation is obtained:

$$b\frac{\dot{m}}{A_v\sqrt{h}} = r\left(\frac{A_s}{A_v}\right)^x \tag{6-2}$$

Plotting the data according to Eq. (6-2) brought the 6 in and 9 in crib data on the same line, but the 3 in cribs still did not align, as shown in Fig. 6-5(a). The 3 in cribs were the most densely-packed, and those with n = 6 and 7 produced a significant amount of smoke at the beginning of the fire growth. This is to be expected as the loosely- and densely-packed cribs follow different burning rate regimes (McAllister, 2015).

Several other researchers have studied propagating crib fires. O'Dogherty & Young (1964) burned white pine with 12% moisture content. Pegg (1980) burned ramin (*gonystylus warbariganus*), a Malayan hardwood. Smith and Thomas (1970) analyzed Webster's unpublished data but did not state the moisture content.

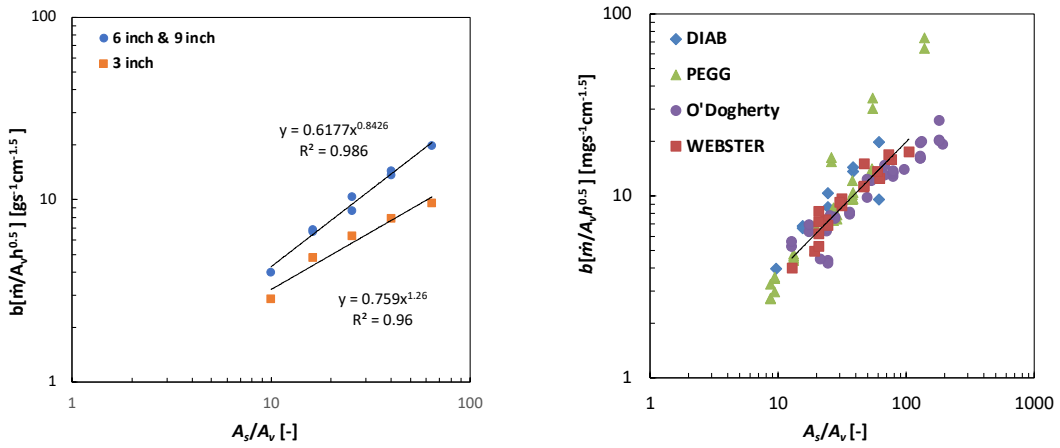

(a) (b)

Figure 6-5: The burning rate data plotted against different areas.

When the smaller cribs ($l \leq 3$ in) were removed, and the data were plotted against the other propagating crib burning rates from literature according to Eq. (6-2), all the data converged, and the data was correlated as shown in Fig. 6-5(b). The following parameters in Eq. (6-2) were obtained through regression:

Reference	k	a	r^2
O'Dogherty &Young (1964)	0.963	0.60	0.90
Pegg (1980)	0.179	1.18	0.93
Webster (unpublished data)	0.597	0.77	0.89
This work	**0.62**	**0.843**	**0.99**

Crib burning rate data has been shown by Yamashika and Kurimoto (1975) to be correlated with the total initial exposed surface area A_s. Figure 6-6 confirms that the burning rate has the strongest dependency on A_s, where all the available burning rate data for propagating crib fires was plotted.

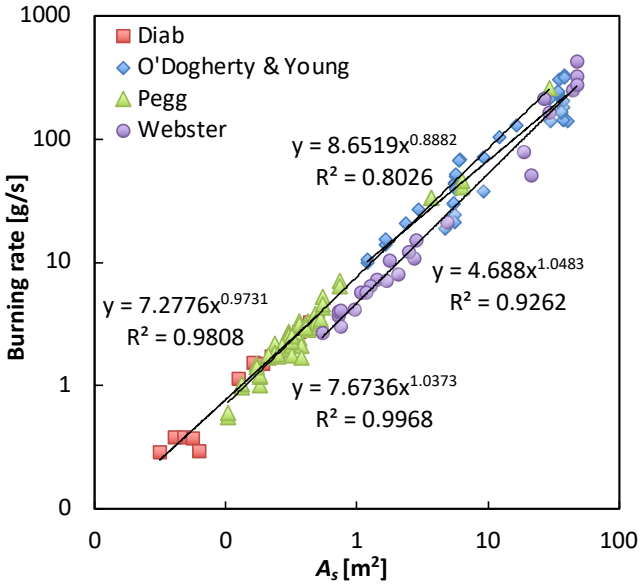

Figure 6-6: Correlation of FB propagating crib burning rates.

6.1.2. Flame heights

The flame height is often correlated against the HRR and the HRR is a function of the burning rate. Furthermore, with crib fires a fraction of the energy from combustion is

utilized to heat up the fuel elements and bring about gasification of the solid fuel. The fraction of energy required for this depends upon the crib geometry, wood species, and moisture content. In this case, the actual HRR is calculated from the following expression:

$$(HRR)_{actual} = \dot{m}\eta\Delta H_c \tag{6-3}$$

where ΔH_c is the heat of combustion, and η is a measure of the 'efficiency' or fraction of the HRR that contributes to the flame. Heskestad (2016) measured the "combustion efficiency", *i.e.,* the ratio of the actual HRR to the theoretical HRR for a stack of wood pallets and obtained a value of approximately 0.63. Wood pallets have some similarity to cribs in that they are constructed and stacked to give a fixed opening (porosity). The combustion efficiency depends on the crib structure because this determines the rate of air flow into the crib. Zhang *et al.* (2015) found η to equal 0.8, whereas Wang *et al.* (2001) stated the combustion efficient to be 0.7 for 10 % moisture content. Both data were reported to be accurate within ± 15 %.

Dalhousie Mineral and Resources Lab measured the higher heating value (HHV) for the yellow popular used in this study and then it was corrected to calculate the lower heating value (LHV) based on literature values for the ultimate analysis, which corrects the H-content and the moisture content and resulted in 17.76 MJ kg^{-1}. Using this value, an estimated "theoretical HRR" can be calculated by multiplying the LHV by the burning rate. Using this HRR value, the Heskestad $\dot{Q}^*$ correlation can be plotted with the normalized flame height (*H*/*D)*. This correlation produced significant scatter in the data and did not correlate as well as it did for the gaseous FB flame. Interestingly, the $\dot{Q}^*$ correlation

produces a power of approximately 2/5, which was the predicted value of Heskestad for free burning liquid and gas fires (Fig. 6-7).

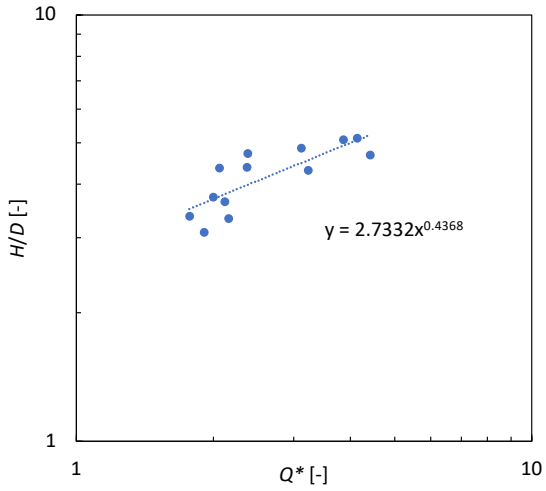

Figure 6-7: Flame height correlated using $\dot{Q}*$ for FB cribs.

The flame height data was correlated with a parameter that affects the air flow rate into the crib. The ratio of l/n controls air flow rate into the crib structure and the quadratic relationship arises because of the dependence of the pressure drop being a quadratic function of the air velocity. Thus, a correlation of the form of $H = a(l/n)^2 + b(l/n) + c$ was used, as shown in Fig. 6-8 and Table 6-3.

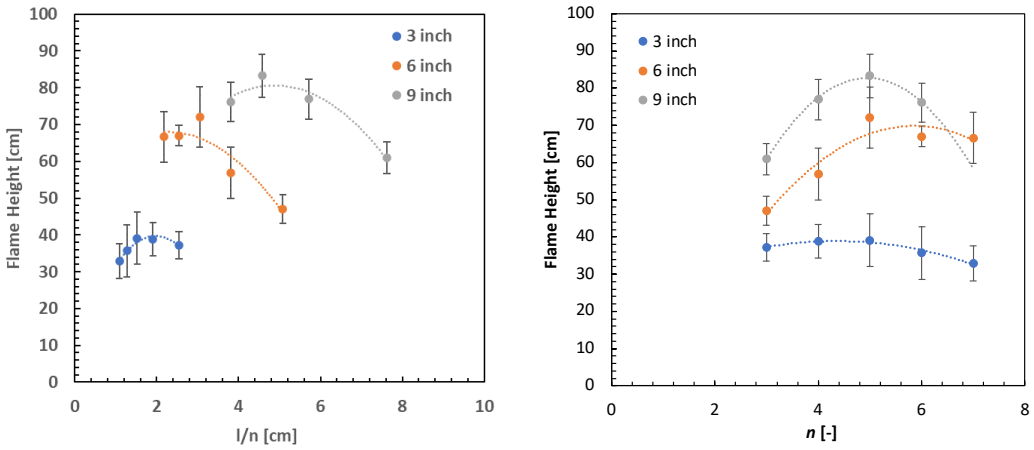

(a) (b)

Figure 6-8: The flame height for FB cribs *vs. l/n* and *n*.

Table 6-3: Correlations for flame height for FB cribs as a function of *l/n*.

	3-inch	**6-inch**	**9-inch**
a	–8.39	–2.79	–2.69
b	33.0	12.7	26.3
c	7.29	53.5	16.3
r^2	0.92	0.86	0.95

Interestingly, when plotting the flame height against the number of sticks per layer, it resulted in a better correlation coefficient, as shown in Table 6-4.

Table 6-4: Correlations for flame height for FB cribs as a function of the number of sticks per layer.

	3-inch	**6-inch**	**9-inch**
a	–0.897	–2.91	–5.8
b	7.81	34.1	57.4
c	21.9	–29.8	–59.3
r^2	**0.96**	**0.907**	**0.997**

The flame heights increased with the number of sticks until it reached a peak, which for all cases was approximately 5 sticks per layer. Both flame heights for 6 and 9 in cribs have a larger dependence on the number of sticks per layer than the 3 in crib. Calculating the maximum flame height from each set—38.9, 70.1, and 82.7 cm—as the length of crib grew so did the flame height. If the flame height was instead calculated from the top of the crib, h_f as shown in Fig. 6-9, the maximum flame heights were reduced to 35.1, 62.4, and 71.2 cm.

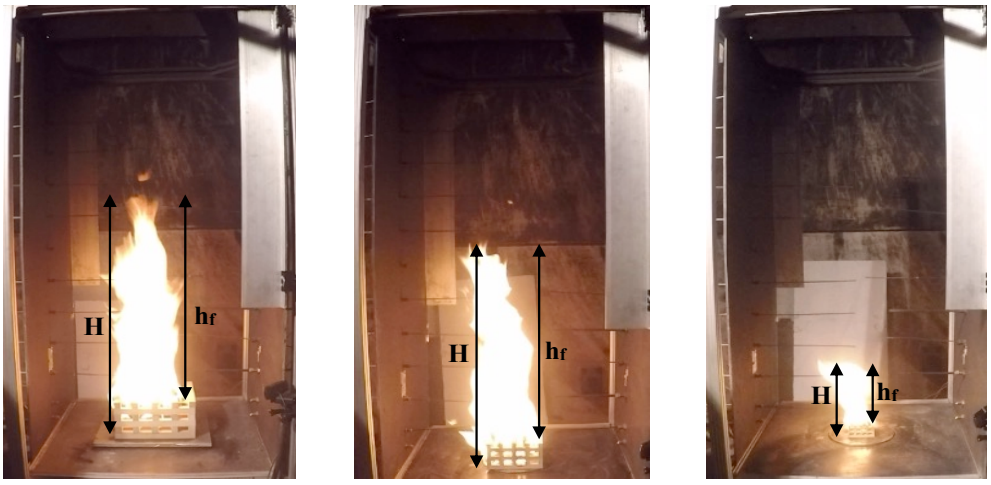

9-inch 6-inch 3-inch

Figure 6-9: The difference between H and h_f for the three crib sizes.

Plotting the average flame height h_f against crib length l, a power correlation is obtained with $r^2 \geq 0.90$, as shown in Fig. 6-10. Figure 6-10 shows that the flame height has a strong dependence on the crib length l, whereas the FB gaseous flame was not dependent on the burner size.

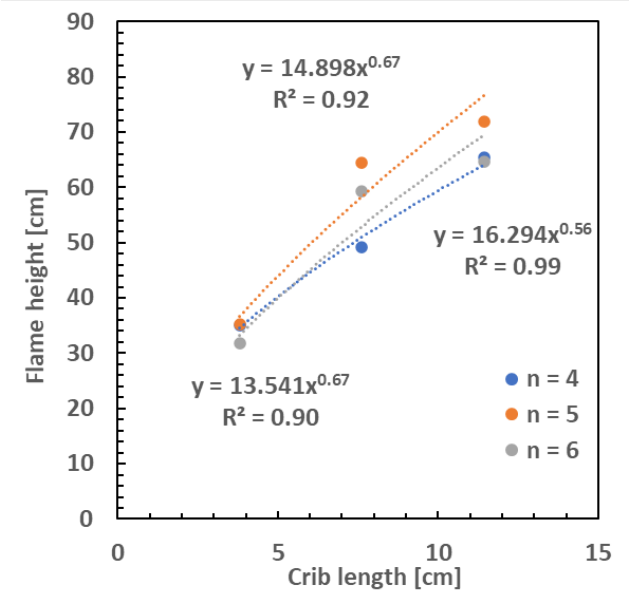

Figure 6-10: Average flame height h_f plotted against crib side length l.

Another method to analyze the dimensional flame height of FB cribs was proposed by Thomas (1962) and discussed in Chapter 2 (Eq. (2-35)). Thomas (1962) used data on Douglas fir obtained by Gross (1962) at the National Bureau of Standards, spruce obtained at the Joint Fire Research Organization (JFRO), and data from Fons *et al.* (1963) for white fir obtained at the US Forest Service (USFS). Gross used cribs that were cubical, whereas Thomas and Fons used shallow-height cribs, and measured the flame height from the base of the crib. Furthermore, Gross placed his cribs above a base plate that allowed air to enter from the bottom of the cribs through the vertical shafts, whereas the JFRO and USFS

experiments placed the cribs on a solid surface, thus only admitting air through the side openings.

The flame height correlations are shown in Fig. 6-11 for the data sets of Thomas (1962) and Fons *et al.* (1963), which produced a better correlation coefficient (r^2 = 0.95 and 0.91) than the FB data set from this work (r^2 = 0.79). However, this difference could be due to having a smaller range of data, whereas Thomas did experiments with a larger range of H/D. This dimensional correlation can be a great predictive tool for FB solid fuel flame heights if the burning rate and the length/diameter are known.

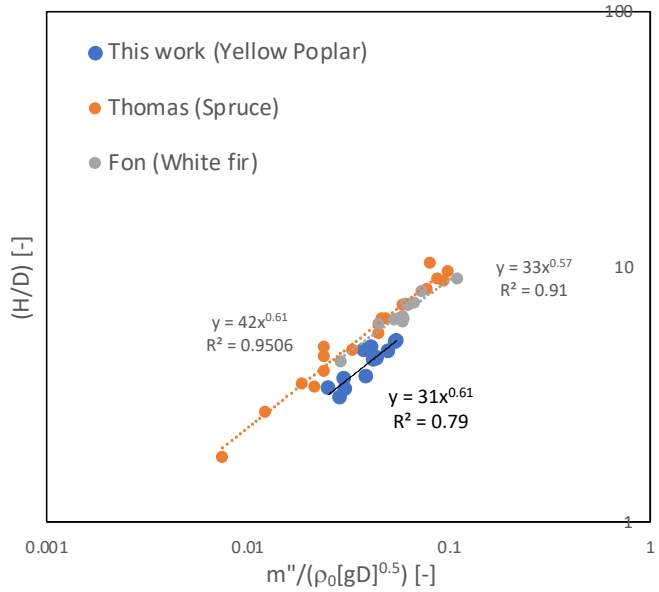

Figure 6-11: Correlation for flame heights of FB cribs.

Comparing the nondimensional flame height correlation of Heskestad with the correlation of Thomas (Eq. (2-35)) shows that the Thomas correlation is a better fit for solid fuel, which may be why Heskestad only proposed using the $\dot{Q}^*$ correlation for liquid and gaseous FB flames.

6.1.3. Flame spread

Fire spread is the process where an unburned fuel surface is heated up by hot combustion products, eventually igniting it. As the fire spreads, propagation of the flame causes the burning surface area to increase. Typical flame-front position issuing from the top surface of the crib from the videos for the FB propagating crib fires is shown in Fig. 6-12 at various times. The fire spreads from the central ignition source to the outside of the crib in a stepwise manner as it transitions from one vertical shaft to the next.

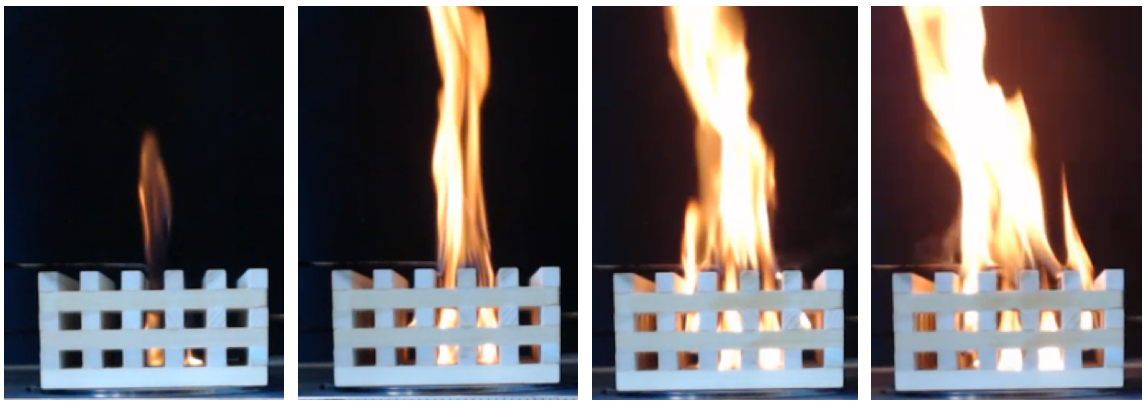

20 s 87 s 163 s 198 s

Figure 6-12: Images showing progression of fire spread through a FB 6 in crib (n = 6).

The 3 in cribs produced very similar spread rate results for n = 4 and 5 and n = 6 and 7. This is to be expected because the crib is small, and therefore changing the number of sticks results in only a small change in the spacing area. Conversely, for the 6 in cribs the spread rates vary greatly from n = 3 to n = 7.

Figure 6-13 shows the fire spread rate data u_s plotted against l/n for the FB crib experiments. Figure 6-14 shows flame spread in the three crib sizes for n = 4.

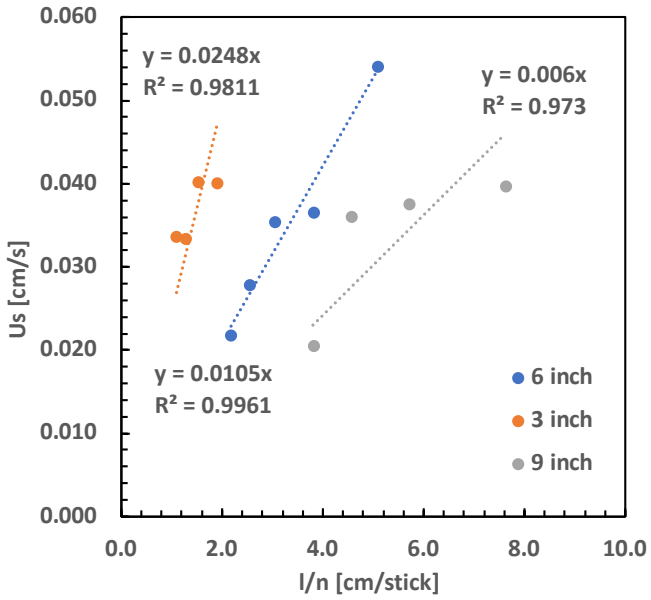

Figure 6-13: Spread rate plots for free burning cribs.

Delichatsios (1976), in his study of fire growth in oven-dried sugar pine wood cribs, found that $u_s = 0.045(l/n)$ when the data was extrapolated to the origin. The data collected for FB cribs in this study showed the following relationships:

3-inch $u_s = 0.025(l/n)$

6-inch $u_s = 0.0105(l/n)$

9-inch $u_s = 0.006(l/n)$

The most likely reason for the lower fire spread rates is that the cribs used in this study had approximately an 8 % moisture content whereas those of Delichatsios (1976) were oven-dried. A secondary reason for the differences could be due to the difference in the thermophysical properties of the different wood types.

Comparing the slopes of the spread rate data for the three cribs, the ratio for 3 to 6 in cribs is 2.36 and ratio for 6 to 9 in cribs is 1.75. These two ratios divided equals 1.3 and dividing the ratio of length 6/3 by 9/6 results in the same value of 1.3. Hence, the spread rate is inversely proportional to the length scale.

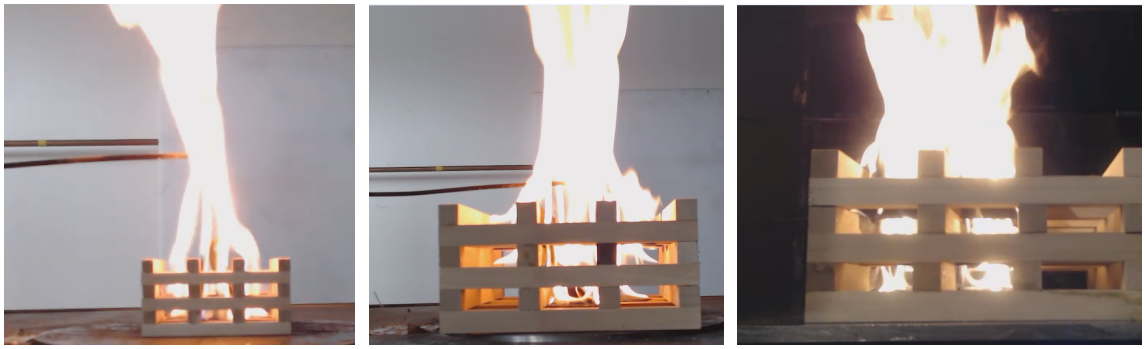

Figure 6-14: Flame spread within the three crib sizes with $n = 4$: 3 in crib (left), 6 in crib (middle), and 9 in crib (right).

6.1.4. Flame temperature

The raw centreline temperature data for the 6 in crib with $n = 5$ and 7 are shown in Figs. 6-15(a) and (b) for the FB crib fires. The flame reached the height of the lowest thermocouple (T2) at 45 s and 100 s for $n = 5$ and $n = 7$, respectively. At 80 s and 200 s the flame began to fluctuate around T3 (30 cm) for $n = 5$ and 7. The flame had fully spread at 100 s with a flame height of approximately 30 cm for $n = 5$, whereas for $n = 7$, the flame had fully spread at 420 s with an approximate flame height of 50 cm. For the $n = 5$ case, the flame height fluctuated between 30 and 60 cm (T3–T4) with no consistent maximum flame height. This can be seen as there are more than one peak on the graph. For the FB crib fire with $n = 7$, the flame height fluctuated between 50 and 70 cm (T4–T5) with many peaks. The significant fluctuations of the temperature data are also due to ghost flames associated with the FB crib fires.

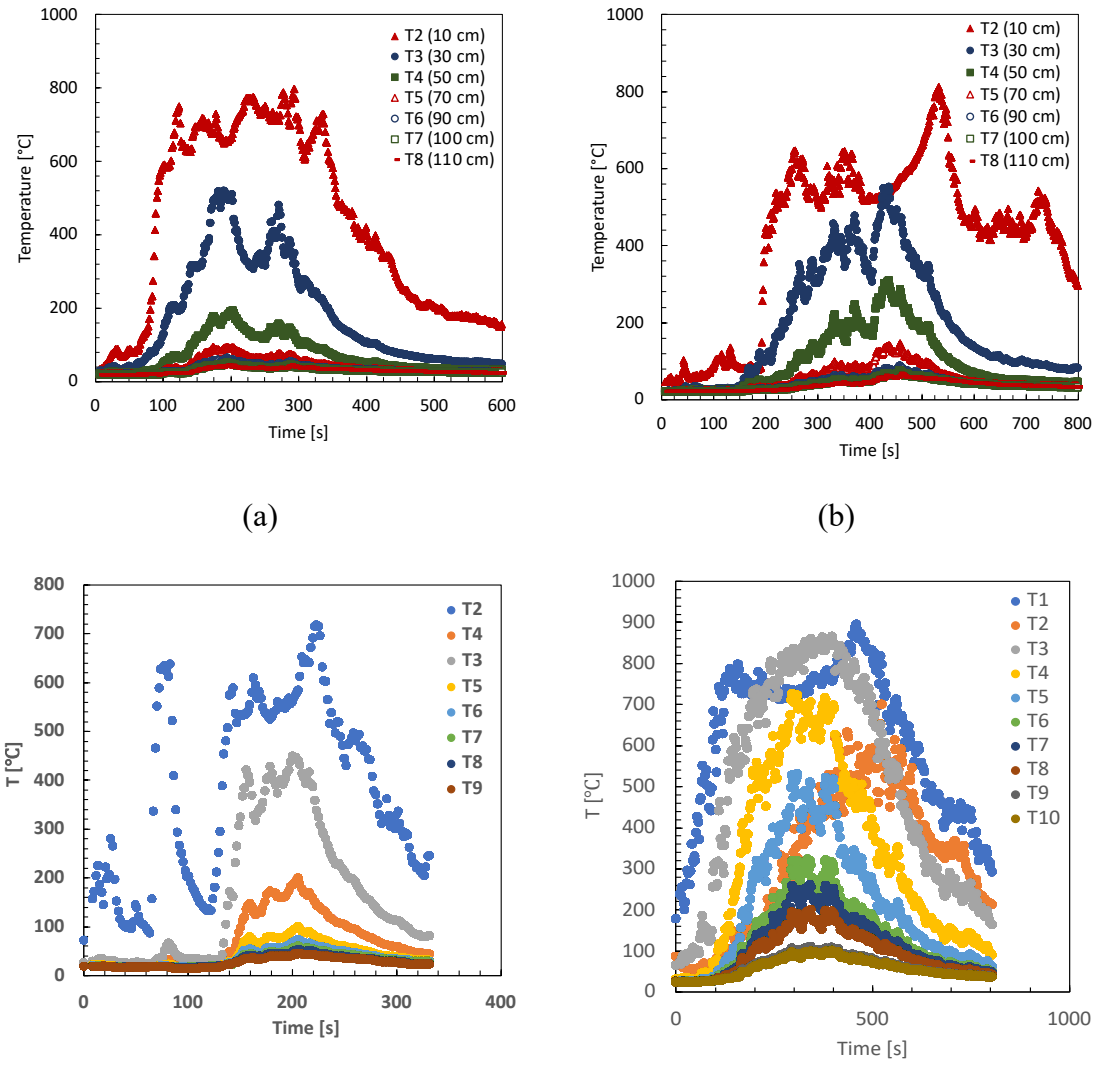

Figure 6-15: Centreline temperature profiles over time for (a) 6 in crib with n= 5, (b) 6 in crib with n = 7, (c) 3 in crib with n = 5, and (d) 9 in crib with n = 5.

Radiation from a crib fire is partially conserved within the structure and likely has an impact on centreline temperature. The 3 in cribs produce a small flame that wanders significantly about the thermocouple. Due to this wandering, the response time of the thermocouple means that measured temperature of the flame lags behind the actual temperature. Furthermore, the rate of heat transferred to the thermocouple changes over

time. Therefore, the recorded temperature profile is less than expected, as shown in Fig. 6-16.

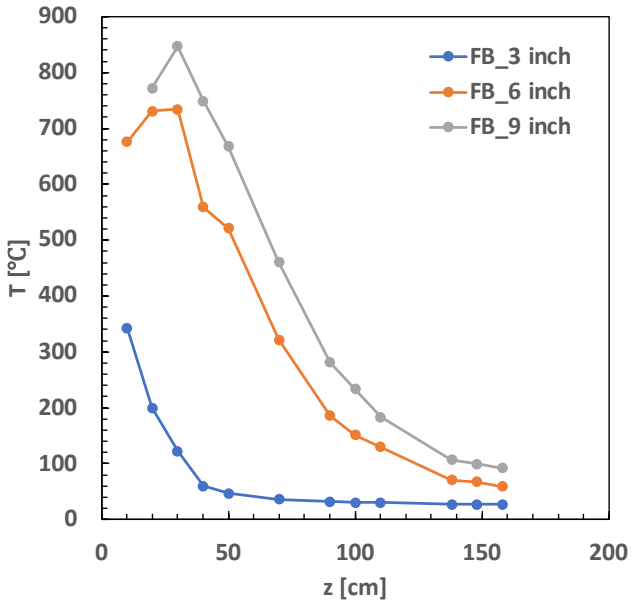

Figure 6-16: Centreline temperature profiles for 3, 6, and 9 in cribs with n = 5.

The centreline temperature was analyzed as a function of height for all the crib structures by normalizing the heights ($Z = z/H$), where z is the height above the base of the crib, and then plotting on logarithmic scales. This analysis shows the trends within the continuous flame region, intermittent region, and plume region. In all cases for the FB crib fires, the centreline temperature decreases with Z, as seen in Fig. 6-17. When normalizing the heights, the data shows that as the crib length increases the centreline temperature values merge. Therefore, less dependence on the number of sticks per layer is observed as the crib size increases.

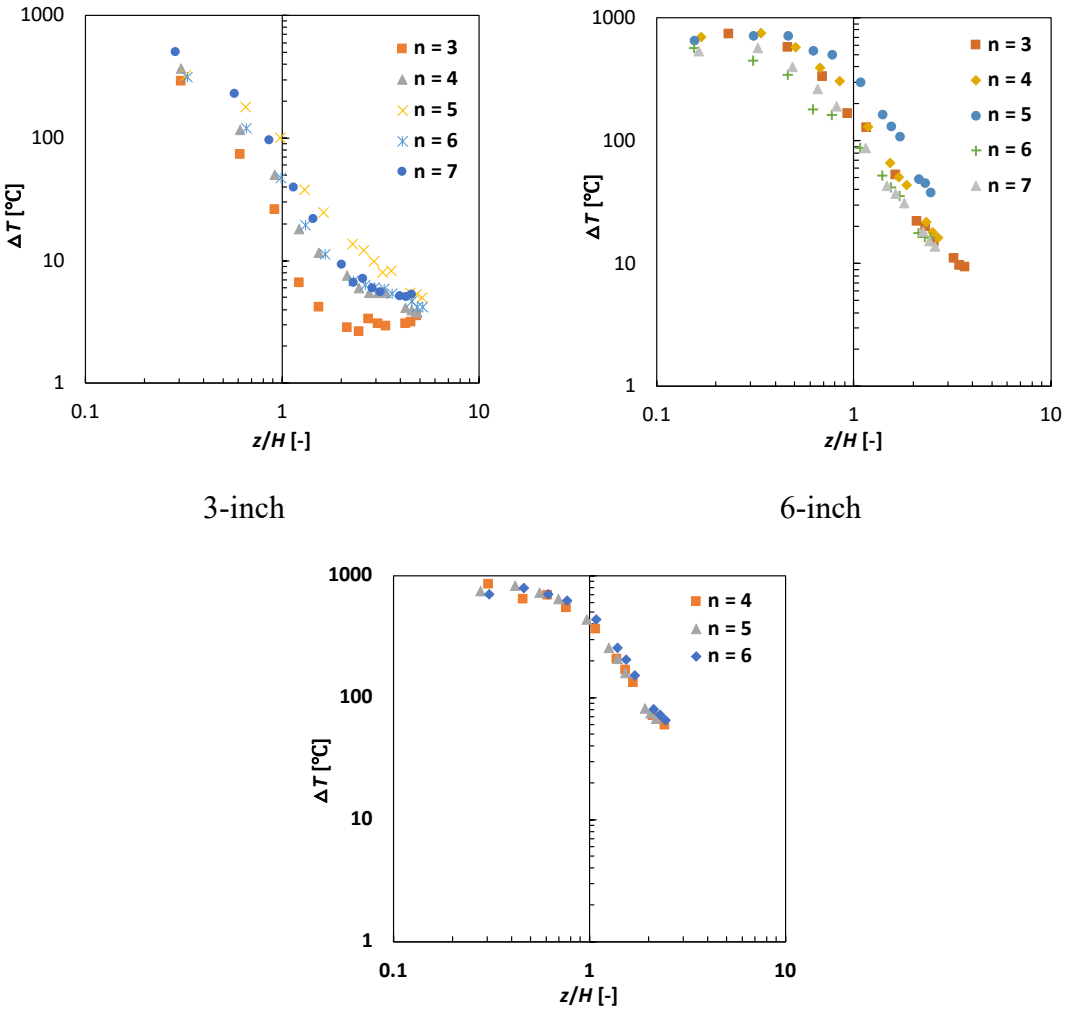

Figure 6-17: Centreline temperature plotted as a function of the normalized flame height for all three crib sizes.

6.2. Fire Whirl Cribs

Following the same format as the analysis for the FB crib fires, the flame heights, burning rates, flame spread rates, and centreline temperature profiles were investigated for propagating FW crib fires.

6.2.1. Flame heights

The fire whirl begins to precess at 5 – 25 s, except for the 3-inch crib with $n = 7$, where it took 120 s for the FW to begin. In this case an abundance of smoke was produced, and the smoke began to whirl. The crib also needed to be supported above the platform on two sticks, which raised it by 6.35 mm, as the side openings did not allow enough air for combustion (see Fig. 6-18).

Figure 6-18: The smoke forming for the 3 in crib FW with $n = 7$ at 25 seconds.

The duration of precession varies greatly for each crib size. The time the FW flame took to precess was a lot longer in crib fires than in the gaseous FWs. In some cases it took up to 120 s for a stable fire whirl to form. The duration of stable FWs for different cribs is shown in Table 6-5. The 3 in cribs produce less heat than the 6 and 9 in cribs. Therefore, they took a longer time to form a stable whirl because it took longer to heat the walls of the FWG. The average precession time was approximately 170, 99, and 100 s for the 3, 6, and 9 in cribs.

Table 6-5: The duration of a stable FWs for different crib configurations.

n	**3-inch [s]**	**6-inch [s]**	**9-inch [s]**
3	2.5	135	150
4	11.5	160	220
5	23	203	245
6	34	163	385
7	64	300	–

It is important to note that, when a stable FW was formed for the 3-inch crib, it only lasted 2–23 s for n = 3, 4, and 5. The reason for this short FW duration is that most of the fuel has been consumed before FW formation, as shown in Fig. 6-19.

(a) (b)

Figure 6-19: The 3 in crib with n = 5 (a) forming a stable FW and (b) close up view of the crib.

The ratio of l/n controls air flow rate into the crib structure and a power relationship arises when plotting the flame height against this parameter, as shown in Fig. 6-20(a). When

plotting the flame height against n, a linear correlation was produced, as shown in Fig. 6-20(b). This was different for the FB crib flame heights, which yielded a quadratic correlation in both cases. Figure 6-20(b) shows that, the more fuel a FW crib has, the larger the flame height formed. No maximum value of n can be identified, but the slopes indicate the rate at which the flame height increases per number of sticks. These correlations do not have an intercept as they would have no physical meaning. The slopes for the 9 in, 6 in, and 3 in cribs in Fig. 6.20(b) are m_9, m_6, and m_3. Their ratios are $m_9/m_3 = 2.13$, $m_6/m_3 = 1.79$, and $m_9/m_6 = 1.18$. This indicates that, as the crib length and size increase, the ratio of the slopes decreases.

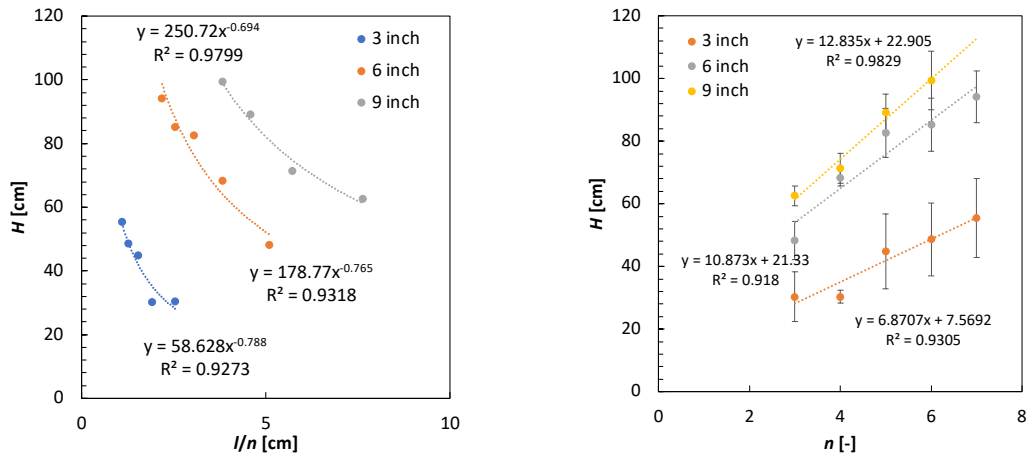

(a) (b)

Figure 6-20: Flame height for crib FWs for all three crib sizes plotted against (a) *l/n* and (b) *n*.

To determine if the crib height h had a significant impact on the average flame heights H, the height of the crib was subtracted from the average flame height $(H - h = h_f)$, as shown in Fig. 6-21.

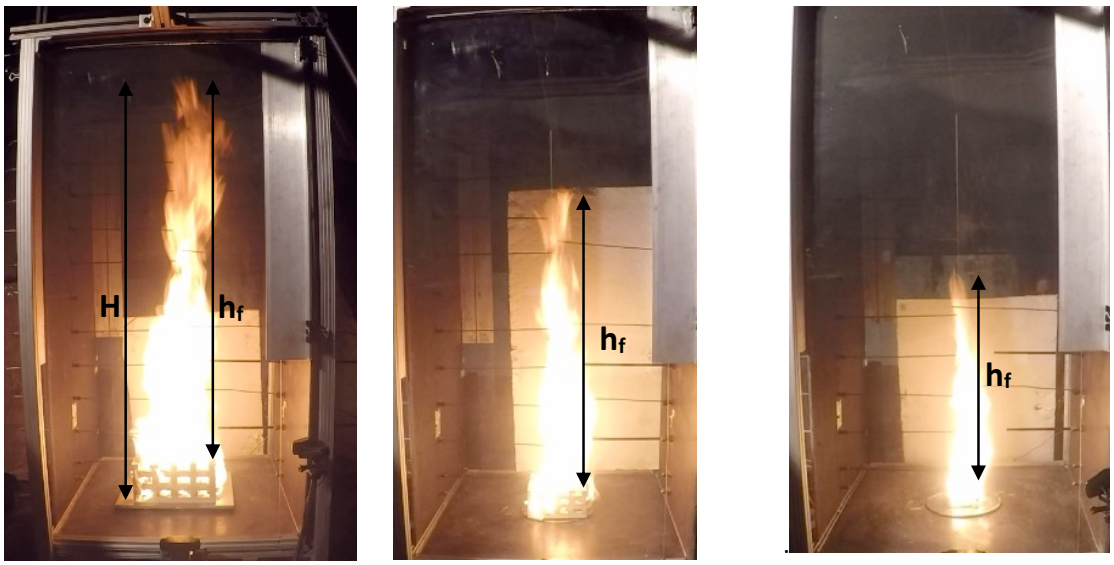

Figure 6-21: The three crib sizes showing the h_f measurement: 9 in crib (left), 6 in crib (middle), and 3 in crib (right).

Figure 6-22 proves that the flame height is dependent on the crib length (size), whereas the gaseous flame heights were not dependent on burner size. However, there was no difference in the trends between plotting H or h_f. Due to the chamber wall height effect observed for propane FWs in Chapter 5, the 6 in crib flame height could be producing similar heights to the 9 in crib. The 9 in cribs would likely have produced larger flame heights if the chamber walls were higher.

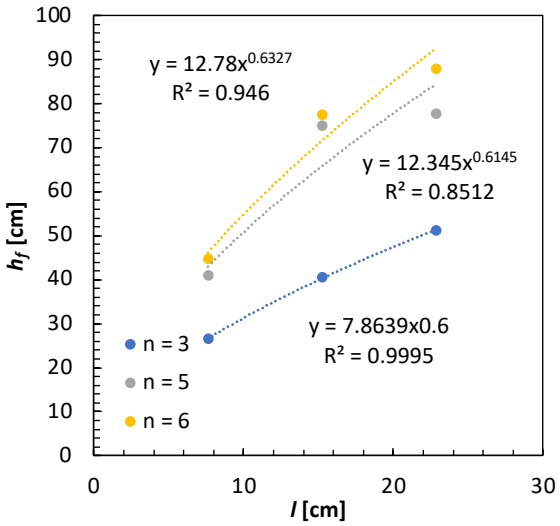

Figure 6-22: Flame height above the crib h_f *vs.* l correlations for crib FWs with 3, 6, and 9 in cribs.

The maximum FW flame heights H_{max} are plotted in Fig. 6-23 against the number of sticks per layer n, which produced a strong linear correlation (r^2 = 1 and 0.92). The difference between H_{max} and the average flame height ($H_{max} - H$) was 15–26 cm for the 3 in cribs, 15–32 cm for the 6 in cribs, and 15–27 cm for the 9 in cribs.

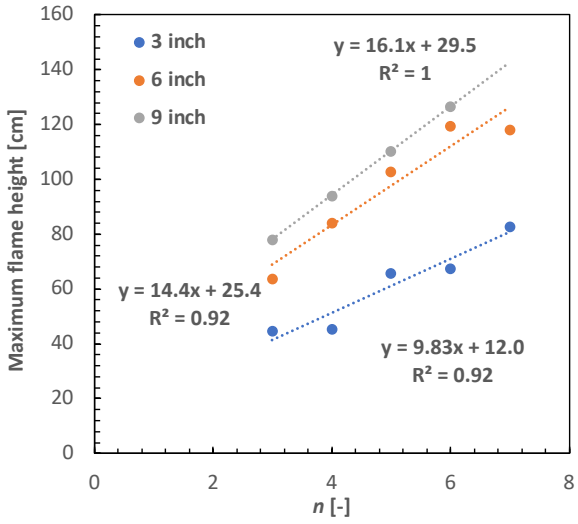

Figure 6-23: Maximum flame height plotted against number of sticks per layer for 3, 6, and 9 in crib FWs.

For all crib sizes, the difference between average and maximum flame heights for $n = 3$ was consistently 15 cm larger, and $n = 7$ produced the largest difference. The maximum peaks may only last 1–2 s, but it is still important to note the large maximum flame heights that they can produce.

As before, the maximum HRR was calculated by multiplying the FW peak burning rates by LHV. Following Heskestad, normalized flame height (*H/D*) was plotted *vs*. $\dot{Q}^*$ for the 6 and 9 in cribs, as shown in Fig. 6-24.

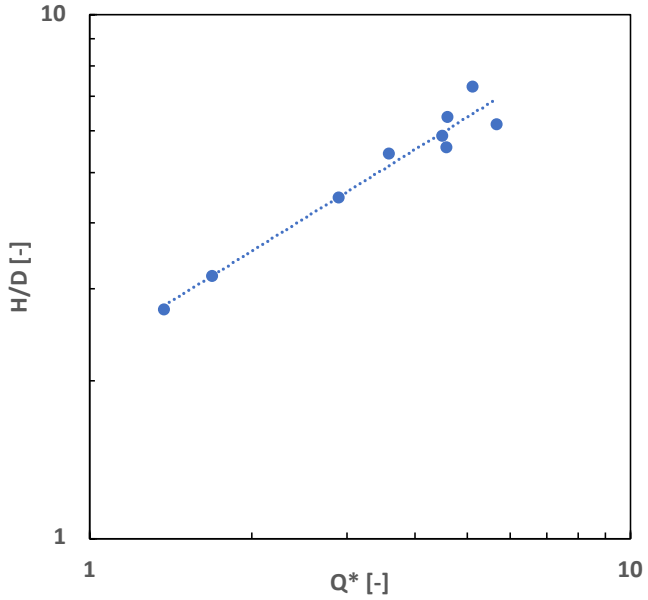

Figure 6-24: Normalized flame height plotted against $\dot{Q}^*$ for 6 and 9 in crib FWs.

Although the exponent was not 2/5, the plot produced a much better r^2 value than for the FB data. Comparing it to the propane FW flame height given by Eq. (5-5) ($H/D = 4.29\dot{Q}^{*2/5}$), the crib FWs produced half of the constant in front. The correlation is given by the following expression:

$$\frac{H}{D} = 2.27\dot{Q}^{*\,3/5} \qquad r^2 = 0.912 \qquad (6\text{-}4)$$

The correlation that Thomas proposed for *H/D* did not work well for the FW crib data (Eq. (2-35)).

6.2.2. Burning rates

The maximum burning rate occurs after the maximum flame height, which is shown in Fig. 6-25. The maximum flame height of the 3 in cribs consistently peaked closest to the peak burning rate, as shown in Fig. 6-25(c). This is due to the 3 in cribs not being able to form a stable FW until the chamber is sufficiently heated.

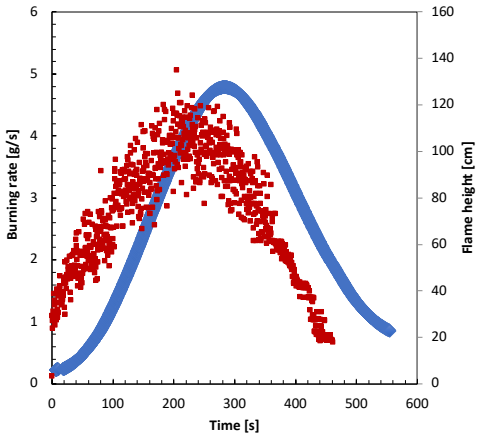

9-inch

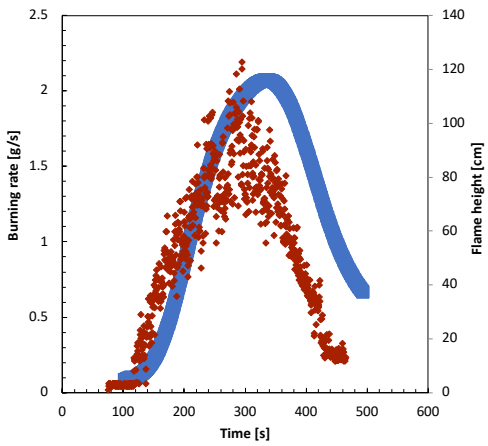

6-inch

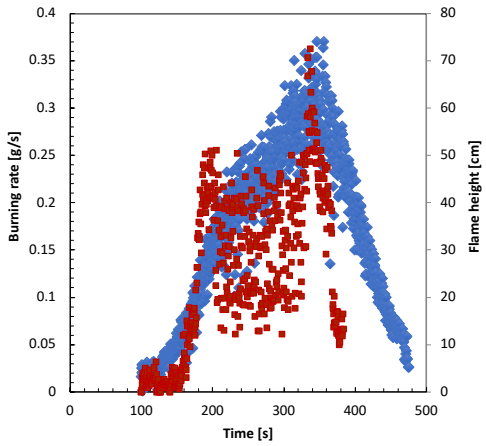

3-inch

Figure 6-25: The burning rate and flame height over time for all three cribs with $n = 6$.

The progression of a crib FW with $n = 5$ is shown in Fig. 6-26. The phases relative to the burning rate are as follows: (a) shows the onset of precession where the flame wanders around the internal structure of the crib; (b) is the point at which a stable FW is formed; (c) is when the fire has propagated to the edge of the crib; (d) is where the maximum burning rate occurs during the quasi-steady burning period; (e) shows a point where the height of the FW is decreasing as the burning rate decreases; and (f) shows the decay of the FW as the crib structure begins to collapse. This is followed by a period of embers during the tail

end of the burning rate curve. Although there is no longer a visible FW, small glowing particles can be seen swirling upwards from the embers.

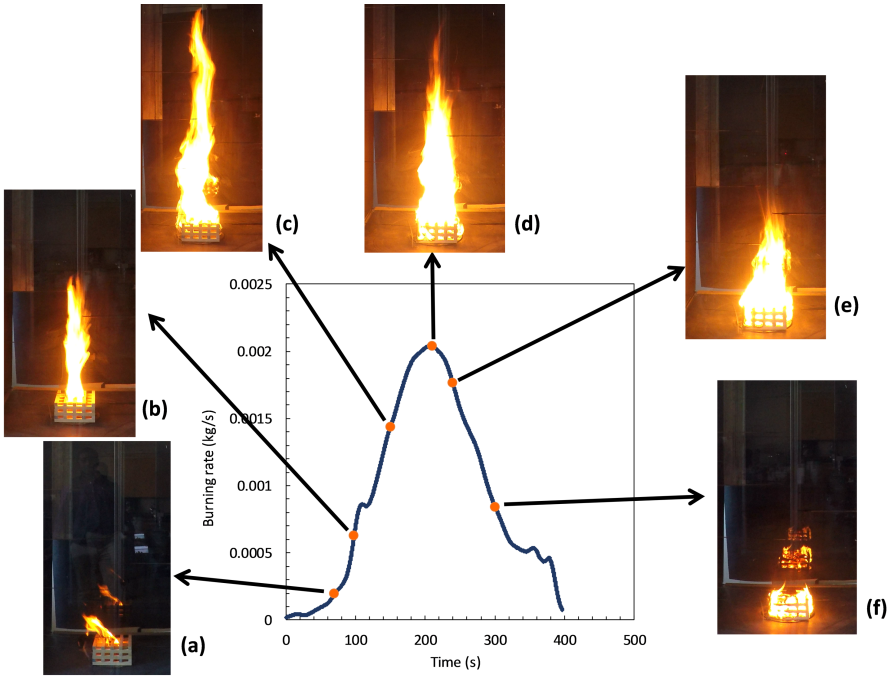

Figure 6-26: Progression of a crib FW with $n = 5$.

The burning rate was plotted against l/n, and a strong power correlation was produced. When plotted against only n, a strong linear correlation was formed for all three crib sizes, as shown in Fig. 6-27.

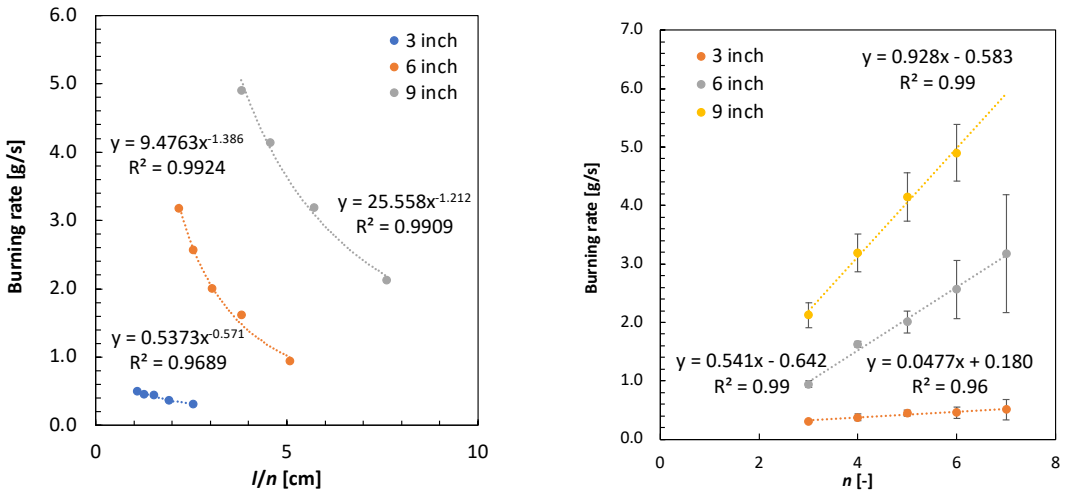

(a) (b)

Figure 6-27: Burning rate of 3, 6, and 9 in crib FWs plotted against (a) *l/n* and (b) sticks per layer *n*.

Plotting the burning rate according to the Thomas correlation (Eq. (6-1)), a similar result was obtained as for the FB data, which can be seen in Fig. 6-28(a). Each of the crib sizes produced three different power correlations with $r^2 > 0.99$. Using Eq. (6-2) to obtain one correlation for the 6 and 9 in cribs provides the result shown in Fig. 6-28(b). Once again, the 3 in crib did not coincide with the 6 and 9 in cribs and was plotted separately. Both correlations yielded $r^2 > 0.997$.

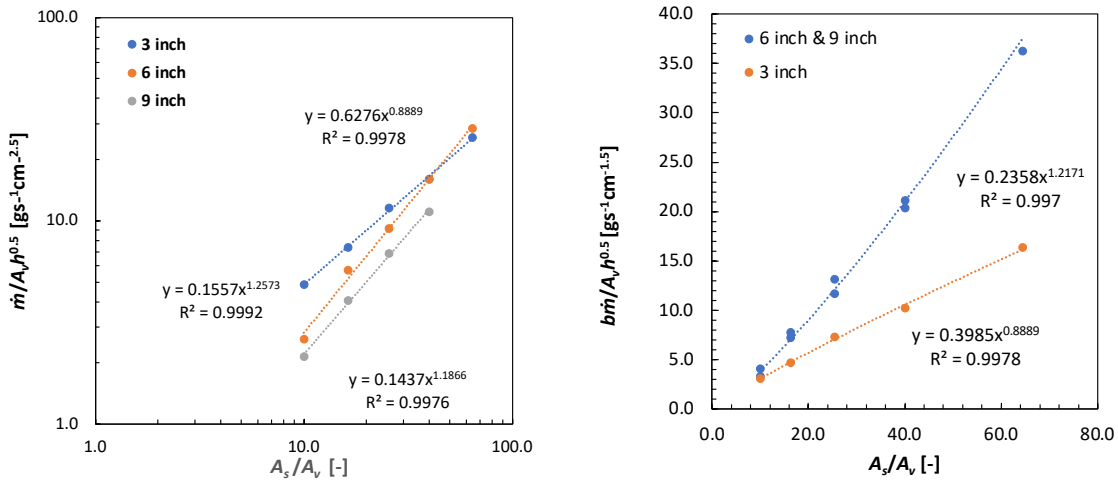

(a) (b)

Figure 6-28: Burning rate correlations (a) using the form of Thomas and Smith and (b) using the new correlation.

When plotting the burning rate against A_s, another strong correlation was produced ($r^2 = 0.965$); thus, the burning rate for crib FWs also has a strong dependence on A_s, shown in Fig. 6-29.

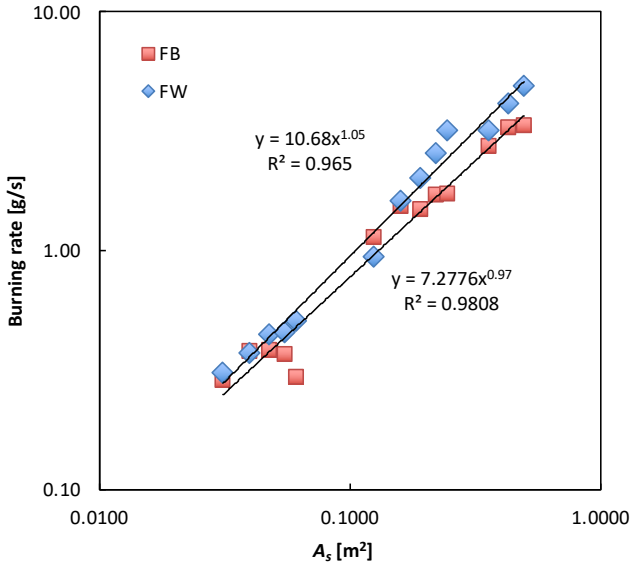

Figure 6-29: The crib FW and FB burning rates plotted against A_s.

6.2.3. Flame spread

Typical flame-front position issuing from the top surface of the crib *vs.* time data taken from the videos for the crib FWs is shown in Fig. 6-30. In the FW experiments, transition to a FW is not established until the air entrainment rate is sufficiently high to cause a strong swirling motion. Prior to formation of the FW, the flames rotate at the base of the crib due to the slow circulation of air in the chamber. Figure 6-30 shows images of the flame transitioning from the left side (LS) to the right side (RS) during the early stages of the test.

66 s (LS) 69 s (RS) 75 s (LS) 77 s (RS)

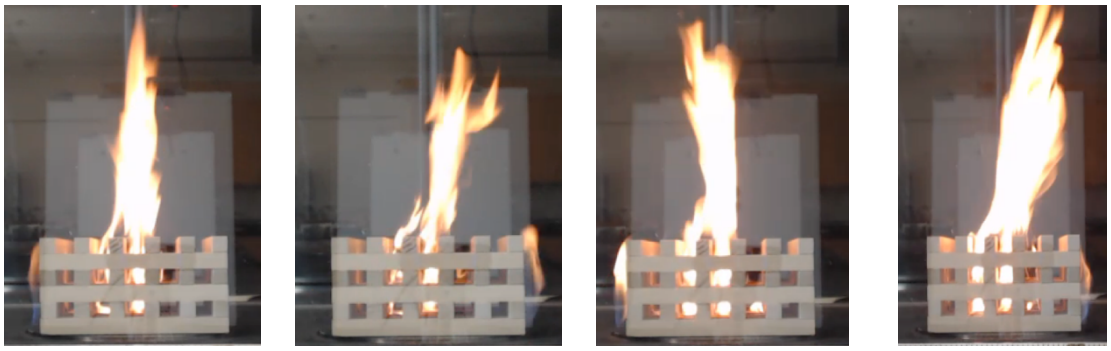

82 s (LS) 84 s (RS) 88 s (LS) 102 s (RS)

Figure 6-30: Images showing the progression of fire spread through a 6 in crib with $n = 6$ and flame rotation at the base prior to formation of a FW.

One of the factors that increases the spread rate for an FW and makes it different from an FB crib is the fire rotation and precession at the bottom of the crib. For the very open-

packed cribs (n = 3, ε = 0.75), the fire spread rate for the 6 and 9 in crib cases were 0.037 and 0.027 cm s^{-1}, which presented as outliers. These outliers were removed in Fig. 6-31 when showing the spread rate results. For the cribs with n = 4–7, the spread rate was found to fit a linear function of (l/n) with r^2 = 0.96, 0.98, and 0.999. The 3 and 6 in cribs produced very similar correlations resulting in only a 3% difference: $u_s = 0.0208(l/n)$, and $u_s = 0.0202(l/n)$. The 9 in crib appears to form its own trend: $u_s = 0.0121(l/n)$. The 6 in crib FW spread 67 % faster than the 9 in crib FW.

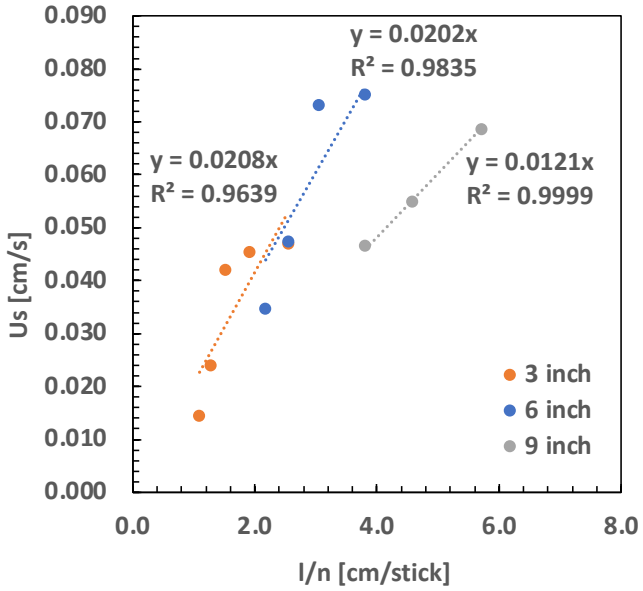

Figure 6-31: Fire spread rate plotted against *l/n* for all three crib sizes.

Images of the flame spread through the three different crib sizes are shown in Fig. 6-32.

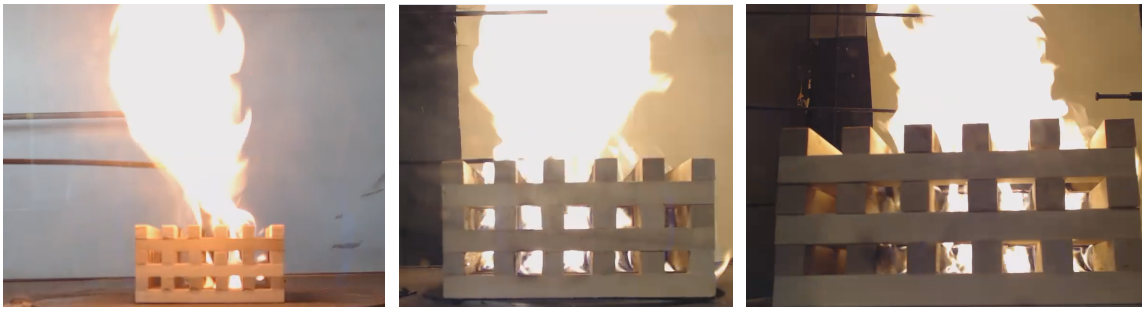

Figure 6-32: Images of the FW spread for the three crib sizes: 3 in crib (left), 6 in crib (middle), and 9 in crib (right).

6.2.4. Flame temperature

The thermocouple probes were placed in various locations for repeat experiments with the same geometrical configurations. In these experiments, no significant difference in the behaviour of the crib FWs was observed, and thus it was concluded that the presence of the thermocouple probes did not act as an appreciable heat sink or significantly disturbance to the flow. There was also no evidence of the flame anchoring to the probes.

Figures 6-33(a) and (b) show the temperature profiles of the 6 in FW tests for $n = 5$ and 7. The flame spread from 0 to 80 s with an approximate flame height of 20 cm for $n = 5$, whereas the flame did not begin to spread in the $n = 7$ test until 150 s after ignition. As the number of sticks per layer increased, so did the time for flame propagation. The flame begins to wander between 80 and 100 s for $n = 5$ and between 260 and 280 s for $n = 7$. The FW had fully formed at 100 s with a flame height between 40 and 50 cm for $n = 5$ and at 290 s with an approximate flame height between 45 and 55 cm for $n = 7$. The flame had completely propagated to the edge of the crib at 150 s and grew from 50 to 90 cm for the $n = 5$ test. For $n = 7$, the flame spread was complete at 390 s with a flame height of 100 cm (T7). Many of the thermocouples reached a maximum peak temperature at roughly 200 s for $n = 5$; the fire whirl was centered with approximate heights between T5 and T6 (70–

90 cm). For the $n = 7$ test, the maximum temperature was reached at approximately 420 s with a flame height around T7 (100 cm). The height fluctuation can be seen by the temperature difference in both tests. Since the $n = 7$ experiment produced higher flame heights, the temperatures were higher than in the $n = 5$ test. The flame began to decrease in height at 225 s and 460 s for $n = 5$ and 7 to approximately 50 cm. When the fire whirl ceased at 300 s for $n = 5$ there was still a strong circulation as the ashes were still spiraling around the chamber. The wood continued to smolder even after the fire had extinguished. The smoldering of wood lasted much longer in the $n = 7$ test due to the larger mass of fuel associated with the increased number of sticks per layer.

Furthermore, Figs. 6-33(a) and (b) show that the centreline temperature increases rapidly once the fire whirl is formed, but there is less fluctuation in temperature over time, which appears to be due to less of a wandering effect. This indicates that fire whirls associated with solid structures tend to be more stable than those associated with pool fires (Lei, *et al.* 2015).

Figure 6-33(c) shows that the 3 in crib a fire whirl started precessing from 35 to 145 s, which is shown by the fluctuation in the thermocouple readings. The FW formed after 138 to 166 s, but the flame kept moving in and out of the thermocouple location. Similar to the FB 3 in crib, as the flame position fluctuates, the air cools down the thermocouple, leading to lower temperature measurements, as illustrated in Fig. 6-34.

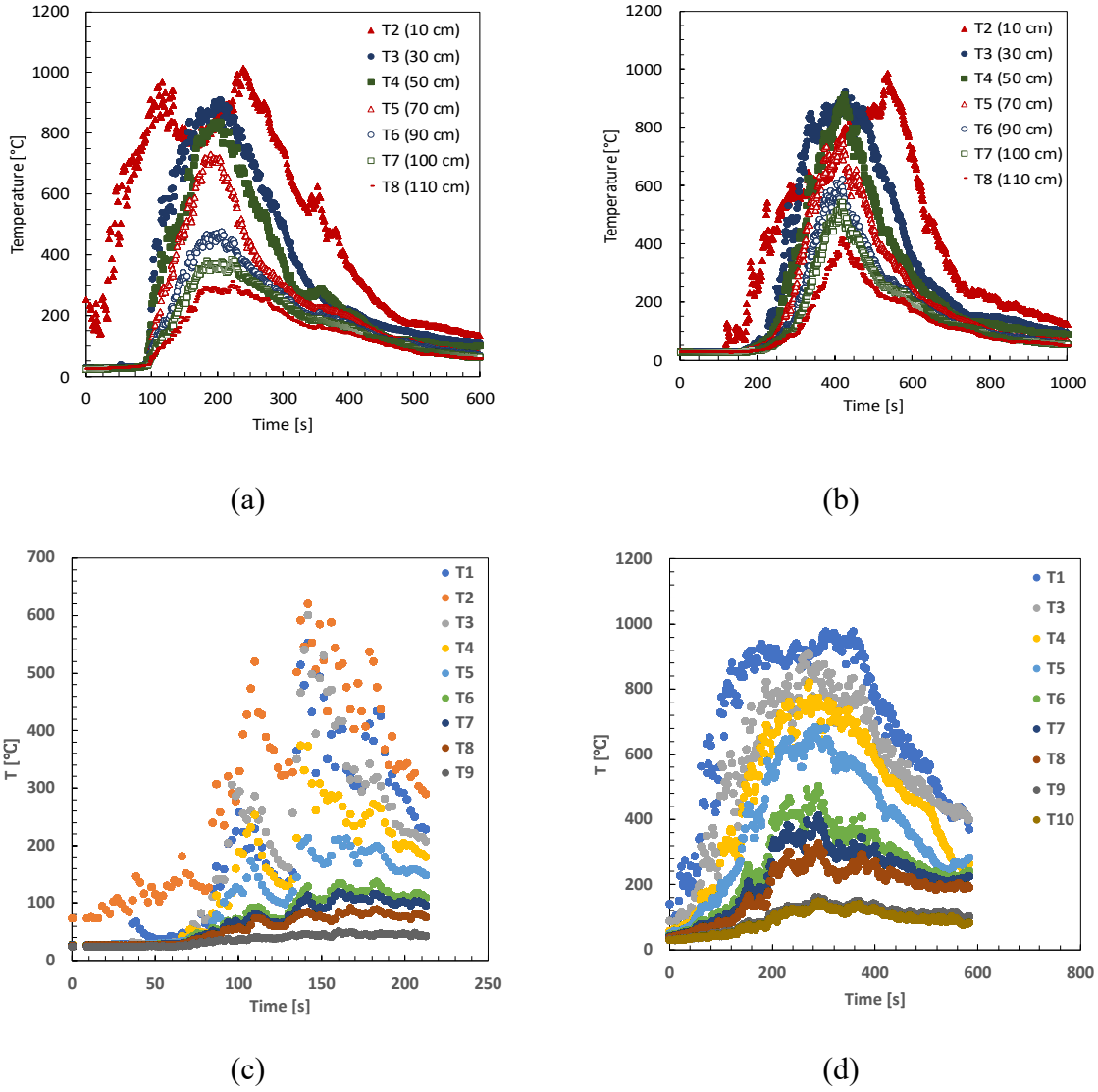

Figure 6-33: The centreline temperature profiles for crib FWs for (a) 6 in crib with $n = 5$, (b) 6 in crib with $n = 7$, (c) 3 in crib with $n = 5$, and (d) 9 in crib with $n = 5$.

Figure 6-33(d) shows that the FW for the 9 in crib with $n = 5$ began precessing from 25 to 99 s after ignition, and the fire whirl formed from 100 to 330 s. The 9 in crib FW temperature profiles are similar to the 6 in cribs; however, the peak temperature was sustained for longer since there is more fuel, which allows the FW to last longer. The temperature stability increased as the size of the crib increased.

Figure 6-34: Flame fluctuation in the 3 in crib for n = 3 (top) and n = 5 (bottom).

In the continuous flame region, the centreline temperature for open-packed cribs was correlated by $z/H^{0.65}$. However, the centreline temperatures for close-packed cribs do not follow those trends in the continuous flame region and were correlated by $z/H^{-0.76}$. The intermittent and plume regions decrease with similar exponents on z/H as determined by Lei *et al.* (2015) who stated the slopes do not overlap in the plume region as they are dependent on HRR. Data for the lower HRRs are further away from the y-axis, which is also shown for the 6 in cribs, as the open-packed crib (n = 3) is the farthest away, (Fig. 6-35(a)). The 9 in crib shows that the temperature profiles for different HRRs are very similar as the lines all merge together, as shown in Fig. 6-35(b).

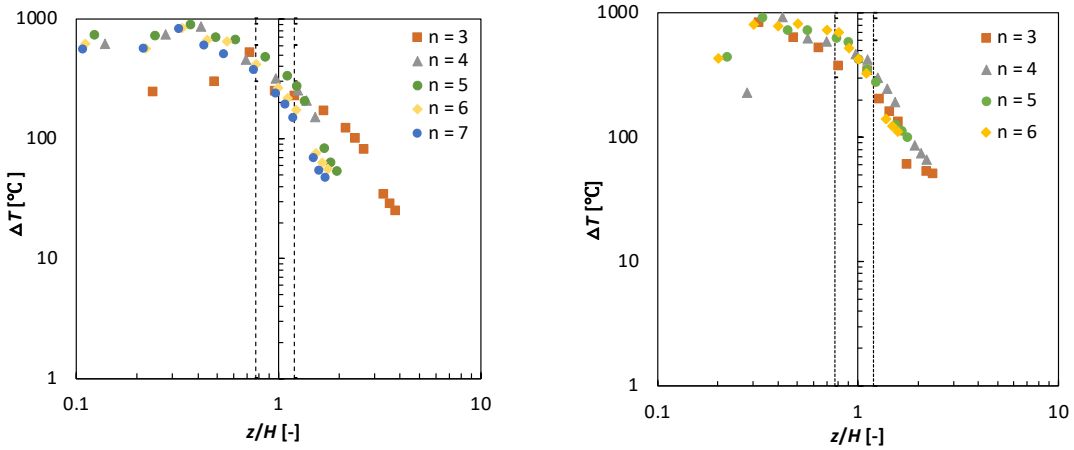

(a) (b)

Figure 6-35: Centreline temperature *vs.* the normalized height for (a) 6 in crib FW and (b) 9 in crib FW experiments. The black dotted lines are the extent of the intermittent regions.

The exponents for the centreline temperature correlations are provided in Table 6-6 for gaseous FW data from literature (Lei *et al.* 2015), the gaseous fire whirl data from this work described in Chapter 5, and the FW crib data from this work. In the intermittent region, all the exponents were within in the same range, with the 6 in crib producing the larger exponent, and the gaseous FW in Chapter 5 producing the smallest. In the plume region, all the exponents are also in the same range. This proves that regardless of the fuel type, it can be plotted using Lei's temperature correlation.

Table 6-6: Correlation exponents for centreline temperatures in the continuous, intermittent, and plume regions.

Fire Whirl Region	Exponent on Z	Reference	Fuel
Continuous flame	0.06	Lei (2015)	Gas
	0.24	This work	Gas
	0.65	This work (n = 3)	Solid (6-inch)
	–0.071	This work (n = 4–7)	Solid (6-inch)
	–0.36	This work (n = 4–6)	Solid (9-inch)
Intermittent	–1.79	Lei (2015)	Gas
	–1.42	This work	Gas
	–1.59	This work	Solid
	–1.96	This work (n = 4–7)	Solid (6-inch)
	–1.77	This work (n = 4-6)	Solid (9-inch)
Plume	–2.23 to –1.31	Lei (2015)	Gas
	–1.82	This work	Gas
	–2.55	This work (n = 3)	Solid (6-inch)
	–3.70 to –2.77	This work (n = 4–7)	Solid (6-inch)
	–2.5	This work (n = 4–6)	Solid (9-inch)

Comparing the centreline temperatures of the 6 in crib to the 9 in crib, as shown in Fig. 6-36, it is clear that the temperature profiles behave in a similar manner in the three regions independent of the size of the fuel bed.

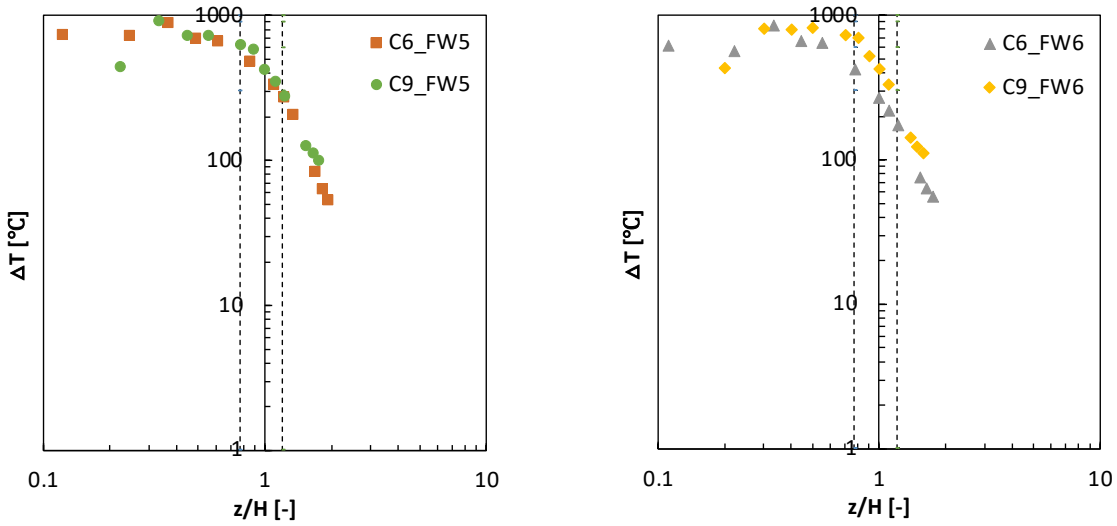

(a) (b)

Figure 6-36: Comparing the centreline temperature profiles of 6 and 9 in cribs with (a) $n = 5$ and (b) $n = 6$.

6.3. Comparison of Free Burning and Fire Whirl Crib Fires

A significant difference between a FB and FW crib fires is the amount of residue left at the end of the fire. Figure 6-37(a) shows that the FB structure collapsed and charred sticks remained, whereas in Fig. 6-37(b) it is seen that no charred sticks remain with the FW. The increased air entrainment and swirling of the air flow during the FW tests results in a residual vortex flow after the fire extinguished, thereby enhancing the smoldering rate and leading to significantly more char burnout. The FW rotation delivers oxygen very efficiently, thus allowing the fuel to burn significantly faster.

(a) (b)

Figure 6-37: Residual ashes remaining after (a) a FB crib fire and (b) a FW experiment.

The second most noticeable difference was the flame height. As discussed in Section 5.2, the FW flame heights are much greater than the FB flame heights. However, for the very open-packed cribs ($n = 3$, $\varepsilon = 0.75$), the average flame height of the FB and FW crib fires were almost identical, in all three cases. As the number of sticks per layer increased (*i.e.*, as the porosity decreased), the average flame height of FWs for the 3 in crib experiments increased from 0.8 (at $n = 3$ and 4) to 1.68 (at $n = 7$) times that of the FB cribs for the same geometrical configuration as shown in Fig. 6-38.

The FW flame heights for the 6 in crib experiments increased from 1.02 (at $n = 3$) to 1.41 (at $n = 7$) times that of FB flames and from 1.02 (at $n = 3$) to 1.31 (at $n = 6$) for the 9 in crib experiments.

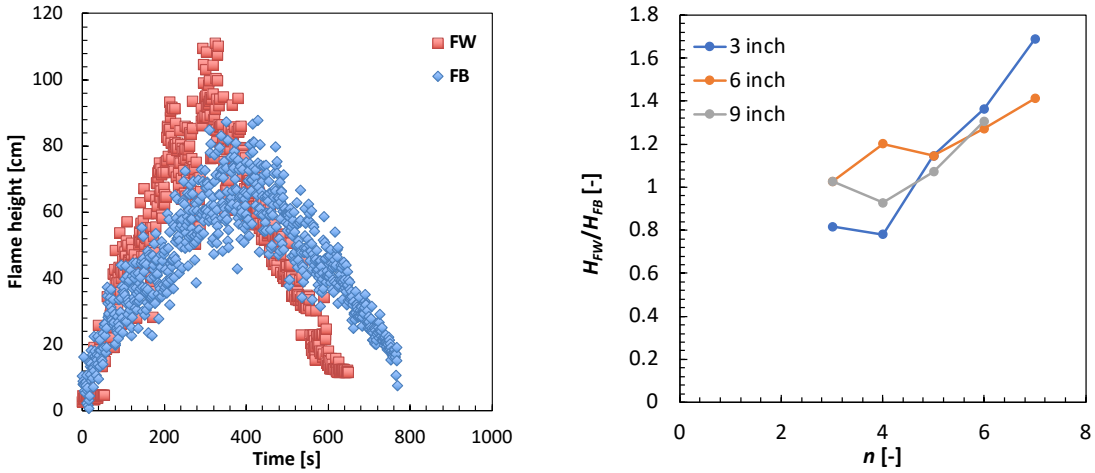

(b)

Figure 6-38: Flame height comparison (a) raw data for 6 in crib with n = 5 and (b) ratio.

However, comparing the 3 in cribs with n = 3 and 4 is not significant because the fire whirl flame height lasted less than 10 s. Additionally, as the flame precessed it was also tilted. Therefore, the vertical flame height could not readily be compared with that of the FB flame heights, which were not tilted. Figure 6-39 shows an example of this behaviour for the n = 4 case.

Figure 6-39: Images of the precession for the 3 in crib FW with n = 4.

The burning rate followed a similar trend to the flame heights; as the number of sticks per layer n increased so did the ratio $\dot{m}_{FW}/\dot{m}_{FB}$, as shown in Fig. 6-40. For the very open-

packed cribs ($n = 3$ and 4), the burning rates of the FB and FW crib fires were almost identical for the 3 and 6 in cribs. As n increased, the burning rate for FW tests increased from 1.0 (at $n = 3$) to 1.71 and 1.84 (at $n = 7$) times that of the FB cribs for the same geometric configuration. The 9 in crib FW burning rates ranged from 1.16 to 1.47 times greater than FB cribs.

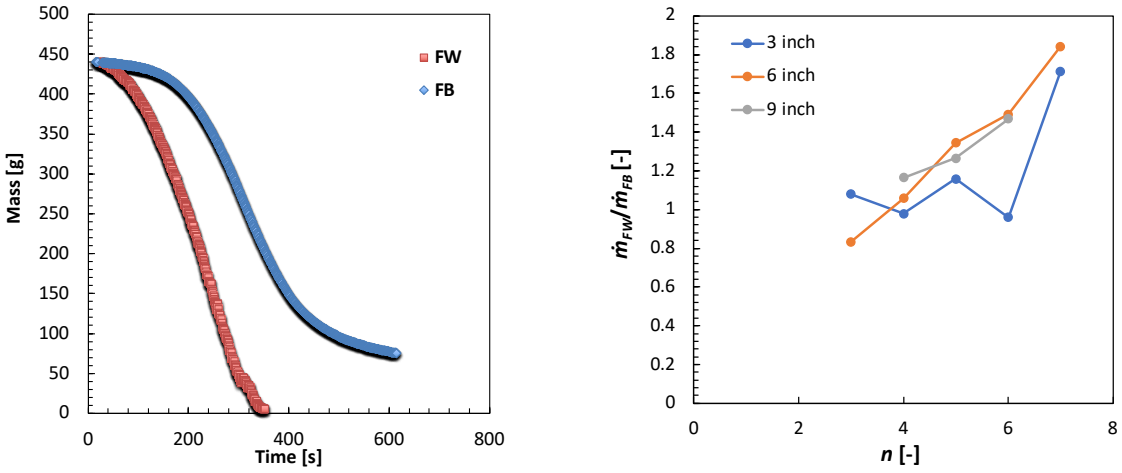

(a) (b)

Figure 6-40: The burning rate comparison for (a) raw data for 6 in crib with $n = 5$ and (b) burning rate ratio.

The spread rate followed the inverse of the flame height and burning rate trends. As n increased, the difference between the FW and the FB spread rates decreased, as shown in Fig. 6-41. The spread rate ratio for the very open-packed cribs ($n = 3$) of 6 and 9 in stick length caused an outlier shown by the square and triangle. This is most likely due to the fire whirl not forming as quickly and allowing the FB spread to be faster than the FW tests.

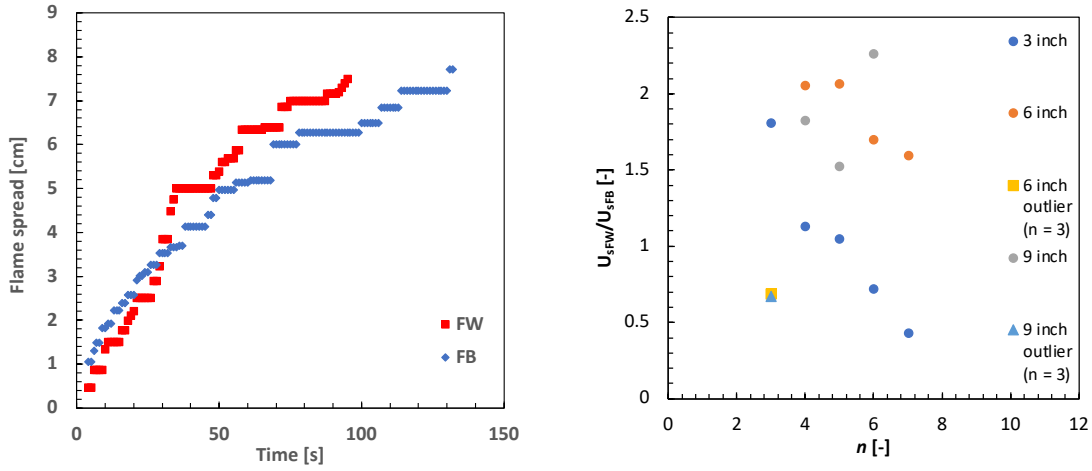

(a) (b)

Figure 6-41: Spread rate comparison for (a) raw data for 6 in crib with n = 5 and (b) spread rate ratio.

Figure 6-42(a) shows the ratio of the average FW to FB spread rate ratio *vs. s/l* and Fig. 6-42(b) shows the flame height ratio *vs. s/l*. The average spread rate ratio was found to follow a quadratic trend, which is reasonably well represented by the following correlations:

$$\text{3-inch} \quad \left(U_{s_{ave}}\right)_{FW}/\left(U_{s_{ave}}\right)_{FB} = -44.9\left(\frac{s}{l}\right)^2 + 17.7\left(\frac{s}{l}\right) - 0.59 \qquad r^2 = 0.999 \qquad (6\text{-}5)$$

$$\text{6-inch} \quad \left(U_{s_{ave}}\right)_{FW}/\left(U_{s_{ave}}\right)_{FB} = -35.1\left(\frac{s}{l}\right)^2 + 13.6\left(\frac{s}{l}\right) + 0.78 \qquad r^2 = 0.935 \qquad (6\text{-}6)$$

The ratio of flame heights was found to follow an empirical correlation and was fitted using the following expression (see Fig. 6-42(b)):

$$\text{3-inch} \quad (H_{ave})_{FW}/(H_{ave})_{FB} = 19.4\left(\frac{s}{l}\right)^2 - 11.4\left(\frac{s}{l}\right) + 2.36 \qquad r^2 = 0.992 \qquad (6\text{-}7)$$

$$\text{6-inch} \quad (H_{ave})_{FW}/(H_{ave})_{FB} = 2.98\left(\frac{s}{l}\right)^2 - 2.38\left(\frac{s}{l}\right) + 1.51 \qquad r^2 = 0.810 \qquad (6\text{-}8)$$

9-inch $$(H_{ave})_{FW}/(H_{ave})_{FB} = 14.1\left(\frac{s}{l}\right)^2 - 7.67\left(\frac{s}{l}\right) + 1.9 \qquad r^2 = 0.982 \qquad (6\text{-}9)$$

It is interesting to note that the flame height ratios for $s/l < 0.2$ were almost identical for the three crib sizes.

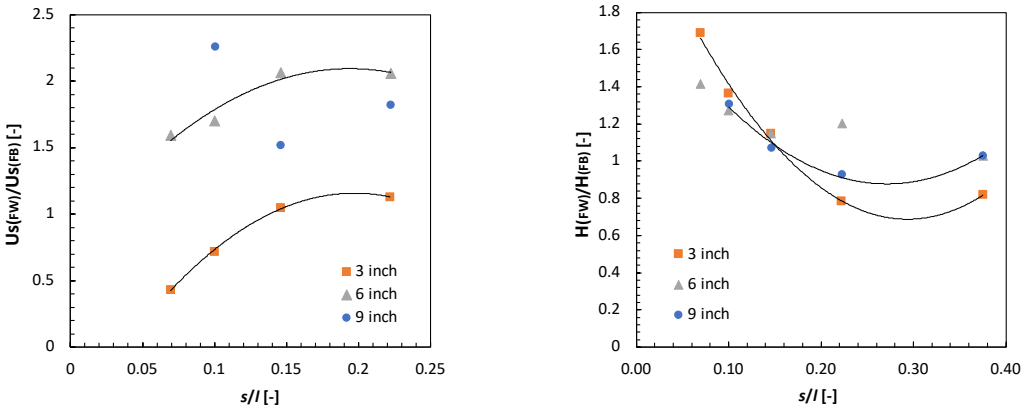

(a) Spread rate (b) Flame height

Figure 6-42: Ratio of FW and FB cribs for (a) spread rate data and (b) flame height data.

Figure 6-43(a) compares data from FWs with FB 6 in crib fires and shows that the temperature in the continuous flame is 2–3 times greater than that of the intermittent flame. The dramatic change in temperature is due to the intermittent region of the FB crib fires occurring at a much lower height than the FW crib fires. The temperature of the plume region of a FW crib fire is higher (> 200 °C) than that for a FB crib fire (≤ 100 °C). Figure 6-43(b) shows the ratio of the absolute temperature of a FW to that of a FB crib fire of the same geometrical configuration. For the cribs studied in this paper, this ratio is 0.99–1.2 at a height of 10 cm (in the flame core) as n ranges from 3–7.

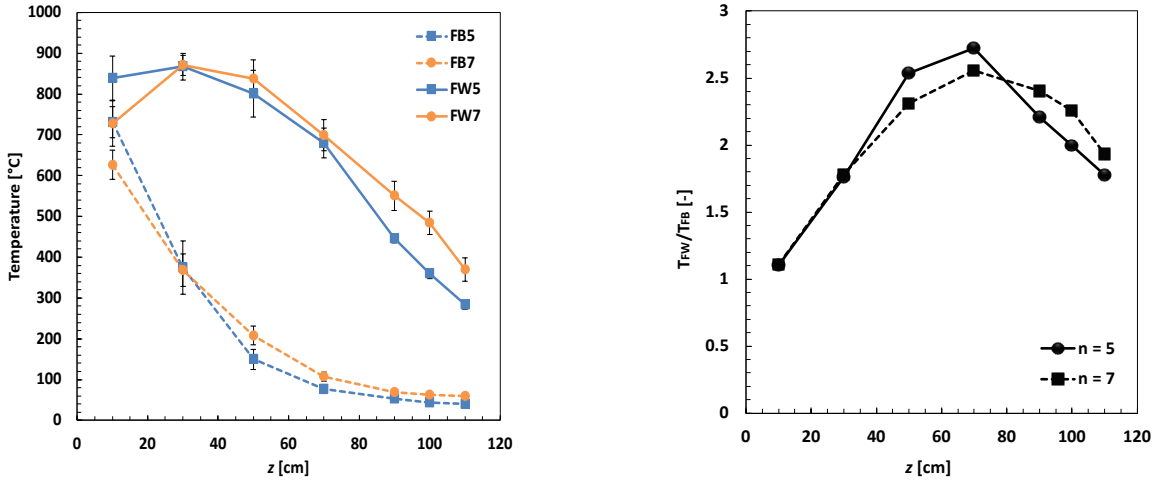

(a) (b)

Figure 6-43: Comparison of centreline temperature profiles for FB and FW 6 in crib fires. (a) Centreline temperature *vs.* height for n = 5 and 7 for FW and FB crib fires; and (b) temperature ratio of FW over FB crib fires for n = 5 and 7.

Comparing the FW and FB ratio for the three crib sizes with n = 6 (Fig. 6-44), the first peak is that of the 3 in crib at ~ 6 times greater, followed by the 6 in crib at ~ 4 times greater, and then the 9 in crib at 2 times greater. This demonstrates that as the crib increases in size the FW produces a higher temperature than the FB case when moving away from the core. This is due to the intermittent region of the FW being at a higher position when the crib length (and height) is larger.

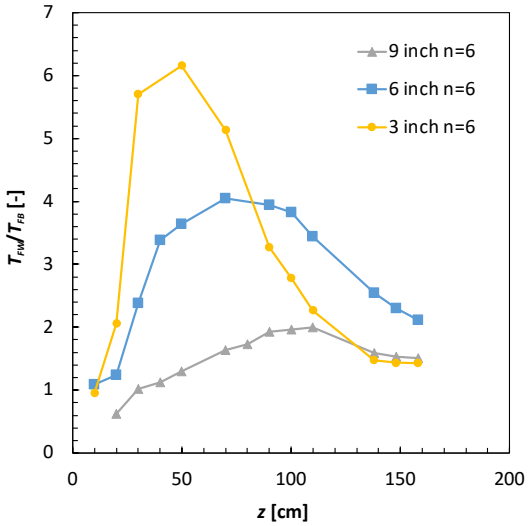

Figure 6-44: Comparison of the FW to FB centreline temperature ratio for different sizes of cribs.

Following Lei *et al.* (2015), the heights z at which centreline temperatures were measured for all the crib structures (both FB and FW) were normalized by the average flame height H, such that $Z = z/H$. Centreline temperatures for n = 4, 5, and 6 were plotted against their normalized height for 6 and 9 in cribs, as shown in Fig. 6-45. This allows for comparing the temperatures within the three different regions.

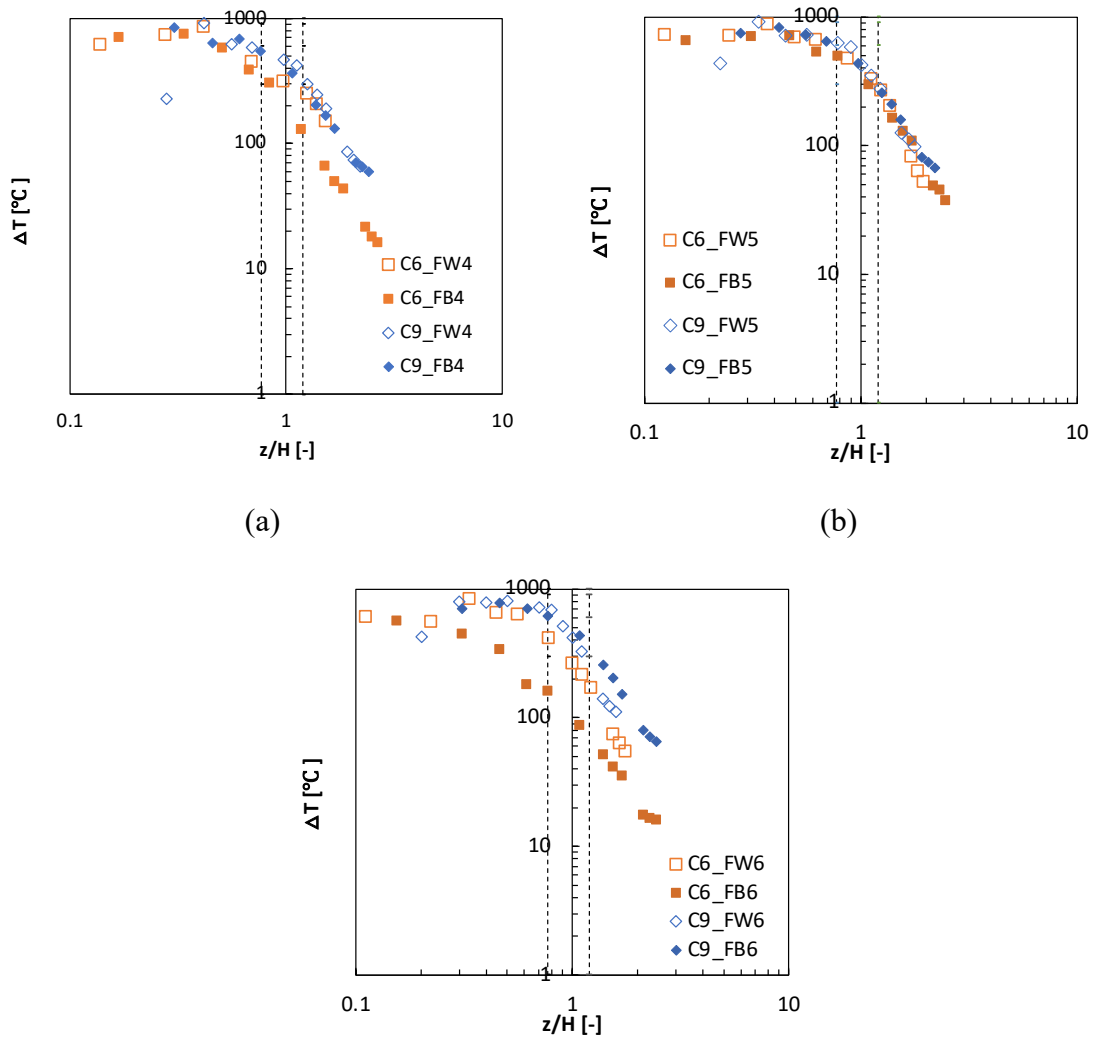

Figure 6-45: Centreline temperature *vs.* the normalized height for 6 and 9 in FB and FW cribs: (a) $n = 4$, (b) $n = 5$, and (c) $n = 6$. The black dotted lines show the extent of the intermittent regions.

For $n = 5$, the centreline temperature plotted against the normalized height of the FW and FB experiments (plotted as one data set) had very similar exponents in all three regions; therefore, the data were plotted together (Table 6-7). The intermittent region regardless of n had very similar exponents for z/H, which was expected according to Lei *et al.* (2015). All exponents on z/H in Table 6-7 were within the same range as the values stated in Table 6-6.

Table 6-7: Centreline temperatures for FW and FB in the continuous, intermittent, and plume regions

Flame Region	**Exponent on *z/H***	**Crib size (*l*)**	***n***
Continuous	–0.076	6-inch and 9-inch	5
Intermittent	–1.64	6-inch and 9-inch	5
	–1.74	6-inch and 9-inch	6
Plume	–2.74	6-inch and 9-inch	5

6.4. General Discussion

Three separate correlations were obtained with the ratio of *l*/*n,* which controls air flow rate into the crib structure, and the quadratic relationship arises because of the dependence of the pressure drop being a quadratic function of the air velocity $H = a(l/n)^2 + b(l/n) + c$. The flame height correlation proposed by Thomas (Eq. (2-35)) was satisfactory.

The FB crib burning rates were also correlated by quadratic relationship with *n*. The correlation of Smith and Thomas (Eq. (6-1)) was also satisfactory for all three crib sizes, although one form could not correlate all the data in a single relationship. However, by multiplying this equation by *b* (Eq. (6-2)), the 6 and 9 in cribs could be correlated by one relationship. Comparing this correlation with the data of Pegg, O'Dogherty & Young, and Webster (all propagating crib fires), all the data were satisfactorily correlated by $b\frac{\dot{m}}{A_v\sqrt{h}} = 1.2\left(\frac{A_s}{A_v}\right)^{0.56}$.

Plotting the burning rate against A_s also produces a good correlation for all the available burning rate data on propagating crib fires by $\dot{m} = 6.8A_s^{0.96}$. The FB spread rate was

determined to be inversely proportional to the length scale. The FB temperature data had significant fluctuations due to ghost flames. When plotting the centreline temperature against normalized heights, it showed less dependence on the number of sticks per layer as the crib size increased.

The FW flame heights produced linear correlations $H = mn$, where m is the slope, which is 8.3, 14.8, and 17.6 for the 3, 6, and 9 in cribs. This shows that as l and n increased so does the flame height. The maximum flame heights produced were 30–65% larger for the 3 in cribs, and 20–40% larger for the 6 in and 9 in cribs. The maximum flame height always occurred before the maximum burning rate. The burning rate produced a linear correlation with n, with slopes of 0.05, 0.54, and 0.93 for the 3, 6, and 9 in cribs. Once again, when plotting burning rate data according to Smith and Thomas, three correlations were produced; however, when multiplying by b, the 6 and 9 inc crib data resulted in one correlation with r^2 of 0.997. The FW centreline temperature profiles had a lot less fluctuation than the FB data and plotting against the normalized flame height the trends were very similar to Lei *et al.* (2015). In the intermittent region the data could be plotted as one set, whereas in the plume region for the 6 in crib each n had their own exponential correlations. Lei *et al.* (2015) states this is due to the different HRRs.

Comparing the FB and FW flame, the FW is observed to produce a less luminous flame and is much cleaner burning. This can be seen by the residual ashes remaining from the two types of experiments. The FW flame heights were between 1 and 1.4 times larger in the 6 and 9 in cribs. The burning rates for the FW flames were 1.2 to 1.8 times larger than the FB flame, and as n increased so did the difference between FW and FB. The FW spread

rates are 1.5 to 2.3 times larger than for FB cribs. At the peak temperature, the centreline temperature was 2.5 times larger in FWs than for FB crib fires.

Chapter 7: Conclusions and Future Work

7.1. Conclusions

Fire whirls are special types of flames that are caused by the interaction of the buoyancy-driven rise of hot combustion gases in a fire and swirling wind conditions. Unfortunately, the spinning behaviour that makes fire whirls fascinating to observe also makes them highly unpredictable and dangerous. The formation of fire whirls can greatly increase the flame height, temperature, burning rate, and spreading rate and decrease the predictability of wildfires, residential and commercial building fires, and industrial fires. Compared with the FB flame, the maximum flame heights of FW flames increased significantly, whereas the same HRR is obtained for a smaller diameter of the fuel (width).

The gaseous FW experiments and simulations showed that the flame heights were dependent on the HRR, gap-width, the chamber's hood, and wall height. The FB and FW flame heights were plotted against $\dot{Q}^*$ to obtain the following relationships:

Gaseous FB: $$\frac{H}{D} = 3.2Q^{*2/5}$$

Gaseous FW: $$\frac{H}{D} = 4.29\dot{Q}^{*2/5}$$

Surprisingly, the burner diameter and the number of inlets did not produce a significant change in flame height or flame temperature, except in the 1-inlet case where a stable FW did not form. The simulations predicted accurate flame heights compared with the experimental data. The simulations underpredicted the flame temperature but still

displayed similar trends. The model predictions are in good agreement with the experimental data of gaseous FWs. The model was used to perform an analysis on the wall height effect. It predicted that there is a significant flame height dependency on the wall height for large HRR and less of an impact for small HRR, relative to the size of the chamber.

For the crib study, a stable FW formed in all cases. For the 3 in cribs, the burning duration was 2–15 s depending on the number of sticks per layer. The flame precessed for most of the time; however, it is impressive that the FW was still able to form with the minimal amount of fuel that the 3 in cribs have. This demonstrates that occurrence of a FW can happen from just a little bush fire or bonfire. The 6 in and 9 in cribs formed a stable FW quickly, and the burning duration was between 135 and 385 s.

The FW flame height for the crib fires increased as the number of sticks increased, whereas the FB flame height had a peak around $n = 5$. This means that, although the mass increased for the FB cases, the flame height reaches a maximum height and plateaus. The FW flame heights continue to increase linearly as the number of sticks increase for all crib packing densities studied in this work. As l increases the flame heights increase according to $H = al^{0.6}$, where a is a constant. The FB and FW flame heights were plotted against $\dot{Q}^*$ to obtain the following expressions:

Crib FW: $$\frac{H}{D} = 2.27\dot{Q}^{*3/5}$$

Crib FB: $$\frac{H}{D} = 2.73\dot{Q}^{*2/5}$$

The maximum FW flame heights were at times 40–60 % larger than the reported average flame heights. The 6 and 9 in cribs had FW flame heights 1.2, 1.3, and 1.4 times larger than their FB counterpart for n = 5, 6, and 7.

The burning rates were all plotted with a modified Thomas correlation: $b\frac{\dot{m}}{A_v\sqrt{h}} = k\left(\frac{A_s}{A_v}\right)^a$. This proved to be the best correlation for FB and FW crib fires. A very strong correlation was produced between the burning rate and the total exposed surface area, A_s for both FW and FB cribs. Comparing the FW burning rate with that of the FB cribs, the maximum burning rate difference for FW cribs was approximately 1.8 and 1.5 times larger for 6 and 9 in cribs than for the FB cribs. There was a lot less residue remaining with the FWs and the ashes whirled around the chamber long after the flame burned out. The whirling ashes demonstrates how spot fires could form when FWs are present.

The FW spread rates were 1.5–2.3 times larger than the FB flames and produced a linear correlation with *l/n*. The FW flame temperature was within the Lei *et al*. (2015) *z/H* power correlation for centreline temperature, which can be used at these crib sizes to calculate an approximate centreline flame temperature given an average flame height.

Comparing the significant difference between FW and FB flame heights, burning rates, spread rates, and temperature profiles, emphasizes the importance of educating people (i.e., fire practitioners, industrial workers etc.) on these differences. This work highlights the importance and benefits of teaching the dynamics of FW to fire fighters entering the field.

7.2. Future Work

Fire whirls generated in a fixed-frame apparatus are formed by air being drawn in tangentially as a result of the buoyancy of the fire. In other words, they are naturally aspirated. It was anticipated that the scaling study on crib FWs would provide information to relate the flame height and burning rate to the geometry of the apparatus, but this was not realized. Future work should be undertaken to scale not only the size of the fire source but also the size of the apparatus to determining the relationship between the geometry and the flame height and burning rate. If this were achieved, then it would be possible to predict flame heights from the HRR and geometry, which would be helpful in assessing the hazards in building fires, especially in atria.

Additionally, there is a significant difference in the way the flame propagates and spreads between a FB and FW in crib fires. With FB crib fires the flame spreads uniformly within the crib and involves more of the surface area of the sticks, until it reaches the outside of the crib. However, with a FW the flame continuously circulates within the crib structure and therefore the amount of fuel surface involved varies, resulting in a significant part of the structure being burned before it reaches the outside of the crib and forms a stable FW. This complex behavior needs a more in-depth technique to investigate the spread rate.

References

Battaglia, F., Mcgrattan, K., Rehm, R., Baum, H., 2000. Simulating fire whirls. Combustion Theory and Modelling 4, 123–138. https://doi.org/10.1088/1364-7830/4/2/303

Baukal, C.E., 2018. Pillar of Fire Theories. null 32, 217–235. https://doi.org/10.1080/09018328.2018.1470847

Block, J.A., 1971. A theoretical and experimental study of nonpropagating free-burning fires. Symposium (International) on Combustion 13, 971–978. https://doi.org/10.1016/S0082-0784(71)80097-8

Bradley, D., Gaskell, P.H., Gu, X., Palacios, A., 2016. Jet flame heights, lift-off distances, and mean flame surface density for extensive ranges of fuels and flow rates. Combustion and Flame 164, 400–409. https://doi.org/10.1016/j.combustflame.2015.09.009

Byram, G.M., Martin, R.E., 1970. The modeling of fire whirlwinds. Forest Science 16, 386–399.

CBC News. 2016a. Dramatic footage shows “fire tornado” in St. Albert.

CBC News, 2016b. “Firenado” caught on video in southern California.

Chow, W.K., Dang, J.F., Gao, Y., Chow, C.L., 2017. Dependence of flame height of internal fire whirl in a vertical shaft on fuel burning rate in pool fire. Applied Thermal Engineering 121, 712–720. https://doi.org/10.1016/j.applthermaleng.2017.04.108

Chow, W.K., Han, S.S., 2011. Experimental Data on Scale Modeling Studies on Internal Fire Whirls. Int. J. on eng. performance-based fire codes 10, 63–74.

Chow, W.K., He, Z., Gao, Y., 2011. Internal Fire Whirls in a Vertical Shaft. Journal of Fire Sciences 29, 71–92. https://doi.org/10.1177/0734904110378974

Chuah, K.H., Kushida, G., 2007. The prediction of flame heights and flame shapes of small fire whirls. Proceedings of the Combustion Institute 31, 2599–2606. https://doi.org/10.1016/j.proci.2006.07.109

CNN, 2018. See “firenado” snatch firefighter’s hose.

Delichatsios, M.A., 1976. Fire growth rates in wood cribs. Combustion and Flame 27, 267–278.

Dermer, P.B., Varaksin, A.Y., Leontiev, A.I., 2017. The wall-free non-stationary fire whirls generation by axisymmetric burning of solid fuel pellets. International Journal of Heat and Mass Transfer 110, 890–897. https://doi.org/10.1016/j.ijheatmasstransfer.2017.03.076

Diab, M., Yip, A., Hadavand, M., Haelssig, J., Pegg, M., 2018. Experimental and Numerical Comparison of Small-scale Gaseous Fire Whirls. Journal of Physics: Conference Series 1107, 042032. https://doi.org/10.1088/1742-6596/1107/4/042032

Diab, M.T., Haelssig, J.B., Pegg, M.J., 2020. The behaviour of wood crib fires under free burning and fire whirl conditions. Fire Safety Journal 112, 102941. https://doi.org/10.1016/j.firesaf.2019.102941

Drysdale, D., 1998. An Introduction to Fire Dynamics, Second. ed. John Wiley & Sons, Chichester.

D'Souza, M.V., McGuire, J.H., 1977. ASTM E-84 and the flammability of foamed thermosetting plastics. Fire Technology 13, 85–94. https://doi.org/10.1007/BF02303053

Emmons, H., Ying, S., 1967. The Fire Whirl. Proceedings of the 11th International Symposium on Combustion 475–488.

Fang, X., Yuen, A.C.Y., Yeoh, G.H., Lee, E.W.M., Cheung, S.C.P., 2020. Capturing the Swirling Vortex and the Impact of Ventilation Conditions on Small-Scale Fire Whirls. Applied Sciences 10, 3428. https://doi.org/10.3390/app10103428

Fons, W.L., Clements, H.B., George, P.M., 1963. Scale effects on propagation rate of laboratory crib fires. Symposium (International) on Combustion 9, 860–866. https://doi.org/10.1016/S0082-0784(63)80092-2

FDS, (2022). Fire Dynamics Simulator, pages.nist.gov/fds-smv/

Forthofer, J.M., Goodrick, S.L., 2011. Review of Vortices in Wildland Fire. Journal of Combustion 2011. https://doi.org/10.1155/2011/984363

Gao, Z., Li, S., Gao, Y., Chow, W.K., 2019. Experimental studies on characteristics of fire whirl in a vertical shaft. Fire and Materials 43, 229–240. https://doi.org/10.1002/fam.2691

Gao, Z., Li, S.S., Gao, Y., Hung, H.Y., Chow, W., 2021. Numerical studies on swirling of internal fire whirls with experimental justifications. Build. Simul. 14, 1499–1509. https://doi.org/10.1007/s12273-020-0756-5

Ghodrat, M., Shakeriaski, F., Nelson, D.J., Simeoni, A., 2021. Experimental and Numerical Analysis of Formation and Flame Precession of Fire Whirls: A Review. Fire 4, 43. https://doi.org/10.3390/fire4030043

Graham, H.E., 1955. Fire Whirlwinds. Bull. Am. Meteorol. Soc. 36, 99–103.

Gross, D., n.d. Experiments on the burning of cross piles of wood 7.

Hariharan, S.B., Farahani, H.F., Rangwala, A.S., Dowling, J.L., Oran, E.S., Gollner, M.J., 2021. Comparison of particulate-matter emissions from liquid-fueled pool fires and fire whirls. Combustion and Flame 227, 483–496. https://doi.org/10.1016/j.combustflame.2020.12.033

Hartl, K.A., Smits, A.J., 2021. The interaction of double burner fire whirls. Combustion and Flame 111679. https://doi.org/10.1016/j.combustflame.2021.111679

Hartl, K.A., Smits, A.J., 2019. Stereo PIV measurements in fire whirls. Exp Fluids 60, 17. https://doi.org/10.1007/s00348-018-2661-6

Hartl, K.A., Smits, A.J., 2016. Scaling of a small scale burner fire whirl. Combustion and Flame 163, 202–208. https://doi.org/10.1016/j.combustflame.2015.09.027

Heskestad, G., 2016. Chapter 13: Fire Plumes, Flame Height, and Air Entrainment, in: SFPE Handbook of Fire Protection Engineering. M.J. Hurley Editor-in-Chief, pp. 396–420.

Heskestad, G., 1999. Turbulent jet diffusion flames: consolidation of flame height data. Combustion and Flame 118, 51–60. https://doi.org/10.1016/S0010-2180(98)00161-8

Heskestad, G., 1998. On Q∗ and the dynamics of turbulent diffusion flames. Fire Safety Journal 30, 215–227. https://doi.org/10.1016/S0379-7112(97)00035-0

Heskestad, G., 1983. Luminous heights of turbulent diffusion flames. Fire Safety Journal 5, 103–108. https://doi.org/10.1016/0379-7112(83)90002-4

Hu, L., Wang, Q., Delichatsios, M., Tang, F., Zhang, X., Lu, S., 2013. Flame height and lift-off of turbulent buoyant jet diffusion flames in a reduced pressure atmosphere. Fuel 109, 234–240. https://doi.org/10.1016/j.fuel.2012.12.050

Hu, L.H., Huo, R., Li, Y.Z., Wang, H.B., 2004. Experimental Study on the Burning Characteristics of Wood Cribs in a Confined Space. Journal of Fire Sciences 22, 473–489. https://doi.org/10.1177/0734904104042595

Huang, X., Zhuo, X., Huang, T., Zheng, Z., Cheng, C., Chow, W., 2019. Simple flame height correlation for buoyancy-controlled diffusion plumes generated by rectangular sources fire with different aspect ratios. Fuel 254, 115655. https://doi.org/10.1016/j.fuel.2019.115655

Janardhan, R.K., Hostikka, S., 2021. When is the fire spreading and when it travels? – Numerical simulations of compartments with wood crib fire loads. Fire Safety Journal 126, 103485. https://doi.org/10.1016/j.firesaf.2021.103485

Kallada Janardhan, R., Hostikka, S., 2019. Predictive Computational Fluid Dynamics Simulation of Fire Spread on Wood Cribs. Fire Technol 55, 2245–2268. https://doi.org/10.1007/s10694-019-00855-3

Kamikawa, D., Weng, W.G., Kagiya, K., Fukuda, Y., Mase, R., Hasemi, Y., 2005. Experimental study of merged flames from multifire sources in propane and wood crib burners. Combustion and Flame 142, 17–23. https://doi.org/10.1016/j.combustflame.2005.02.004

Karlsson, B., Quintiere, J.G., 2000. Enclosure fire dynamics, Environmental and energy engineering series. CRC Press, Boca Raton, FL.

Klimenko, A.Y., Williams, F.A., 2013. On the flame length in firewhirls with strong vorticity. Combustion and Flame 160, 335–339. https://doi.org/10.1016/j.combustflame.2012.10.019

Kuwana, K., Matsue, K., Fukumoto, Y., Dobashi, R., Saito, K., 2022. Fire whirls: A Combustion Science Perspective. Combustion Science and Technology 1–18. https://doi.org/10.1080/00102202.2021.2019234

Kuwana, K., Morishita, S., Dobashi, R., Chuah, K.H., Saito, K., 2011. The burning rate's effect on the flame length of weak fire whirls. Proceedings of the Combustion Institute 33, 2425–2432. https://doi.org/10.1016/j.proci.2010.05.049

Kuwana, K., Saito, K., Williams, F.A., 2020. Fire-whirl Movement along Line Fires – A Separated-flow Rotating-cylinder Analogy. Combustion Science and Technology 192, 1160–1172. https://doi.org/10.1080/00102202.2020.1712376

Kuwana, K., Sekimoto, K., Saito, K., Williams, F.A., 2008. Scaling fire whirls. Fire Safety Journal 43, 252–257. https://doi.org/10.1016/j.firesaf.2007.10.006

Lei, J., Liu, N., 2016. Flame precession of fire whirls: A further experimental study. Fire Safety Journal 79, 1–9. https://doi.org/10.1016/j.firesaf.2015.10.005

Lei, J., Liu, N., Jiao, Y., Zhang, S., 2017a. Experimental investigation on flame patterns of buoyant diffusion flame in a large range of imposed circulations. Proceedings of the Combustion Institute 36, 3149–3156. https://doi.org/10.1016/j.proci.2016.06.072

Lei, J., Liu, N., Tu, R., 2017b. Flame height of turbulent fire whirls: A model study by concept of turbulence suppression. Proceedings of the Combustion Institute 36, 3131–3138. https://doi.org/10.1016/j.proci.2016.06.080

Lei, J., Liu, N., Zhang, L., Chen, H., Shu, L., Chen, P., Deng, Z., Zhu, J., Satoh, K., de Ris, J.L., 2011. Experimental research on combustion dynamics of medium-scale fire whirl. Proceedings of the Combustion Institute 33, 2407–2415. https://doi.org/10.1016/j.proci.2010.06.009

Lei, J., Liu, N., Zhang, L., Satoh, K., 2015. Temperature, velocity and air entrainment of fire whirl plume: A comprehensive experimental investigation. Combustion and Flame 162, 745–758. https://doi.org/10.1016/j.combustflame.2014.08.017

Li, S., Yao, Q., Law, C.K., 2019. The bottom boundary-layer structure of fire whirls. Proceedings of the Combustion Institute 37, 4277–4284. https://doi.org/10.1016/j.proci.2018.05.009

Los Angeles Times, 2021. Watch powerful fire tornado as crews battle blazes across California.

Martin, R.E., Pendleton, D.W., Burgess, W., 1976. Effect of fire whirlwind formation on solid fuel burning rates. Fire Technol 12, 33–40. https://doi.org/10.1007/BF02629468

McAllister, S., Finney, M., 2016. Burning Rates of Wood Cribs with Implications for Wildland Fires. Fire Technol 52, 1755–1777. https://doi.org/10.1007/s10694-015-0543-5

McAllister, S., Finney, M., 2013. Effect of Crib Dimensions on Burning Rate, in: Proceedings of the Seventh International Seminar Fire and Explosion Hazards. Presented at the Proceedings of the Seventh International Seminar Fire and Explosion Hazards, Research Publishing Services, pp. 533–542. https://doi.org/10.3850/978-981-07-5936-0_08-02

McCaffrey, B.J., 1979. Purely buoyant diffusion flames: some experimental results (No. NBS IR 79-1910). National Bureau of Standards, Gaithersburg, MD. https://doi.org/10.6028/NBS.IR.79-1910

O'Dogherty, M.J., Young, R.A., 1964. Miscellaneous experiments on the burning of wooden cribs

Palacios, A., Bradley, D., 2022. Wildfires and the generation of fire whirls. Combustion and Flame 239, 111664. https://doi.org/10.1016/j.combustflame.2021.111664

Parente, R.M., Pereira, J.M.C., Pereira, J.C.F., 2019. On the influence of circulation on fire whirl height. Fire Safety Journal 106, 146–154. https://doi.org/10.1016/j.firesaf.2019.03.010

Pinto, C., Viegas, D., Almeida, M., Raposo, J., 2017. Fire whirls in forest fires: An experimental analysis. Fire Safety Journal 87, 37–48. https://doi.org/10.1016/j.firesaf.2016.11.004

Putnam, A.A., Speich, C.F., 1963. A model study of the interaction of multiple turbulent diffusion flames. Symposium (International) on Combustion 9, 867–877. https://doi.org/10.1016/S0082-0784(63)80093-4

Quintiere, J.G., 2006. Fundamentals of fire phenomena. John Wiley, Chichester.

Quintiere, J.G., 1989. Scaling applications in fire research. Fire Safety Journal 15, 3–29. https://doi.org/10.1016/0379-7112(89)90045-3

Quintiere, J.G., McCaffrey, B.J., 1980. The burning of wood and plastic cribs in an enclosure. Fire and Materials 1, 2–4.

Rembert, E.W., Haslam, R.T., 1925. Factors Influencing Length of a Gas Flame Burning in Secondary Air. Ind. Eng. Chem. 17, 1236–1238. https://doi.org/10.1021/ie50192a009

Smith, P.G., Thomas, P.H., 1970. The rate of burning of wood cribs. Fire Technology 6, 29–38. https://doi.org/10.1007/BF02588857

Snegirev, A.Yu., Marsden, J.A., Francis, J., Makhviladze, G.M., 2004. Numerical studies and experimental observations of whirling flames. International Journal of Heat and Mass Transfer 47, 2523–2539. https://doi.org/10.1016/j.ijheatmasstransfer.2004.02.002

Steward, F.R., 1970. Prediction of the Height of Turbulent Diffusion Buoyant Flames. null 2, 203–212. https://doi.org/10.1080/00102207008952248

Stubbs, D.C., Humphreys, L.H., Goldman, A., Childtree, A.M., Kush, J.S., Scarborough, D.E., 2021. An experimental investigation into the wildland fire burning characteristics of loblolly pine needles. Fire Safety Journal 126, 103471. https://doi.org/10.1016/j.firesaf.2021.103471

Sugawa, O., Sakai, K., 1997. Flame Length and Width Produced by Ejected Propane Gas Fuel from a Pipe. Fire Science and Technology 17, 55–63. https://doi.org/10.3210/fst.17.55

Tedim, F., McCaffrey, S., Leone, V., Vazquez-Varela, C., Depietri, Y., Buergelt, P., Lovreglio, R., 2021. Supporting a shift in wildfire management from fighting fires to thriving with fires: The need for translational wildfire science. Forest Policy and Economics 131, 102565. https://doi.org/10.1016/j.forpol.2021.102565

The Guardian, 2018. “A fire tornado”: death toll in massive California blaze rises to five.

Thomas, P.H., 1962. THE SIZE OF FLAMES FROM NATURAL FIRES 33.

Thomas, P.H., 1960. Buoyant diffusion flames. Combustion and Flame 4, 381–382. https://doi.org/10.1016/s0010-2180(60)80053-3

Tohidi, A., Gollner, M.J., Xiao, H., 2018. Fire Whirls. Annu. Rev. Fluid Mech. 50, 187–213. https://doi.org/10.1146/annurev-fluid-122316-045209

Wan, H., Gao, Z., Ji, J., Sun, J., Zhang, Y., Li, K., 2018. Predicting heat fluxes received by horizontal targets from two buoyant turbulent diffusion flames of propane burning

in still air. Combustion and Flame 190, 260–269. https://doi.org/10.1016/j.combustflame.2017.12.003

Wang, P., Liu, N., Zhang, L., Bai, Y., Satoh, K., 2015. Fire Whirl Experimental Facility with No Enclosure of Solid Walls: Design and Validation. Fire Technol 51, 951–969. https://doi.org/10.1007/s10694-014-0435-0

Wang, Q., Tang, F., Zhou, Z., Liu, H., Palacios, A., 2017. Flame height of axisymmetric gaseous fuel jets restricted by parallel sidewalls: Experiments and theoretical analysis. Applied Energy 208, 1519–1526. https://doi.org/10.1016/j.apenergy.2017.08.230

Wang, Z., Jia, F., Galea, E.R., Patel, M.K., Ewer, J., 2001. Simulating one of the CIB W14 round robin test cases using the SMARTFIRE fire field model. Fire Safety Journal 36, 661–677. https://doi.org/10.1016/S0379-7112(01)00018-2

Xu, Q., Griffin, G.J., Jiang, Y., Preston, C., Bicknell, A.D., Bradbury, G.P., White, N., 2008. Study of burning behavior of small scale wood crib with cone calorimeter. J Therm Anal Calorim 91, 787–790. https://doi.org/10.1007/s10973-007-8338-7

Yamashika, S., Kurimoto, H., 1976. Burning Rate of Wood Crib Report of Fire Research Institute of Japan, vol. 48, no. 8, 1976. (No. 8). Fire Research Institute of Japan.

Yeung, H.H., Han, S., Ki, W.C., Lun, C.C., 2019. Observation on a fire whirl in a vertical shaft using high-speed camera and associated correlation derived. Thermal Science 266–266.

Yu, H., Guo, S., Peng, M., Li, Q., Ruan, J., Wan, W., Chen, C., 2013. Study on the Influence of Air-inlet Width on Fire Whirls Combustion Characteristic. Procedia Engineering 62, 813–820. https://doi.org/10.1016/j.proeng.2013.08.130

Yuen, A.C.Y., Yeoh, G.H., Cheung, S.C.P., Chan, Q.N., Chen, T.B.Y., Yang, W., Lu, H., 2018. Numerical study of the development and angular speed of a small-scale fire whirl. Journal of Computational Science 27, 21–34. https://doi.org/10.1016/j.jocs.2018.04.021

Zhang, S., Ni, X., Zhao, M., Feng, J., Zhang, R., 2015a. Numerical simulation of wood crib fire behavior in a confined space using cone calorimeter data. J Therm Anal Calorim 119, 2291–2303. https://doi.org/10.1007/s10973-014-4291-4

Zhang, S., Ni, X., Zhao, M., Zhang, R., Zhang, H., 2015b. Experimental study on the characteristics of wood crib fire in a confined space with different ventilation conditions. J Therm Anal Calorim 120, 1383–1391. https://doi.org/10.1007/s10973-014-4359-1

Zhang, Xiaochun, Hu, L., Zhu, W., Zhang, Xiaolei, Yang, L., 2014. Flame extension length and temperature profile in thermal impinging flow of buoyant round jet upon

a horizontal plate. Applied Thermal Engineering 73, 15–22. https://doi.org/10.1016/j.applthermaleng.2014.07.016

Zhou, K., Liu, N., Zhang, L., Satoh, K., 2014. Thermal Radiation from Fire Whirls: Revised Solid Flame Model. Fire Technol 50, 1573–1587. https://doi.org/10.1007/s10694-013-0360-7

Zhou, K., Qin, X., Zhang, L., Wu, Y., 2019. An experimental study of jet fires in rotating flow fields. Combustion and Flame 210, 193–203. https://doi.org/10.1016/j.combustflame.2019.08.034

Zou, G., Chow, W., 2015. Generation of an internal fire whirl in an open roof vertical shaft model with a single corner gap. Journal of Fire Sciences 33, 183–201. https://doi.org/10.1177/0734904115569703

Zou, G.W., Hung, H.Y., Chow, W.K., 2019. A study of correlation between flame height and gap width of an internal fire whirl in a vertical shaft with a single corner gap. Indoor and Built Environment 28, 34–45. https://doi.org/10.1177/1420326X17729742

Zukoski, E.E., 1995. Properties of fire plumes, in: Combustion Fundamentals of Fire. Academic Press, pp. 101–219.

Zukoski, E.E., Kubota, T., Cetegen, B., 1981. Entrainment in fire plumes. Fire Safety Journal 3, 107–121. https://doi.org/10.1016/0379-7112(81)90037-0

Appendix A: Derivations and Calculations

For square-based cribs with n sticks per layer of length l and square cross-section b and N layers, the crib height (h) is given by the following equation:

$$h = Nb \tag{A-1}$$

The spacing between sticks in each layer can be calculated as follows:

$$s = (l - nb)/(n - 1) \tag{A-2}$$

The total cross-sectional area of all the vertical shafts (A_v) is given by the following expression:

$$A_v = (l - nb)^2 \tag{A-3}$$

The total cross-sectional area of the side openings on any one side (A_{so}) can be calculated as follows:

$$A_{so} = (n - 1)sb\,(N - 1)/2 = (l - nb)b\,(N - 1)/2 \tag{A-4}$$

The total exposed fuel surface area of a crib, which sits on a flat surface such that the underside of the bottom layer of sticks is not exposed, is given by the following equation:

$$A_s = 2nb[N(2l - nb) + b(n + N)] - bln \tag{A-5}$$

The crib porosity can be calculated as follows:

$$\varepsilon = 1 - nb/l \tag{A-6}$$